UNIVERSITY OF OKLAHOMA

GRADUATE COLLEGE

EXPERIMENTAL AND NATURAL STUDIES OF MN AND THE ISOTOPES OF B IN GRANITE-PEGMATITE SYSTEMS

A DISSERTATION

SUBMITTED TO THE GRADUATE FACULTY

in partial fulfillment of the requirements for the

Degree of

DOCTOR OF PHILOSOPHY

By

JAMES LAVADA MANER IV
Norman, Oklahoma
2017

EXPERIMENTAL AND NATURAL STUDIES OF MN AND THE ISOTOPES OF B IN GRANITE-PEGMATITE SYSTEMS

A DISSERTATION APPROVED FOR THE
CONOCOPHILLIPS SCHOOL OF GEOLOGY AND GEOPHYSICS

BY

_____
Dr. David London, Chair

_____
Dr. Andrew S. Elwood Madden

_____
Dr. Barry L. Weaver

_____
Dr. Robert Thomson

_____
Dr. George R. Rossman

Dedication

This dissertation is dedicated to my family

I would not be in the position of writing this dissertation without the emotional support of my family. They stood behind me for nearly 12 years while I completed my undergraduate and graduate education. I'll always remember the sacrifices they chose to make to ensure that my dreams could become reality. I would like to specifically thank Taylor Davis. Unlike many people at OU, Taylor was, and is, fully aware of the hardships I endured while completing my Ph.D. When the times got rough, and everyone else turned their backs on me, Taylor stood by my side and encouraged me to continue pursuing my education. I look forward to spending many more years with Taylor.

Acknowledgments

Completion of this dissertation would not have been possible without the assistance, guidance, and emotional support of many people. First and foremost, I would also like to thank Dr. David London for being my mentor and friend for the past several years. Dr. London is a tremendously generous and intelligent man. The experimental lab became a sort of classroom for me for many years. Much of what I have learned about experimental petrology, granites, and pegmatites came from discussion with Dr. London. Secondly, I would like to thank Dr. George B. Morgan VI. Many hours and days were spent in the electron microprobe lab analyzing minerals and glasses. George was not only extremely helpful but very entertaining. Between the electron microprobe course and the daily dialogue in the electron microprobe lab, I gained a skillset that helped me land a job as an electron microprobe operator. I would also like to thank George for inviting me to his house for the holidays, in case I had nowhere else to go.

I would like to thank Drs. Lynda Williams and Rich Hervig for their assistance with the Cameca 6f secondary ion mass spectrometer (SIMS) at Arizona State University. It is thanks to both that I now have not only a fundamental knowledge of SIMS but the ability to critically evaluate instrument setups and analytical routines. I'll carry that knowledge forward through my life.

Lastly, I would like to thank my committee members. Their support has not gone unnoticed.

Table of Contents

List of Tables

List of Figures

Abstract

Partition coefficients (D) and exchange coefficients (K_D) for Fe, Mn, and Mg between tourmaline (Tur), garnet (Grt), cordierite (Crd) and granitic melt were measured between 650°C and 850°C at 200 MPa_{H2O}. Manganese is incompatible in tourmaline ($D_{Mn} \approx 0.3$ to 0.9) at temperatures greater than 650°C and is highly compatible in garnet ($D_{Mn} \approx 15$ to 39) and cordierite ($D_{Mn} \approx 2$ to 7) at all temperatures. Tourmaline is not stable at temperatures greater than 750°C. The partition coefficients are used in a Rayleigh fractional crystallization model to test their ability to predict the point at which Mn-rich garnet (spessartine) would become saturated in an S-type granitic melt. As expected, approximately 90% of crystallization is necessary to bring the Mn content of an anatectic S-type granitic liquid to spessartine saturation at ~ 665°C and 200 MPa.

The boron isotopic composition, $\delta^{11}B$, of borate and borosilicate minerals (including tourmaline (Tur)) from three dikes at the Little Three (LT3) pegmatite mine, Ramona, CA, were measured using secondary ion mass spectrometry (SIMS). The tourmaline at the LT3 were found to be strikingly heavy compared to tourmaline from other pegmatites. At the LT3, average values of $\delta^{11}B_{Tur}$ are constant across magmatic portions of each dike. Values of $\delta^{11}B_{Tur}$ only increase from massive pegmatite into miarolitic cavity where other B-bearing minerals, whose B is in 4-fold coordination, occur with tourmaline. A thermal cooling model shows that the pegmatites would have crystallized in a matter of days, which is much faster than the diffusivity of B in hydrous granitic melt. Therefore, it is unlikely that the $\delta^{11}B$ of tourmaline records an equilibrium composition with respect to melt (or aqueous solution). Altered oceanic

crust is a likely source of the pegmatite-forming melt, and B, based on similarities of boron isotopic composition and geochemistry of potential source plutons.

Dozens of experiments were conducted to measure the diffusivity of B in hydrous granitic melt at 800°C at 200 MPa, and to assess the diffusive separation of ^{10}B and ^{11}B. In a different series of experiments, the fractionation of boron isotopes between granitic melt and aqueous solution was measured at 700°C and 800°C at 200 MPa_{H2O}. Boron diffuses at a rate similar to Al (10^{-13} m^2/s) in hydrous granitic melt, and ^{10}B diffuses faster than ^{11}B. Fractionation of boron isotopes between granitic melt and aqueous solution is shown to be significant and corroborates the results of Hervig et al. (2002). However, in one experiment (MAC230) the $\delta^{11}B$ of the final glass is identical to the starting glass (Macusani obsidian). The rapid crystallization of the melt in MAC230 must have exceeded the diffusivity of B through melt at 500°C such that the aqueous solution (i.e. miarolitic cavity) and melt could not equilibrate; a result that corroborates the findings at the LT3 pegmatite mine.

Chapter 1 Introduction

The first project of my graduate training was to investigate the partitioning of Fe-Mn and Fe-Mg among garnet, tourmaline, and biotite. The primary goal of that project was to assess the effect of Mn on the well-known Fe-Mg garnet-biotite geothermometer. A secondary goal was to measure the distribution of Fe-Mn and Fe-Mg between garnet and tourmaline toward calibrating a geothermometer that could be applied to evolved granites and pegmatites. Although garnet and biotite crystallized from granitic melt in some experiments, biotite crystals were too small for chemical characterization using electron microprobe methods. In another, more extensive, series of experiments, in which a B-bearing granitic liquid was used as a starting material, tourmaline crystallized with garnet. In several experiments, especially those at T > 750°C, cordierite crystallized (with garnet) instead of tourmaline. Tourmaline and garnet were saturated with Mn and Mg, respectively, at very low concentrations which severely limited their use for geothermometery. Thus, neither of the main goals of my first project were accomplished. Nevertheless, a substantial amount of mineral-melt partitioning data was collected from those experiments.

Partition coefficients for Fe, Mn, and Mg between tourmaline, cordierite, garnet, and granitic melt have not been thoroughly investigated in prior experimental work. Partition coefficients for tourmaline and garnet would be useful for understanding the enrichment of Mn from source to evolved granite and pegmatite. Though it is apparent that the enrichment of Mn in residual granitic liquid must occur via the crystallization of other minerals in which Mn is incompatible, experimental studies have not directly confirmed this hypothesis.

Chapter 5 of this dissertation reports mineral-melt partitioning data and solubility data for cordierite, tourmaline, and garnet. The data are used, in conjunction with data from the literature for biotite and muscovite, in a Rayleigh fractional crystallization model to assess the amount of fractional crystallization necessary to bring an anatectic S-type granitic melt to spessartine saturation. The model predicts that ~ 90% crystallization of an anatectic S-type granitic melt is necessary to bring the Mn content of melt high enough to precipitate Mn-rich garnet at ~ 665°C and 200 MPa. Though there are caveats associated with how the model is constructed, the goal of the model was to test the applicability of the experimentally measured partition coefficients. The occurrence of Mn-rich garnet in granitic rocks is limited to only the highly evolved suites, which is consistent with the model presented in Chapter 5, which suggests to me that the partition coefficients are applicable to natural systems.

After completing my work with mineral-melt partitioning, I began research that focused on the boron isotopic composition, $\delta^{11}B$, of tourmaline (Tur) in granites and pegmatites. The $\delta^{11}B$ of tourmaline has been used to

(1) infer crystallization processes,

(2) identify sources of melt and aqueous fluid, and

(3) test for the presence of an aqueous solution and understand its role in the crystallization of granites and pegmatites.

The first and third points require a knowledge of equilibrium fractionation factors in the system tourmaline-granitic melt-aqueous solution, which is incompletely characterized. Equilibrium between tourmaline, melt, and aqueous solution can be tested by comparing the $\delta^{11}B$ of tourmaline with Rayleigh models, for as long as the sequence of

crystallization is known and the spatial distribution of tourmaline crystals in the pegmatite is preserved. All previous studies of the $\delta^{11}B$ of tourmaline from pegmatites have sampled crystals from massive pegmatite and miarolitic cavities. No study has systematically sampled tourmaline crystals from margin to core of a pegmatite; that would allow for an assessment of equilibrium crystallization in pegmatites.

Chapter 2 reports $\delta^{11}B$ values for borate and borosilicate minerals (including tourmaline) from three different mines (named Main, Swamp, and Spessartine) on the Little Three pegmatite property, Ramona, CA. This is the first study in which the spatial distribution of all minerals was preserved, to the centimeter, throughout the pegmatites. Moreover, London et al. (2012) and Morgan and London (1999) estimated a crystallization temperature of 450°C based on the compositions of feldspars, and they recorded the modes of all minerals throughout the pegmatites. Therefore, the pegmatites at the Little Three mine are uniquely suitable to test equilibrium fractionation factors for boron's isotopes by comparing the compositions of tourmaline against a Rayleigh model.

Two peculiarities emerged from the boron isotopic data reported in Chapter 2:

(1) The average $\delta^{11}B$ of tourmaline from one zone to another is constant from margin to core of the Main dike and

(2) that the $\delta^{11}B$ of tourmaline is strikingly heavy compared to tourmaline from other pegmatites.

The constancy of $\delta^{11}B_{Tur}$ values across the Main dike could reflect an equilibrium distribution of boron's isotopes between tourmaline and granitic melt if $\Delta^{11}B_{Tur\text{-}melt}$ is zero. However, there is reason to believe that $\Delta^{11}B_{Tur\text{-}melt}$ should be non-zero and

positive. The value for $\Delta^{11}B_{Tur\text{-}melt}$ is positive (~ +12‰) when calculated using values for $\Delta^{11}B_{Melt\text{-}vapor}$ (Hervig et al. 2002), which are significantly negative at pegmatite-forming temperatures (e.g. 450°C), and $\Delta^{11}B_{Tur\text{-}vapor}$ (Palmer et al. 1992, Meyer et al. 2008). Therefore, it is unlikely that the flat profile of $\delta^{11}B_{Tur}$ values across the Main dike reflects an equilibrium distribution of boron's isotopes between tourmaline and granitic melt. Even so, uncertainties related to $\Delta^{11}B_{Tur\text{-}melt}$ and $\Delta^{11}B_{Melt\text{-}vapor}$ preclude using the $\delta^{11}B$ of tourmaline to assess equilibrium conditions in pegmatites. Moreover, a decrease in the $\delta^{11}B$ of tourmaline from core to rim could reflect a faster diffusivity of ^{10}B compared to ^{11}B and not to a positive value for $\Delta^{11}B_{Tur\text{-}melt}$ or to the partioning of ^{11}B to an aqueous solution from melt, if ^{10}B and ^{11}B diffuse at different rates, and ^{10}B is faster than ^{11}B.

It is likely that the flat profile of $\delta^{11}B_{Tur}$ values reflects the bulk composition of the melt due to the slower rate of diffusion of B in hydrous granitic melt compared to the rapid rate of crystallization of the pegmatite. A comparison of the modeled cooling rate of the pegmatite with the diffusivity of B in hydrous, granitic melt reveals that the pegmatite crystallized much faster than B could have diffused through melt. Based in part on the boron isotopic composition of the pegmatites, it is likely that the source of the pegmatite-forming melt was altered oceanic crust.

The $\delta^{11}B$ of tourmaline increases from coarse pegmatite into miarolitic cavity where other B-bearing minerals, whose B is in 4-fold structural coordination, occur with tourmaline in the miarolitic cavity. In miarolitic cavities where tourmaline is the sole, or dominant, host of B, the $\delta^{11}B$ of tourmaline does not change from coarse pegmatite into miarolitic cavity. It would seem, therefore, that if miarolitic cavities represent

crystallization from an aqueous solution, then boron isotopic fractionation between granitic melt and aqueous solution should be nil (if equilibrium prevails). Experiments by Hervig et al. (2002) suggest that the fractionation of boron isotopes between granitic melt and aqueous solution is large, even at liquidus temperature.

The results from the study of the Little Three pegmatites posed two questions. Do ^{11}B and ^{10}B have different diffusion coefficients in hydrous granitic melt? What is the magnitude and direction of $\Delta^{11}B_{Tur\text{-}melt}$ and $\Delta^{11}B_{Melt\text{-}vapor}$?

In Chapter 3, I report experimental data showing that ^{11}B diffuses at a slower rate compared to ^{10}B. Moreover, the data in Chapter 3 show that the diffusivity of B in hydrous granitic melt at 800°C is similar to Al. The diffusion data for B in hydrous granitic melt support the hypothesis that the $\delta^{11}B$ of tourmaline from pegmatite dikes that crystallize rapidly cannot reflect an equilibrium composition with respect to melt. Nevertheless, the $\delta^{11}B$ of tourmaline can still be used to identify potential source materials.

Chapter 4 reports data from experiments designed to measure the fractionation of ^{11}B and ^{10}B between granitic melt and aqueous solution. The fractionation of boron isotopes between granitic melt (Macusani obsidian) and aqueous fluid was first investigated by Hervig et al. (2002). In their study, they found significant fractionation between melt and aqueous solution at 750°C and 850°C (500 MPa). However, some studies have questioned the values reported by Hervig et al. (2002) based on similarities of $\delta^{11}B_{Tur}$ values in associated magmatic and vapor-saturated environments (e.g. miarolitic pegmatites and veins emanating from granitic plutons (Beurlen et al., 2011; da Costa et al., 2014; Drivenes et al., 2015; Jiang and Palmer, 1998; Jiang et al., 2008,

2003; Pesquera et al., 2005; Siegel et al., 2016; Smith and Yardley, 1996; Tonarini et al., 1998; Trumbull et al., 2013, 2008; Trumbull and Chaussidon, 1999; Yang et al., 2015). The experiments reported by Hervig et al. (2002) were conducted using a chip of Macusani obsidian at 850°C and 750°C for 24 and 48 hours, respectively. In 2014, Rick Hervig provided me with a SIMS transect of a glass (Macusani obsidian) that had been heated to 950°C (100 MPa) for 7 days. The profile shows an abrupt 15‰ decrease in $\delta^{11}B$ at the melt-aqueous fluid interface and the $\delta^{11}B$ of glass < 400 µm from the interface has the same composition as the initial, unreacted glass (Fig. 1-1). Therefore, the data reported in Hervig et al. (2002), which was conducted at lower temperature and for a shorter duration, appears unlikely to reflect an equilibrium distribution of boron's isotopes between melt and aqueous solution.

The experiments reported in Chapter 4 used the Macusani obsidian and a glass whose composition is close to the thermal minimum in the haplogranite system at 200 MPa_{H2O}. Each experiment was heated to either 700°C or 800°C (200 MPa_{H2O}) for 30 days. The $\delta^{11}B$ of the resultant glass was measured by SIMS and the $\delta^{11}B$ of the final aqueous solution was calculated using mass-balance equations. Values of $\Delta^{11}B_{Melt\text{-}vapor}$ are similar to those reported by Hervig et al. (2002).

Glass from one experiment, MAC230 (London and Morgan 2017), in which a core of Macusani obsidian was allowed to crystallize almost completely and formed a large miarolitic cavity in residual melt, was analyzed by SIMS. The $\delta^{11}B$ of the residual glass in MAC230 is identical to the starting glass. The rapid crystallization of the Macusani glass in MAC230 must not have allowed the fluid in the miarolitic cavity to

equilibrate with melt. The result from MAC230 appears to be directly applicable to pegmatite systems, e.g. Little Three pegmatites (Chapter 2).

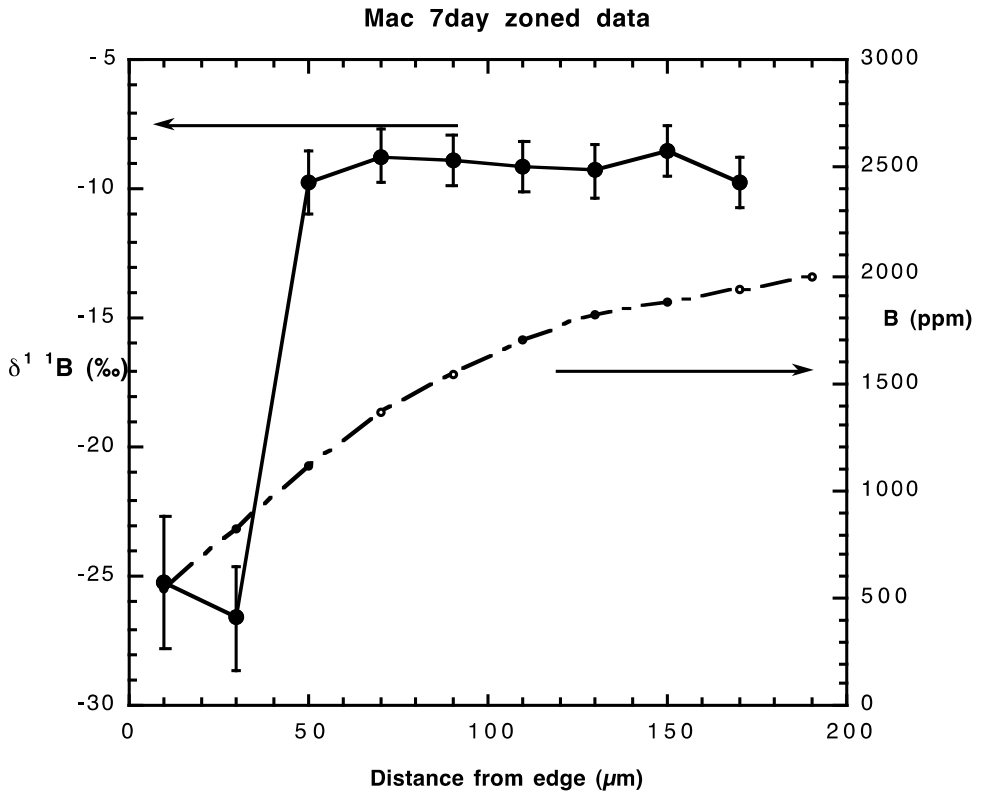

Figure 1-1 Boron and boron isotopic zoning in Macusani obsidian held at 950˚C and 1 kilobar pressure for 7 days. Filled symbols are boron isotopic ratios. Error bars are 2 standard errors of the mean. The starting composition was ~-9‰. The small open symbols are total boron contents in ppm (by weight).

Chapter 2 The boron isotopic evolution of the Little Three pegmatites, Ramona, CA

1. Introduction

Tourmaline (Tur) is the most abundant boron-rich mineral in the continental crust (Grew, 1996), where it is commonly associated with evolved S-type granites and their derivative LCT (Li, Cs, Ta) pegmatites (Černý and Ercit, 2005; London et al., 1996). The boron isotopic composition, $\delta^{11}B$, of tourmaline and the fractionation of boron's isotopes, ^{10}B and ^{11}B, in the system tourmaline-granitic melt-aqueous solution have been the focus of many studies, all with the intent of assessing the roles and sources of melt and aqueous solution in the formation of granites and pegmatites (Beurlen et al., 2011; da Costa et al., 2014; Drivenes et al., 2015; Jiang and Palmer, 1998; Jiang et al., 2008, 2003; Pesquera et al., 2005; Siegel et al., 2016; Smith and Yardley, 1996; Tonarini et al., 1998; Trumbull et al., 2013, 2008; Trumbull and Chaussidon, 1999; Yang et al., 2015). Among these studies, some have reported little or no change in the values of $\delta^{11}B_{Tur}$ from the juvenile source granites all the way through to tourmaline that crystallized in the miarolitic cavities of highly fractionated pegmatites (Tonarini et al., 1998), whereas in other individual pegmatites, the range of $\delta^{11}B$ values for tourmaline is nearly 20‰ (Trumbull et al., 2013). Where variations in $\delta^{11}B_{Tur}$ are observed, they are thought to represent a variety of processes, including:

1) fractional crystallization with concomitant isotopic fractionation between tourmaline, melt and/or aqueous fluid (Trumbull et al., 2013; Siegel et al., 2016),

2) the co-crystallization of micas (Siegel et al., 2016) and borates/borosilicates (De Vito et al., 2002; Dini et al., 2002; Dini and Tonarini, 2002) whose B is structurally bound in 4-fold coordination, resulting in a strong preference for ^{10}B over ^{11}B, and
3) the influx of fluids from the host rock into the pegmatite (Trumbull et al., 2013).

Interpretation of $\delta^{11}B_{Tur}$ values relies upon two precepts: (1) a knowledge of equilibrium boron isotopic fractionation factors, particularly in the system tourmaline-melt-aqueous fluid, and (2) a presumption that the values measured in natural systems are those attained at isotopic equilibrium. Boron isotopic fractionation, $\Delta^{11}B$, between melt-aqueous solution has been experimentally measured (Hervig et al., 2002), and those results show an enrichment of ^{11}B in aqueous fluid relative to melt; however, the magnitude of these fractionation factors have been questioned by some scientists (Trumbull et al., 2013). Fractionation factors for the system tourmaline-aqueous solution have been experimentally measured (Meyer et al., 2008; Palmer et al., 1992) and calculated using *ab initio* first principles methods (Kowalski et al. 2013). Though differences in experimental techniques have produced uncertainties regarding the absolute values of fractionation in the system tourmaline-aqueous solution, there is consensus that the fractionation of boron's isotopes between tourmaline-aqueous solution will yield an isotopically heavy solution. Fractionation in the system tourmaline-melt remains completely undocumented.

In summary, the boron isotopic composition of tourmaline may provide information on the processes by which granites and pegmatites crystallize. However, uncertainties in boron isotopic fractionation factors among tourmaline-granitic melt-aqueous solution hinder interpretations of the boron isotopic compositions of tourmaline

from granites or pegmatites. Until those uncertainties are resolved via carefully executed experiments, systematic and thorough sampling of tourmaline from pegmatites and accurate boron isotopic analyses are still essential toward advancing a growing knowledge of boron isotopic compositions of tourmaline from pegmatites.

1.1. Goal of This Study

The goal of this study is to measure the boron isotopic composition of borosilicate and borate minerals in the pegmatites (names Main, Swamp, and Spessartine) of the Little Three mine with the principal aims of

1) using the boron isotopic composition of each pegmatite to ascertain the likely source of the boron component of these pegmatites, and
2) interpreting the fractionation of boron's isotopes from margin to miarolitic cavities using the boron isotopic composition of tourmaline.

The pegmatites of the Little Three mine near Ramona, California, are ideally suited for this task. The pegmatites have been shown by London et al. (2012) and Morgan and London (1999) to have crystallized nearly isothermally at ~ 450°C as essentially closed systems. The modal mineralogy by zones within the pegmatites is well-documented. In the present study, we evaluate $\delta^{11}B_{Tur}$ inward from margins to centers of the Main and Swamp dikes at the centimeter scale in oriented samples that constitute continuous sections through both dikes.

2. Geology of Pegmatites at the Little Three Mine

2.1. Location, structure, and host rocks.

The Little Three pegmatite claims (coordinates +33° 3’ 28.44”, -116° 47’ 31.67”), approximately 7.5 km east of the town of Ramona, California, lie at the southeast end of a swarm of granitic pegmatite dikes. The Main dike contains the thickest section of pegmatite, up to ~ 2.5 meters (Morgan and London, 1999; Stern et al., 1986), and has been a significant source of fine crystals of topaz, elbaite, lepidolite, feldspar, quartz, hambergite, bismuthian stibiotantalite, and boromuscovite from miarolitic cavities (Fisher, 2002; Foord, 1982; Foord et al., 1991a, 1991b, 1989, 1986; Kordela, 1990; London, 2013; Novak et al., 1998; Sinkankas, 1956, 1967). The Spessartine claim, with a maximum thickness of ~ 1.5 meters, lies within the same dike as the Hercules claim to the west (Foord et al., 1989); the Spessartine claim has produced much of the finest gem-quality spessartine found anywhere in the world (Laurs and Knox, 2001). The Swamp dike is synonymous with workings described as the Spaulding-Hatfield Creek-Sinkankas dikes in Foord et al. (1989). Other small, unnamed pegmatite dikes occur on the property.

These dikes have a ~N45°W strike, have outcrop with widths on the order of a few meters, and strike at lengths of up to ~ 1.5 km of continuous exposure. The dip of each pegmatite varies from subhorizontal to ~ 70° to the southwest (London et al., 2012; Simpson, 1965; Stern et al., 1986). London et al. (2012) proposed that the sharp fluctuations in dip may represent a stepped, or en-echelon dike dimension; hence, the sub-horizontal and steeply dipping outcrops could represent portions of the same dike.

Apart from one small outcrop showing a cross-cutting of two dike segments in the Main dike, each dike appears to be a single injection of crystal-free granitic melt.

The pegmatites are hosted by mafic tonalites of the Ramona Complex within a transitional area between the Western and Eastern zones of the Peninsular Range Batholith (PRB) (London et al., 2012; Symons et al., 2009). Gabbroic and granitic rocks in the PRB were emplaced during the Jurassic and Cretaceous (Todd et al., 2003). Granitic rocks in the Western zone have chemical affinities with I-type granites ($Sr_i \leq 0.705$, $\delta^{18}O \leq 8.5‰$; Symons et al., 2003) and those in the Eastern zone exhibit I-type and mixed I-S type affinities ($Sr_i \geq 0.705$, $\delta^{18}O \geq 9.0‰$: Symons et al., 2003). Magmatism in the Western zone lasted from ~122 Ma to ~100 Ma at which time magmatism in the Eastern zone began or became more active. Based on K-Ar (Foord et al., 1991a) and paleomagnetic ages (Symons et al., 2009), the emplacement of the pegmatites at the Little Three mine occurred between magmatic events in the Western and Eastern zones (ca. 98 to 100 Ma).

2.2. Internal zonation

London et al. (2012) estimated the modal mineralogy from margin-to-margin of the Swamp dike. A modal analysis of minerals in the Main dike has not been studied as extensively; however, the modal mineralogy of the exposed dike segments on the mine property exhibit the same overall internal zonation with few exceptions. Along the footwall contact of the Main dike, a coarse-grained granites grades sharply upward into massive leucocratic saccharoidal aplite, the first unit recognized as pegmatitic (Morgan and London, 1999). At the Swamp dike, a similarly coarse-grained granite is succeeded upward by graphic quartz – K-feldspar pegmatite. In both dikes, the footwall zones of

massive aplite or graphic granite grade upward into sharply layered saccharoidal aplite. Light bands have the modal composition of $Qtz_{22}Ab_{64}Kfs_{11}Tur_{03}Gt_{00}Ms_{00}$, and dark bands consist of $Qtz_{23}Ab_{15}Kfs_{50}Tur_{12}Gt_{00}Ms_{00}$ (London et al., 2012). In both pegmatites, the layered aplite is succeeded upward by the lower intermediate zone ($Qtz_{22}Pl_{44}Kfs_{25}Tur_{03}Gt_{03}Ms_{02}$), with prominent coarse-grained unidirectional solidification texture (UST), which includes tourmaline crystals that flair (expand) inward toward the dike centers.

The wall zones along the hanging wall contacts with tonalite are dominated by plagioclase over K-feldspar, and they contain far more modal quartz than the footwall sections ($Qtz_{42}Ab_{39}Kfs_{07}Tur_{12}Gt_{00}Ms_{00}$). The wall zones grade downward into the same coarsely-crystalline upper intermediate zone with prominent UST fabric and graphic quartz – K-feldspar intergrowths. Approaching the dike centerline, the upper and lower intermediate zones of the Main and Swamp dikes become markedly enriched in K-feldspar and quartz ($Qtz_{43}Ab_{06}Kfs_{49}Tur_{00}Gt_{00}Ms_{00}$) in what constitutes the core of the Swamp dike. The Main and Spessartine dikes terminate with miarolitic cavities along their centerline; though the miarolitic cavities are quartz-rich, feldspars comprise an appreciable proportion of the contents (see Fig. 2 of London et al., 2012). In all three pegmatites, except for the Spessartine dike whose contacts are not exposed, tourmaline is present from margins to center, including rare miarolitic segments of the Swamp dike.

3. Methods

3.1. Description of samples

A complete and representative cross section of the Main dike of the Little Three pegmatite was collected as large, decimeter-sized rock samples (Fig. 2-1) (Morgan and London, 1999). Minerals from miarolitic cavities sampled for this study include a crystal of lepidolite, 2.0x2.0x0.5 cm, hambergite, of which only ~ 40 grams of material was collected, and two color zoned tourmaline crystals from the ’91 London pocket of the Main dike. One of the color zoned tourmaline crystals grades from a dark green base to a light green cap. The other crystal grades from a dark green base to a light green cap with a light pink layer covering the prismatic surfaces. Boromuscovite forms a fine-grained coating on nearly every mineral within the miarolitic cavities of the Main dike. A single tourmaline crystal extending approximately 6 cm from the upper intermediate zone downward toward the pocket-line is dark black along most of its length (~ 4 cm) then exhibits a light green section with a light pink cap at its termination.

A complete cross-section of the Swamp dike was collected as two boulders from which two large sections were cut and polished (Fig. 2-2). Euhedral crystals of danburite and tourmaline were collected by DL from a rare pocket in the Swamp dike. Crystals from the Spessartine dike, obtained from L.B. Spaulding, Jr., include three black tourmaline crystals, muscovite, and axinite from a pocket, black tourmaline from massive pegmatite. Two of the black tourmaline crystals from the pocket differ only in size; the third is intergrown with axinite. An external tourmalinite was collected by DL from the exposed hanging wall of Spaulding's workings. Photographs of all samples

collected from each miarolitic cavity and the external tourmaline are shown in Figure 2-3.

3.2. Preparation of samples for SIMS and EMPA

Tourmaline crystals were systematically sampled to preserve their spatial relationship with respect to height above the base of each dike. This was accomplished using two different sampling methods. In the first method, tourmaline crystals were hand-picked from crushed thin section billets of the Main dike aplite (line rock). In the second method, tourmaline crystals from the Main and Swamp dikes were sampled by drilling ¼" (W) x ½" (L) cores from areas with abundant tourmaline.

Two elbaite crystals from the '91 London pocket and the single, 6 cm long tourmaline crystal were sectioned parallel to their *c* crystallographic axes. Three fragments were taken from center to margin of the dark green/green elbaite crystal and from each of the three colored zones in the other elbaite crystal. The single, 6 cm long tourmaline crystal was sampled in 3 locations parallel to the *c* axial direction. The first location was from the base in the dark-black area, the second location was in a transitional area between the dark-black and pink areas, and the third location was near the pink tip of the crystal.

Hand-picked tourmaline crystals, and boron isotopic standards (dravite and axinite: characterized by Dyar et al. (2001) and Leeman and Tonarini (2001), were embedded in Crystalbond™ in ¼" brass cylinders. Cored material, axinite, hambergite, and danburite were cast in 1" circular molds and mounted using EpoThin™ epoxy. Boron isotopic standards and a dravite, whose boron isotopic composition of -11.8‰

has only been determined by SIMS, were cast in one 1" circular mount using EpoThin™ epoxy. All mounts were ground down to a 3 µm polish using diamond imbedded lapping films and the polished using diamond grit suspended in water to a ¼ µm polish. Polished crystals were removed from Crystalbond™ by soaking each mount in acetone overnight. Clean crystals and standards were placed in the central portion of indium filled aluminum holders and pushed into the indium metal using a hydraulic press which produced flat sample surfaces.

Cleavage fragments of muscovite and lepidolite and powdered boromuscovite were ultrasonically cleaned in solutions containing 1.8% mannitol, rinsed in deionized, ultra-filtered water, and placed in a desiccator to dry. Muscovite and lepidolite were pressed onto double-sided carbon-tape on a 1" Al stub such that their *c* crystallographic axes were perpendicular to the stub surface. Approximately 10 µL of the boromuscovite slurry was pipetted onto a standard 1" petrographic glass slide. On each mica mount was added approximately 5 µL of an illite standard suspension (IMt-1: Williams et al. (2001). The droplets were allowed to dry flat prior to gold coating. All samples were gold coated at the Arizona State University (ASU) Secondary Ion Mass Spectrometry (SIMS) facility immediately before analysis.

3.3. Electron Microbeam Analytical (EMPA) Methods

Tourmaline and micas were analyzed using the Cameca SX100 electron microprobe at the University of Oklahoma, which is equipped with 5 wavelength-dispersive spectrometers. A 15 kV accelerating voltage, 20 nA beam current, and a 2 µm spot size were used to analyze tourmaline crystals. Detection limits for Na, Mg, Al, Si, Fe, Mn, K, Ca, Ti, and F are below 0.04 wt.% oxide except for B_2O_3 which has a

detection limit of 0.70 wt.%. A 2-condition routine was developed for analysis of micas. Both conditions used a 20 kV accelerating voltage and 20 μm spot; the difference being a 2 nA current to analyze K, Na, Al, Si, and Ca and a 20 nA current to analyze Fe, Mn, and Mg. Detection limits for all elements analyzed using the mica analytical routine are below 0.06 wt.% oxide. Data reduction employed the PAP method (Pouchou and Pichoir, 1985).

Compositional data for tourmaline, determined by EMPA, are reported in Appendix 1. Mole fractions of end-member tourmaline components are calculated using the Excel^{TM} spreadsheet of Morgan (2016) and EMPA data. The spreadsheet calculates fractions for the following tourmaline species: schorl (Srl), dravite (Drv), elbaite (Elb), uvite (Uvt), feruvite (Fuv), foitite (Ftt), Mg-foitite (Mft), olenite (Oln), tsilaistite (Tsl), liddicoatite (Ldd), and rossmanite (Rss) (abbreviations for schorl, dravite, elbaite from Whitney and Evans (2010), all others from Morgan (2016). Chemical formulas for pertinent tourmaline species are presented in Table 2-1. Readers are referred to Morgan (2016) for detailed instructions on how tourmaline components are calculated in the spreadsheet. Results from the spreadsheet calculations are tabulated in Appendix 1.

3.4. Secondary Ion Mass Spectrometry (SIMS)

Boron isotopic measurements were made using the Cameca 6f Ion Microprobe at ASU in November 2014 and October 2015. Both analytical sessions used a $^{16}O^-$ primary beam accelerated to -12.5 kV with a sample voltage of +9 kV yielding a total impact energy of 21.5 kV. The energy window was set to accept secondary ions with energies of ±40 eV. The instrument was configured in such a way to achieve a mass resolving power (MRP) greater than 962, which is required to distinguish between the

$^{10}B^{1}H$ and ^{11}B secondary ion signals (for tourmaline, axinite, micas, and danburite), and > 1400, which is required to resolve $^{10}Be^{1}H$ from ^{10}B (for hambergite). The primary beam current was set to between 1 and 5 nA, depending on the concentration of B in the mineral, to yield acceptable count rates for ^{11}B and ^{10}B. A pre-sputter time of 7.5-minute proved adequate to obtain stead-state sputtering conditions. Both ^{11}B and ^{10}B were counted on an electron multiplier with counting times of 4s for ^{10}B and 1s for ^{11}B, to adjust for their natural abundances and improve counting statistics.

The boron and boron isotopic compositions of micas were analyzed during the 2015 session using the same instrument configuration described above, with a few differences. Silicon, ^{28}Si, was counted for 10s on the Faraday cup following the ^{10}B and ^{11}B analysis to allow for the calculation of B using the calibration of Hervig (1996). A current between 2.5 and 5.5 nA and a pre-sputter time of up to 3 minutes provided a stable count rate.

3.4.1. Standardization and Instrumental Mass Fractionation

Dravite, axinite, and illite boron isotopic standards were used in this study to monitor and correct for instrumental mass fractionation (IMF). Analysis of the dravite standard at multiple times daily showed a maximum IMF drift of 5‰ for the October 2015 session and 8‰ for the November 2014 session (Table 2-2). A time-dependent IMF correction factor was developed to correct all analyses of tourmaline. Errors associated differences in spot-to-spot analyses on the standards are less than 2‰. A secondary tourmaline standard, whose boron isotopic composition of -11.8‰ has only been determined by SIMS, was analyzed during the 2014 and 2015 sessions and its composition was reproducible to within the ~ 2‰ external errors observed during both

sessions. Therefore, the boron isotopic compositions of all tourmaline crystals are believed to be accurate to within the ±2‰ external errors.

The axinite standard was analyzed twice immediately before and after 3 analyses of the axinite from the pegmatite. The drift in IMF was less than 2‰ during this short analytical period (Table 2-2). Therefore, axinite analyses are believed to be accurate to within 2‰. The IMF drift for the IMt-1 clay standard during a single day of analyses was less than 4‰, with no systematic variation over time (Table 2-2). The boron isotopic compositions of muscovite and lepidolite are believed to be accurate to within the ±4‰ external errors.

Boron isotopic compositions of hambergite and danburite were standardized using the dravite standard. Consequently, due to possible differences in matrix effects between hambergite, danburite, and tourmaline, values of $\delta^{11}B$ for hambergite and danburite may be inaccurate. Correcting for the isotopic composition of an unknown by using an IMF factor derived from a standard whose structure and composition is significantly different from the unknown has been shown to produce erroneous results (Ludwig et al., 2011; Marschall and Ludwig, 2006).

Raw isotopic ratios derived from SIMS for all crystalline phases from the pegmatites were corrected for IMF, as described below, and converted to delta, δ, notation using the international boron isotope standard, NIST SRM 951 boric acid, with a certified value of 4.04362 (Catanzaro et al., 1970). Internal errors for individual point analyses reported in this study are consistently less than 0.8‰ for all minerals except the micas whose internal errors ranged between 1 and 3‰. The larger internal errors for

the micas likely result from a combination of low concentration of B in the micas and irregularities on the sample surfaces. IMF corrected values of $\delta^{11}B$ for all crystals from each pegmatite are reported in Appendix 1.

4. Results

4.1. Main Dike

4.1.1. Boron isotopic compositions

The complete range of $\delta^{11}B_{Tur}$ from the massive and layered aplites and lower and upper intermediate zones extends from -2.0‰ to +7.5‰ (Table 2-3) and forms a left-skewed, normal distribution with a mean value of +4.7‰ (±3.4‰ 2σSD, N=48) and a median value of 5.1‰ (Fig. 2-4). Of the two elbaite crystals collected from the ’91 London pocket, the crystal with a dark green core and light green cap has a mean $\delta^{11}B$ value of +1.0‰ (±1.0‰ 2σSD, N=7), and shows no systematic isotopic zonation. The mean $\delta^{11}B$ of the second elbaite crystal, including its three-color zones, is +3.1‰ (±1.8‰ 2σSD, N=7), with no systematic internal variation. Values of $\delta^{11}B$ within the single tourmaline extending from the upper intermediate zone into a miarolitic cavity decrease from +6.0‰ (±0.2‰ 2σSD, N=2) at the dark base located in the upper intermediate zone to +2.0‰ (±2.0‰ 2σSD, N=2) at the pink cap in the miarolitic cavity. Hambergite from the ’91 London pocket has an average $\delta^{11}B$ of +20.9‰ (±2.2‰ 2σSD, N=4) and lepidolite has an average $\delta^{11}B$ of -7.9‰ (±3.6‰ 2σSD, N=5).

4.1.2. Chemical compositions

The chemical compositions of tourmaline evolve from $Srl_{40}Ftt_{26}Drv_{14}Mft_{09}Oln_{05}Fuv_{03}Uvt_{01}Tsl_{01}$ in the massive aplite of the footwall to

$Srl_{32}Ftt_{50}Drv_{02}Mft_{03}Oln_{11}Fuv_{01}Uvt_{00}Tsl_{02}$ in the intermediate zone of the footwall. The F contents of tourmaline from the massive and layered aplites and lower and upper intermediate zones are near the detection limit by EMPA (~ 0.1 wt.% F). The transition from intermediate zone to core zone is marked by a sharp increase of Mn, Al, and F in tourmaline (1 to 1.5 wt.% F). The composition of the single tourmaline crystal extending from the upper intermediate zone toward the pocket grades from 67 total mole percent schorl-olenite-foitite to a total 99 mole percent rossmanite-tsilaisite-elbaite-olenite toward the pocket. Tourmaline crystals from the '91 London pocket are a solid solution of tsilaisite, elbaite, and rossmanite with minor foitite and olenite components.

Hambergite from the Main dike has the composition $Be_2BO_3(OH_{0.6},F_{0.4})$ (Novak et al., 1998). The SIMS analyses of B in boromuscovite and in lepidolite were normalized to their Si concentrations using the silica content of boromuscovite from (Foord et al., 1991b) and EMPA for lepidolite. The B contents of lepidolite and boromuscovite are ~200 ppm B and ~15,000 ppm B, respectively.

4.2. Swamp Dike

4.2.1. Boron isotopic compositions

The complete range of $\delta^{11}B_{Tur}$ extends from -0.1‰ to +7.9‰ (Table 2-4). The data display a bimodal distribution with a mean value of +4.0‰ (±5.0‰ 2σSD, N=34) (Fig. 2-5). Boron isotopic data for tourmaline from the massive and layered aplite at the foot wall of the dike form a normal distribution with a mean value of +6.1‰ (±2.2‰ 2σSD, N=18) and a median value of 6.4‰. Values of $\delta^{11}B_{Tur}$ decrease sharply across the transition from layered aplite to the overlying lower intermediate zone. Data from

the lower and upper intermediate zones form a normal distribution with a mean value of +1.7‰ (±2.1‰ 2σSD, N=16) and a median value of +1.9‰. Tourmaline and danburite from a pocket in the Swamp dike have average $\delta^{11}B$ values of +6.7‰ (±2.8‰ 2σSD, N=3) and -5.6‰ (±2.4‰ 2σSD, N=3), respectively.

4.2.2. Chemical compositions

Tourmaline from the lower graphic zone of the Swamp dike are a solid-solution of $Srl_{48}Ftt_{16}Drv_{18}Mft_{06}Oln_{04}Fuv_{04}Uvt_{02}Tsl_{01}$. In the massive and layered aplites, tourmaline have the average composition $Srl_{39}Ftt_{32}Drv_{08}Mft_{07}Oln_{10}Fuv_{03}Uvt_{01}Tsl_{01}$. From the layered aplite toward the core of the pegmatite, tourmalines become more aluminous and manganoan, as indicated by an increase in the olenite-foitite and tsilaisite components, respectively. No other chemical parameter appears to change systematically from margin-to-core of the pegmatite. Tourmaline crystals from the Swamp dike have notably low concentrations of F (<0.09 wt.% F), including tourmaline found in a rare pocket, as compared to the Main dike. Tourmaline from the pocket have the composition $Srl_{49}Ftt_{44}Drv_{01}Mft_{01}Oln_{08}Fuv_{02}Uvt_{00}Tsl_{05}$. Lastly, London et al. (2012) report an end-member composition for danburite ($CaB_2Si_2O_8$: London et al., 2012).

4.3. Spessartine Dike

4.3.1. Boron isotopic compositions

One tourmaline crystal from an intermediate zone of the Spessartine dike (Fig. 2-6, Table 2-5) has an average $\delta^{11}B$ of +4.6‰ (±1.8‰ 2σSD, N=3). The two individual black tourmaline crystals from a miarolitic cavity have mean $\delta^{11}B$ values of +5.7‰ (±0.6‰ 2σSD, N=3) and +5.8‰ (±1.2‰ 2σSD, N=4), respectively. The tourmaline intergrown with axinite has an average $\delta^{11}B$ of +13.8‰ (±4.6‰ 2σSD, N=3) and the

axinite has an average $\delta^{11}B$ of +2.6‰ (±3.0‰ 2σSD, N=3). Muscovite from the same pocket has a $\delta^{11}B$ of -10.1‰ (±4.0‰ 2σSD, N=5). The external tourmalinite has an average $\delta^{11}B_{Tur}$ of -0.1‰ (±3.4‰ 2σSD, N=7).

4.3.2. Chemical compositions

The compositions of individual tourmaline crystals from the intermediate zone are a solid-solution of $Srl_{32}Ftt_{46}Mft_{01}Oln_{16}Fuv_{05}$. Two individual tourmaline from the miarolitic cavity are a solid-solution of $Srl_{35}Ftt_{48}Drv_{01}Oln_{11}Fuv_{02}Tsl_{02}$ and $Srl_{26}Ftt_{16}Drv_{22}Mft_{06}Oln_{08}Fuv_{03}Uvt_{05}Tsl_{13}$, respectively. The tourmaline intergrown with axinite is a solid-solution of $Srl_{09}Ftt_{50}Drv_{00}Mft_{00}Oln_{28}Fuv_{13}Uvt_{00}Tsl_{00}$. The external tourmaline is a solid-solution of $Srl_{25}Ftt_{12}Drv_{14}Mft_{08}Oln_{24}Fuv_{07}Uvt_{04}Tsl_{07}$ and is notably F-rich (0.66 wt.% F) compared to other tourmaline crystals from the Spessartine dike (0.06 to 0.29 wt.% F). Axinite has the composition $Ca_2(Mn_{0.8}Fe_{0.2})Al_2Si_3O_{15}(OH)$ (London et al., 2012). Mica (muscovite) from the miarolitic cavity, analyzed by EMPA in the present study, is a solid-solution of paragonite (~10%) and muscovite (~90%). The B content of muscovite, as determined by SIMS, is ~900 ppm B.

5. Discussion

Two peculiarities emerge concerning the values of $\delta^{11}B_{Tur}$ from the pegmatites of the Little Three mine.

1) the overall $\delta^{11}B_{Tur}$ values are heavier than most other granite-pegmatite systems that have been studied (Fig. 2-7), and
2) the $\delta^{11}B$ of tourmaline across the Main and Swamp dikes tend not to fluctuate as expected based on what is known about fractionation in the system tourmaline-granitic melt-aqueous fluid

5.1. Heavy Isotopic Bulk Composition

There are at least two possible explanations for the heavy isotopic compositions of tourmaline from the pegmatite dikes at the Little Three mine: (1) the system was open to influx or loss of B, such that the pegmatite-forming melt gained ^{11}B or lost ^{10}B, and/or (2) the source of the pegmatite-forming melt was isotopically heavy.

5.1.1. Influx of B into the pegmatites

The host rocks for the Little Three dikes are typical calc-alkaline norite and tonalite of the Peninsular Ranges Batholith (PRB) (Symons et al., 2009); therefore, they are not a source of boron that crystallized within the pegmatites. The norite-tonalite is locally altered to tourmaline at one small meter-scale spot along the contact of the Spessartine dike. Otherwise, the contacts between pegmatites and mafic hosts are sharp and fresh along tens of meters of outcrop strike. Thus, there is enough control by outcrop to state that the host rock is reactive to an influx of boron, but that very little boron escaped from the pegmatite system to the host (London et al., 2012). If correct, then the pegmatites crystallized as essentially closed systems with respect to their hosts, and the bulk isotopic signature of borate (hambergite) and borosilicate minerals in their modal proportion would be close to that of the bulk isotopic system of the pegmatite-forming melt and aqueous solution.

5.1.2. Potential sources of the pegmatite-forming melt

Tourmalines from the Little Three pegmatites differ from other pegmatitic tourmaline in that their $\delta^{11}B$ values are substantially higher than tourmaline from most pegmatites (Fig. 2-7). The full range of $\delta^{11}B_{Tur}$ from granites and pegmatites extends from approximately -27‰ to +9‰ (Palmer and Swihart, 1996; Xiao et al., 2013) with a

prominent mode at ~ -10‰ (Fig. 2-7). The light isotopic signature of tourmaline in these granites and pegmatites is thought to originate from the loss of ^{11}B to an aqueous fluid during dehydration of pelitic rocks with increasing metamorphic grade (Romer and Meixner, 2014a; Rosner et al., 2003). Anatexis of the resultant ^{10}B-enriched metapelitic rock results in an isotopically light granitic magma. The LCT family of pegmatites (Černý and Ercit, 2005) arise from extended fractional crystallization of S-type granitic melt and, compared to pegmatites that originate from other sources, they are characterized by elevated concentrations of Li, Cs, Ta, and P. Therefore, the expectation is that if the pegmatites of the Little Three mine were derived from an S-type granitic source, then they should have boron isotopic and trace element compositions similar LCT pegmatites.

Unpublished analyses of the foot wall and central portions of the Swamp dike reveal exceedingly low concentrations of P (0.04 wt% P_2O_5), Be (1.2 ppm) and Cs (8.4 ppm), and high F in comparison to other dikes that fit the LCT family of trace element signatures. The Swamp dike contains no lithium minerals or beryl, which are sparse even in the more fractionated Main dike. Based on the heavy values of $\delta^{11}B_{Tur}$ in the Little Three pegmatites, the source of the pegmatite-forming melt must have had a heavy boron isotopic composition; thus, a metapelitic source is not likely.

Potential sources of magma for the pegmatites at the Little Three mine are the granitic rocks of the PRB, namely the La-Posta and Corte Madre plutons. The La-Posta pluton, located in the Eastern zone of the PRB, has been suggested to be a potential source of the melt for the pegmatites, based on similar ages (Symons et al., 2009); however, the Corte Madre pluton, a high-silica leucogranite located in the Western

zone, could be a source of melt for the pegmatites due to its proximity to the pegmatites. The pegmatites have K-Ar (Foord et al., 1991a) and paleomagnetic ages (Symons et al., 2009) older than, but slightly overlapping, granitoids of the Eastern PRB (98 to 100 Ma vs 80 to 100 Ma: Symons et al., 2003). The age of the Corte Madre is reported to be 111±2 Ma (Todd et al., 2003), which is ~12 Ma older than the pegmatites. The Corte Madre and La-Posta plutons are characterized as peraluminous, I-type granites based on their chemical and isotopic compositions (ASI ≈1.00-1.20; $Sr_i \leq 0.705$; and $\delta^{18}O \geq 7.2‰$: Todd et al., 2003) and both plutons show a trend of decreasing P_2O_5 with increasing differentiation (Todd et al., 2003). These leucocratic plutons are suitable sources of melt for the Little Three pegmatites based on their peraluminous character and low concentration of P.

Though the Corte Madre and La-Post plutons differ in location and age, both are thought to be products of fractional crystallization of melt generated in the deep-crust or mantle wedge. Todd et al. (2003) and Walawender et al. (1990) proposed that these plutons arose anatexis of material in the deep crust or mantle wedge driven by the influx of water from an underlying oceanic slab. If the pegmatites associated with the PRB resulted from crystallization of a magma generated by the release of fluids emanating from oceanic crust, we would expect the boron isotopic composition of the pegmatites to be similar to that of oceanic crust, assuming there is no loss of B or isotopic fractionation during the transition from melt at the source to emplacement and crystallization of the pegmatites. The $\delta^{11}B$ of altered oceanic crust is heavier than fresh mid-ocean ridge basalt (MORB) (Leeman and Sisson, 1996; Palmer and Swihart, 1996) and is similar to the average $\delta^{11}B$ of the Little Three pegmatites. Therefore, the best

candidate for the heavy $\delta^{11}B$ observed in the Little Three pegmatites appears to have been altered oceanic crust.

5.2. Evaluation of Boron Isotopic Equilibrium among Tourmaline-Melt-Aqueous Fluid

If an equilibrium distribution of boron isotopes between tourmaline and melt was maintained during the crystallization of the Main and Swamp dikes, then the $\delta^{11}B$ of tourmaline from margin-to-core of each pegmatite should follow a pattern similar to one predicted by the Rayleigh equation. However, this assessment hinges upon knowing the value of $\Delta^{11}B_{Tur\text{-}melt}$, which has not been experimentally measured or calculated using first principles methods. If the values for $\Delta^{11}B_{melt\text{-}vpr}$ (Hervig et al., 2002) and $\Delta^{11}B_{Tur\text{-}vapor}$ (Kowalski et al., 2013; Meyer et al., 2008; Palmer et al., 1992) are correct, then an estimate for $\Delta^{11}B_{Tur\text{-}melt}$ can be calculated from these datasets. The calculated value for $\Delta^{11}B_{Tur\text{-}melt}$ is between +8.9‰ and +6.5‰, at 450°C, the temperature of crystallization for the Main and Swamp dikes (London et al., 2012; Morgan and London, 1999). The model shown in Figure 2-8 begins with the compositions of tourmaline form the massive aplite in the footwall and from the upper intermediate zone in the hanging wall of the Main dike. As shown by London et al. (2012) and Morgan and London (1999), the Main and Swamp dikes crystallized inward from the margins such that the core zone crystallized last.

In the Main and Swamp dikes, values of $\delta^{11}B_{Tur}$ form a mostly flat pattern from margin to core of the pegmatite (Fig 2-8). The flat pattern could have resulted from (1) a small value for $\Delta^{11}B_{Tur\text{-}melt}$ (i.e. a small α factor in the Rayleigh equation), or (2) a non-equilibrium distribution of boron isotopes between tourmaline and melt. As shown in Figures 2-8 and 2-9, the patterns of $\delta^{11}B_{Tur}$ from margin-to-core of each pegmatite

does not match the Rayleigh curve that uses a $\Delta^{11}B_{Tur\text{-}melt}$ of +6.5‰. If the value of $\Delta^{11}B_{Tur\text{-}melt}$ is reduced to +1.0‰, the Rayleigh curve becomes more similar to the observed pattern of $\delta^{11}B_{Tur}$.

Unlike the Main dike, there is an abrupt 4.4‰ decrease in $\delta^{11}B_{Tur}$ at the transition from layered aplite to intermediate zone (Fig. 2-9) in the Swamp dike. The abrupt decrease in $\delta^{11}B_{Tur}$ from layered aplite to intermediate zone could not result from an equilibrium distribution of boron isotopes between tourmaline and melt. A loss of ^{11}B from melt to an aqueous fluid is possible if the mass of aqueous fluid was large relative to the mass of melt. Even so, we would expect the $\delta^{11}B$ of tourmaline from the miarolitic cavity to be commensurately heavy compared to tourmaline from the intermediate zone, assuming the experimentally determined values of $\Delta^{11}B_{melt\text{-}vapor}$ are correct. With two exceptions, discussed in section 5.3., the $\delta^{11}B$ of tourmaline from intermediate zones and miarolitic cavities in the Main and Swamp dikes are identical. Textural evidence within the Main and Swamp dikes indicates that an aqueous fluid was present only after the intermediate zones were mostly solidified; small miaroles are present ~10 cm from the larger miarolitic cavities (Morgan and London, 1999). The Swamp dike is essentially massive, with only rare and small miarolitic cavities found at its dike center. In the Swamp dike, systematic variations in Al/Si order and Cs contents of K-feldspar are those expected of an entirely igneous origin, with aqueous fluid present only as the pegmatite approached the core stage of crystallization (London et al., 2012). Therefore, the decrease in $\delta^{11}B_{Tur}$ in the Swamp dike is not likely caused by an enrichment of ^{10}B in melt resulting from the loss of ^{11}B to an exsolved aqueous solution.

5.3. Boron Isotopic Compositions of Tourmaline at the Transition between Intermediate Zone and Miarolitic Cavity

Values of $\delta^{11}B_{Tur}$ from the intermediate zones and miarolitic cavities are virtually identical, with two exceptions (Figs 2-6, 2-8, 2-9). The boron isotopic composition of tourmaline collected from pockets containing B-rich minerals whose B is structurally bound in 4-fold coordination (danburite: Swamp dike; axinite: Spessartine dike) is heavier than tourmaline from the adjacent intermediate zone and, in the Spessartine dike, heavier than other tourmaline crystals from the same miarolitic cavity. In the Spessartine dike, the boron isotopic compositions of three tourmaline crystals from a pocket in the Spessartine dike display a bimodal distribution: two crystals are isotopically similar to tourmaline from massive pegmatite and the third is heavier (Fig 2-6). The heavier tourmaline is intergrown with axinite, whose B is in 4-fold coordination and has a lighter composition than tourmaline.

The $\delta^{11}B$ of tourmaline from the intermediate zones, if crystallized from the melt only, should be substantially lighter than tourmaline formed from aqueous fluid in the miarolitic cavities if miarolitic cavities form from a typical, solute-poor hydrothermal solution (Jahns and Burnham, 1969; Simmons et al., 2012), and the experimental data of Hervig et al. (2002) are applied. The $\delta^{11}B$ of tourmaline in the miarolitic cavities is heavier than in the adjoining massive pegmatite only when danburite or axinite are present in the cavities. The constancy of $\delta^{11}B_{Tur}$ between the intermediate zones and miarolitic cavities signifies that the fractionation of boron isotopes between melt and aqueous fluid is negligible, or that tourmaline in the miarolitic cavities did not crystallize from a typically solute-poor aqueous solution.

London (2013) put forward an argument that crystal-filled miarolitic cavities in pegmatites formed mostly from a dense hydrosilicate liquid that deposited massive clay as the final crystalline material. The heavier composition of tourmaline associated with axinite compared to other individual tourmaline from the same pocket likely derives from local equilibration with axinite through an isotopically heavy fluid. If the principal pocket-forming fluid was a dense, hydrous, and viscous silicate liquid (London, 2013), then $\delta^{11}B_{Tur}$ might reflect only local reaction relationships and locally controlled fractionation of boron's isotopes, as limited by the low diffusivity of boron in viscous melts. This would explain the large disparity in $\delta^{11}B_{Tur}$ among the three tourmaline samples, only one of which is in contact with axinite. Furthermore, the composition of muscovite is ~15‰ lighter than the lightest tourmaline from the miarolitic cavity. If the boron isotopic compositions of muscovite and tourmaline represent a state of equilibrium fractionation, then their boron isotopic compositions should differ by an amount predicted by the fractionation factors for tourmaline-aqueous fluid and muscovite-aqueous fluid. At 450°C, the $\delta^{11}B$ of muscovite and tourmaline should differ by ~7 to ~10‰, which is not the case.

5.4. Alteration of the Host Rock

Localized tourmalinization of the host tonalite has been observed only in one small, meter-scale area along the hanging wall of the Spessartine dike. The source of B for the external tourmaline could only have been the pegmatite; thus, the boron isotopic composition of the external tourmaline must be similar to an aqueous fluid from within the pegmatite. However, the isotopic composition of the external tourmaline is significantly lighter than all other tourmaline in the pegmatites (Figs. 2-6 and 2-7).

Because the progressive crystallization of tourmaline should drive the isotopic composition of an aqueous fluid to heavier values, we would expect the external tourmaline to have a heavier isotopic composition than tourmaline form the miarolitic cavity. However, the timing and temperature of the crystallization of the external tourmaline are not necessarily the same as the initial stage of consolidation within the miarolitic cavities. The light isotopic composition of the external tourmaline could be reconciled to the calculated composition of the aqueous solution in the miarolitic cavities if the wall rock alteration occurred at ≤150°C, using the datasets of Meyer et al. (2008) and Palmer et al. (1992).

5.5. Disequilibrium Processes attending Pegmatite Crystallization

The arguments above rely entirely upon the assumption that equilibrium is maintained during crystallization of boron-bearing minerals and fluids in each pegmatite. All prior studies of boron isotopic fractionation in granite-pegmatite systems implicitly assume that fractionation between and among tourmaline, granitic melt, and aqueous fluid and the resultant $\delta^{11}B$ of tourmaline occurs at an equilibrium state from start to finish. The systematic changes in isotopic composition modeled by the Rayleigh equation utilizes fractionation factors between crystal and bulk melt or aqueous fluid. As shown by Morgan and London (1999), the concentrations of incompatible elements in the Main dike of the Little Three mine are consistent with constitutional zone refining, in which fractionation occurs mostly in the boundary layer of melt adjacent to crystals, not in the bulk melt medium. Therefore, the assumption that equilibrium isotopic fractionation factors can be applied to pegmatites may be inherently flawed due to the conditions, or processes, under which pegmatites form.

Previous studies of the boron isotopic composition of tourmaline from pegmatites did not, however, consider the rapid rates of crystal growth or the low diffusivity of boron through viscous melts at low, pegmatite-forming temperatures (London, 2009, 2008). A thermal cooling model (HEAT3D: Wohletz, 2013) for the Swamp dike shows that the pegmatite, if originally injected as an entirely silicate liquid with an initial temperature of 700°C into host rocks at ~150°C, would reach a core temperature of ~ 450°C after only 7 days; increasing the host rock temperatures by 25°-50°C produces a negligible increase in cooling time. The temperatures derived from feldspar solvus thermometry imply that the crystallization front of the pegmatite advanced from margin to center over this same time frame. If equilibrium is maintained between tourmaline and melt, then the diffusion of B must be fast enough to keep up with the crystallization rate. The diffusivity of B through hydrous granitic melt is ~10^{-12} m^2/s at 800°C (London, 2009; Mungall et al., 1999) and at lower temperature, e.g. 450°C, the diffusivity of B is orders of magnitude slower. Considering a period of 7 days for primary crystallization, and a diffusivity of B orders of magnitude slower than 10^{-12} m^2/s, the growth rate of tourmaline would have far exceeded the diffusivity of B through hydrous granitic melt. Therefore, variations in $\delta^{11}B_{Tur}$ are not the result of Rayleigh fractionation (cf. Siegel et al., 2016; Trumbull et al., 2013), in which the bulk melt is continuously in equilibrium with the distribution of isotopes in tourmaline, but rather due to local effects that include the formation of a chemically distinct boundary layer of melt adjacent to growing crystals (London, 2008, 1992). If the growth rate of tourmaline greatly exceeds the diffusivity of boron through melt, as we predict, then the

boron isotopic composition of tourmaline would be close to that of the bulk melt, and we would expect negligible change in the isotopic composition of tourmaline.

In addition to the arguments mentioned above, boron isotopic compositions of tourmaline in pegmatites that cannot be explained by equilibrium (Rayleigh) crystallization might be the result of a difference in the diffusivity of ^{11}B and ^{10}B. Preliminary data on the diffusivity of boron's isotopes comes from experiment CGB2 (Fig. 2-10), conducted at 800°C and 200 MPa as described and presented in London (2009). As expected, ^{10}B diffused farther, hence faster, than did ^{11}B, with a 6‰ difference in their apparent diffusivities over a distance of ~ 2 mm. Similarly, the diffusivities of the light isotopes of Li and Ca have been shown to diffuse faster than their heavier isotopes (Richter et al., 2003). Therefore, if $\Delta^{11}B_{Tur\text{-}melt}$ is large and positive and ^{10}B diffuses faster than ^{11}B, the expectation is that values of $\delta^{11}B_{Tur}$ across a pegmatite would become increasingly light; much more so than Rayleigh fractionation would predict.

6. Summary and Concluding Remarks

The results from this study highlight the fact that an equilibrium distribution of boron isotopes is unlikely during the crystallization of pegmatites. If an equilibrium distribution of boron isotopes between tourmaline and granitic melt is not attained, then the boron isotopic composition of magmatic tourmaline should be close to the ratio of isotopes in the bulk melt. In that case, the isotopic composition of tourmaline from pegmatites should reflect the character of the magmatic source of the pegmatite. Differences in the diffusivity of boron isotopes through viscous silicate melt, in relation to the rate of advance of the tourmaline-bearing crystallization front, may also play a

role in the few sharp variations and minor oscillations of boron isotope compositions that have been observed in this study.

Importantly, a system in which there is no fractionation of boron isotopes because of kinetic factors is indistinguishable from a system in which there is no fractionation of isotopes at equilibrium (e.g. Tonarini et al., 1998). Until the systematics of $\Delta^{11}B_{melt\text{-}fluid}$ and $\Delta^{11}B_{Tur\text{-}melt}$ are better calibrated via carefully executed experiments, the boron isotopic composition of tourmaline from pegmatites will remain a poorly understood indicator of internal processes of pegmatite formation.

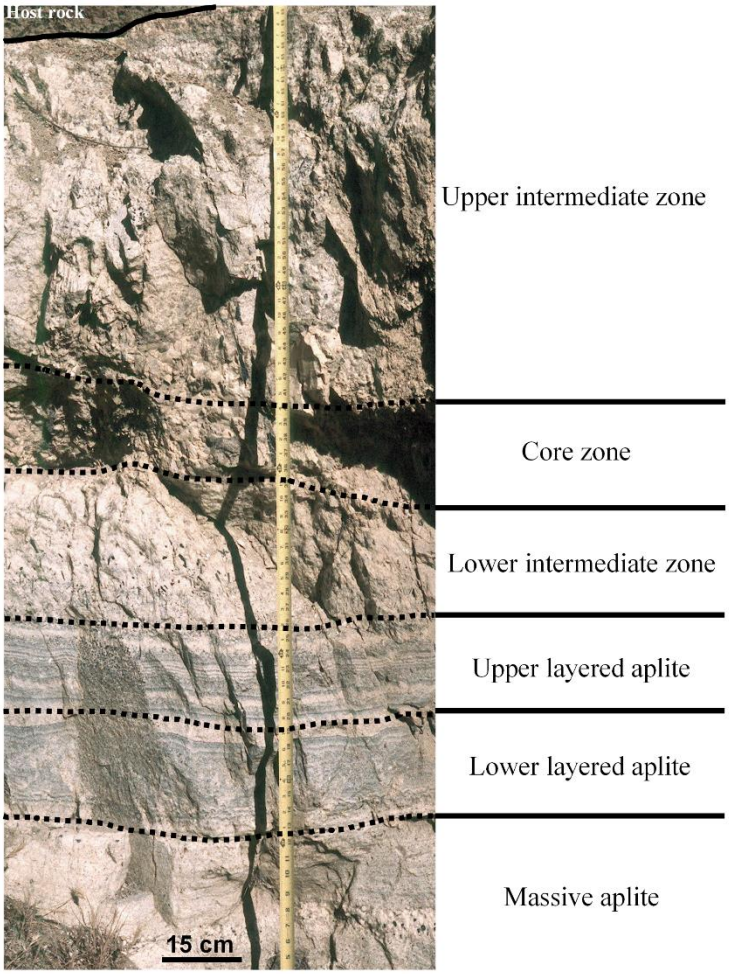

Figure 2-1 Photograph of Main dike outcrop. Pegmatite zones labeled in figure. A detailed discussion of the mineralogic zonation is presented in section 2.2

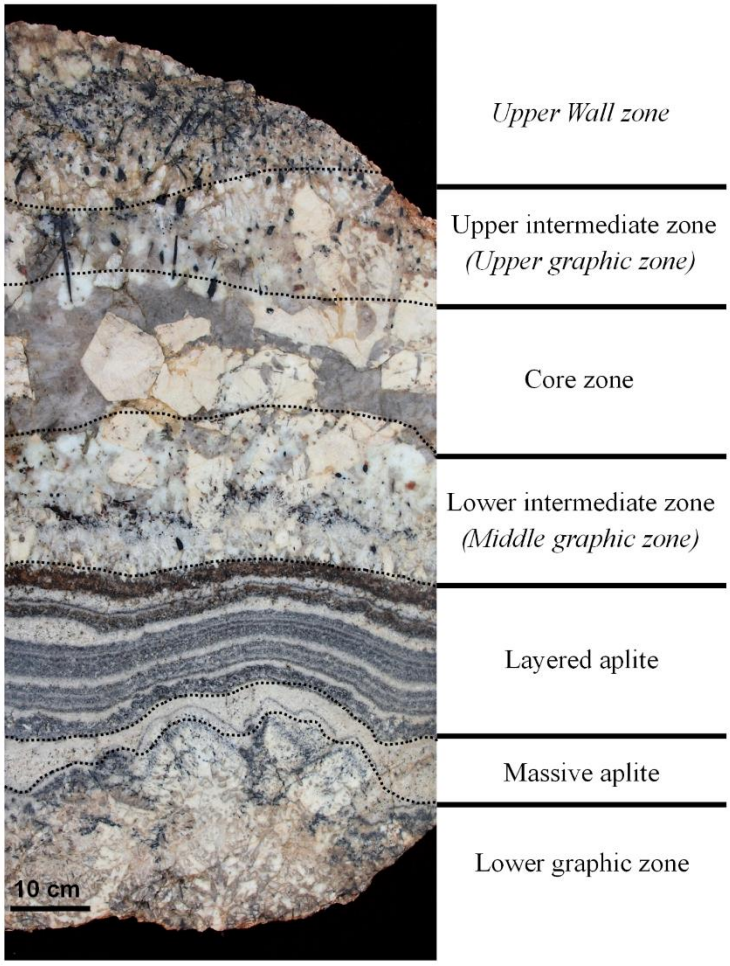

Figure 2-2 Photograph of a polished cross-section of the Swamp dike showing textural zonation and pegmatitic-zones. Italicized text, both in and out of parentheses, is from London et al. (2012). Non-italicized text outside parentheses is the nomenclature for zones used in the present study.

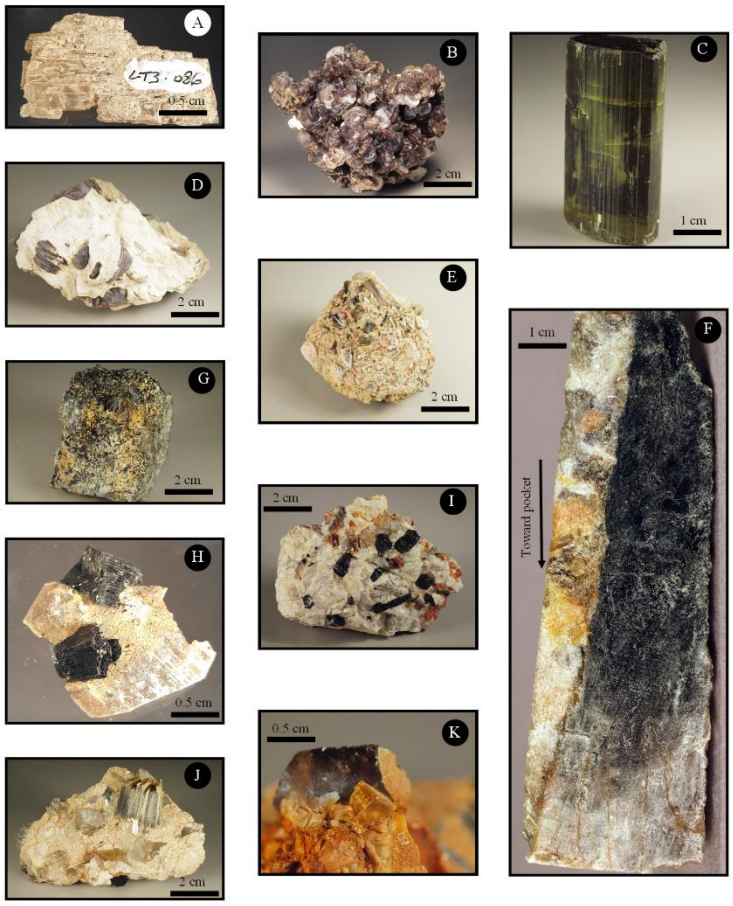

Figure 2-3 Photographs of pocket mineralogy from the Main dike (A-F), Spessartine dike (G-J), and Swamp dike (K). (A) Hambergite. (B) Lepidolite. (C) Green elbaite. (D) Boromuscovite (bright white coating) on muscovite. (E) Fine-grained polychromatic elbaite. (F) Single tourmaline crystal extending from intermediate zone into pocket. (G) Fine-grained external tourmaline (tourmalinite). (H) Tourmaline intergrown with axinite. (I) Tourmaline-, muscovite-, garnet-bearing massive pegmatite from intermediate zone. (J) Muscovite on albite and quartz. (K) Danburite (yellow/orange crystal in center of image) on quartz.

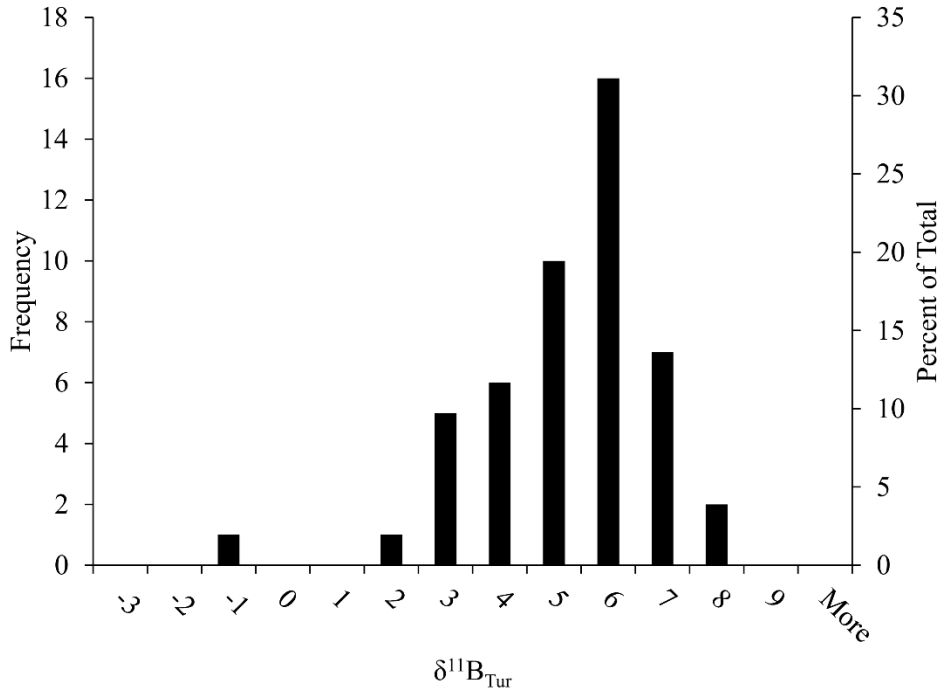

Figure 2-4 Histogram of $\delta^{11}B_{Tur}$ values for tourmaline from the footwall and hanging wall sections of the Main dike.

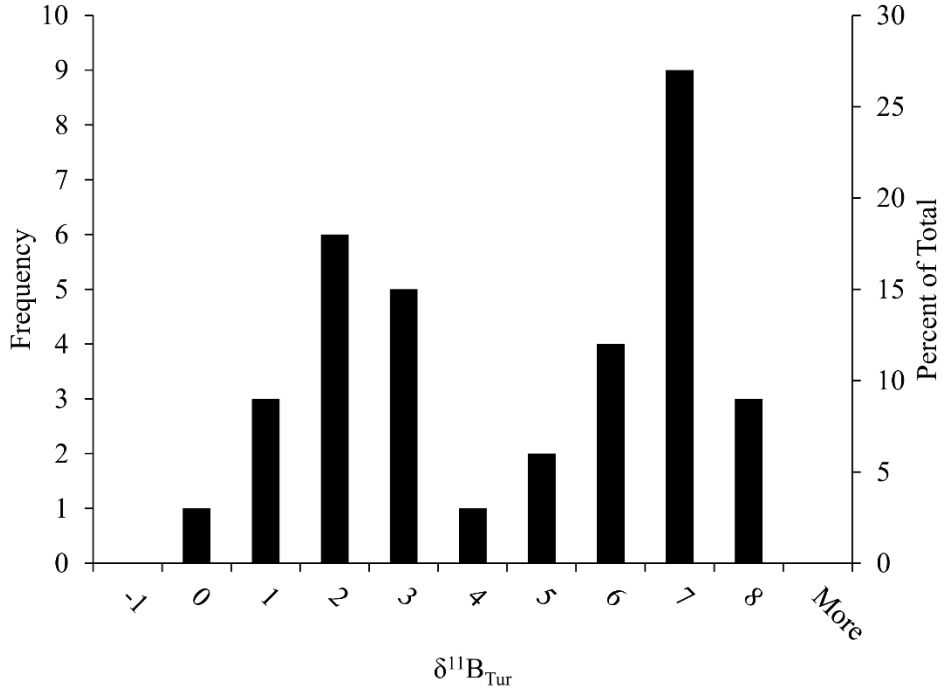

Figure 2-5 Histogram of $\delta^{11}B_{Tur}$ values for tourmaline from the footwall and hanging wall sections of the Swamp dike.

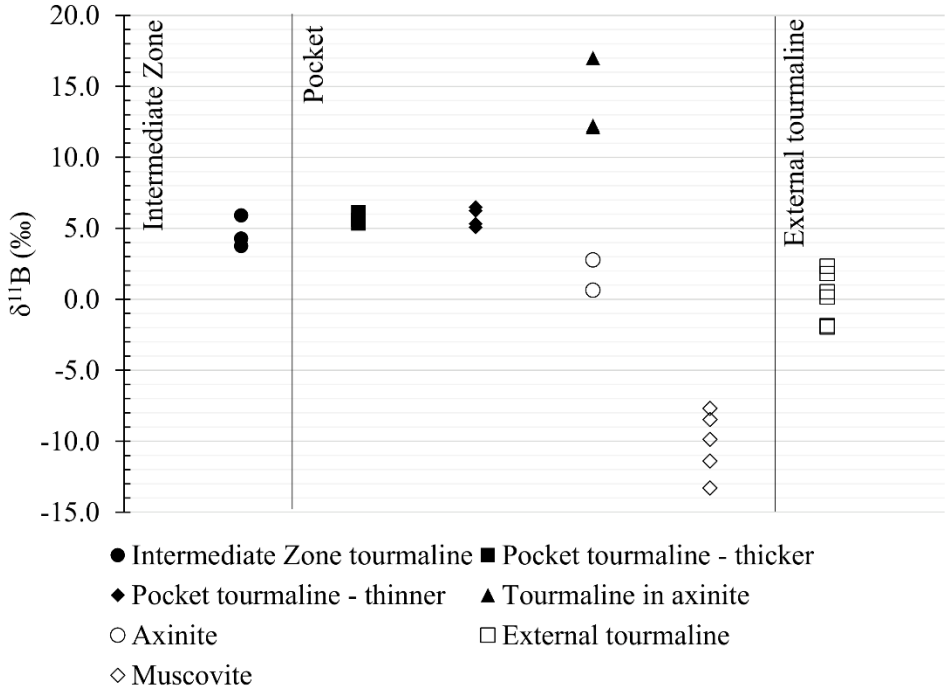

Figure 2-6 Boron isotopic compositions of tourmaline, muscovite, and axinite from the Spessartine dike. Individual symbols represent individual analyses. Error bars are smaller than the size of the symbol. Units along the x-axis are arbitrary.

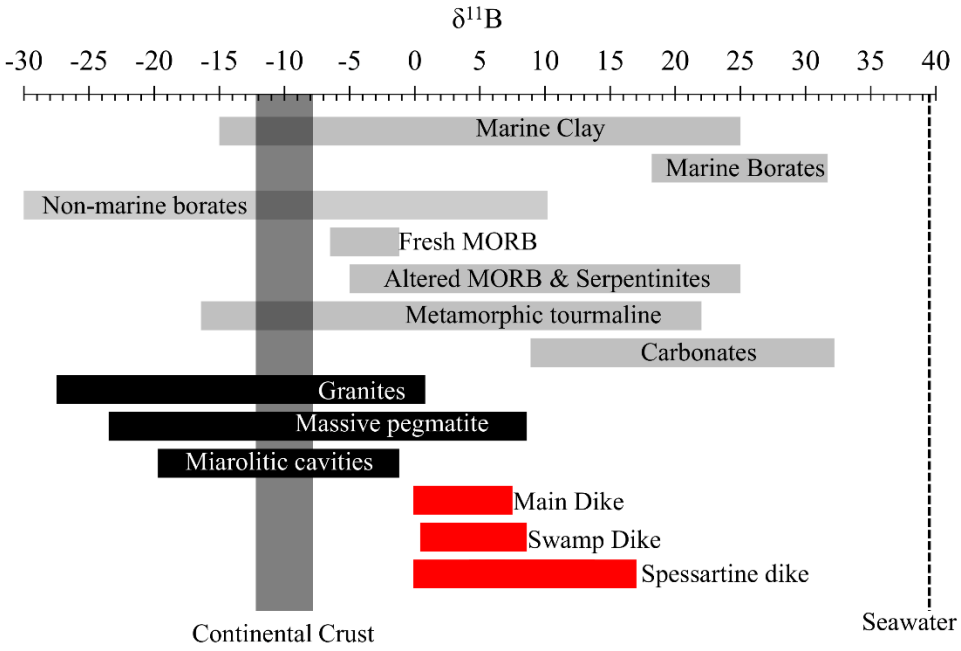

Figure 2-7 Boron isotopic compositions of various geological materials (data from Palmer and Swihart, 1996; Xiao et al., 2013).

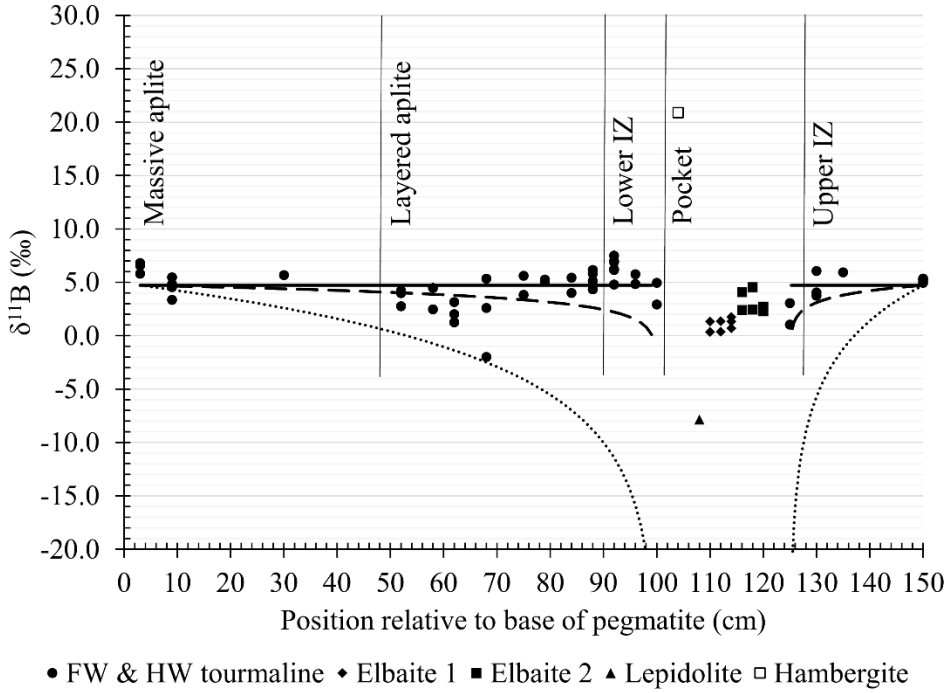

Figure 2-8 Boron isotopic compositions of tourmaline, hambergite, and lepidolite from the Main dike as a function of their location relative to the base of the pegmatite. 'IZ' refers to the intermediate zone. 'FW" refers to footwall and 'HW' refers to hanging wall. Elbaite 1 has a dark green core and light green rim. Elbaite 2 has a dark green base, light green rim, and a light pink cap. Dotted, black line represents a Rayleigh fractionation model for $\delta^{11}B_{Tur}$ based on a $\Delta^{11}B_{Tur\text{-}melt}$ of +6.5‰. Dashed, black line represents a Rayleigh model for $\delta^{11}B_{Tur}$ based on a $\Delta^{11}B_{Tur\text{-}melt}$ of +1.0‰. Solid, black line represent the average $\delta^{11}B$ value for tourmaline across the footwall and hanging wall sections of the pegmatite. Each symbol represents an individual analysis. Errors are smaller than the symbol size.

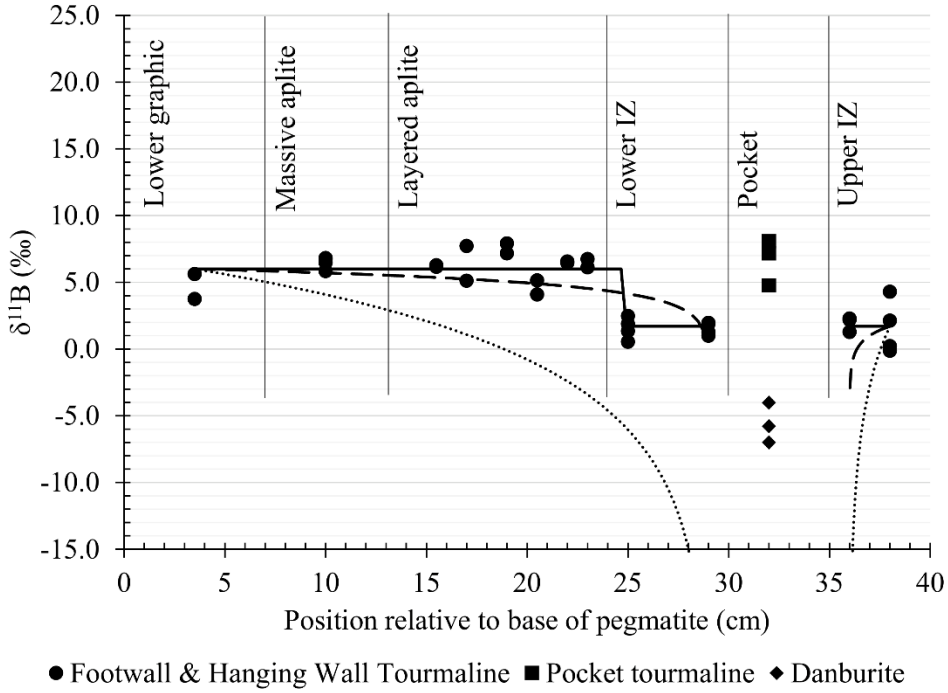

Figure 2-9 Boron isotopic compositions of tourmaline, danburite, and muscovite from the Swamp dike as a function of their location relative to the base of the pegmatite. 'IZ' refers to the intermediate zone. Dotted, black line represents a Rayleigh fractionation model for $\delta^{11}B_{Tur}$ based on a $\Delta^{11}B_{Tur\text{-}melt}$ of +6.5‰. Dashed, black line represents a Rayleigh fractionation model for $\delta^{11}B_{Tur}$ based on a $\Delta^{11}B_{Tur\text{-}melt}$ of +1.0‰. Solid, black line represent the average $\delta^{11}B$ value for tourmaline across the footwall and hanging wall sections of the pegmatite. Each symbol represents an individual analysis. Internal errors are smaller than the symbol size.

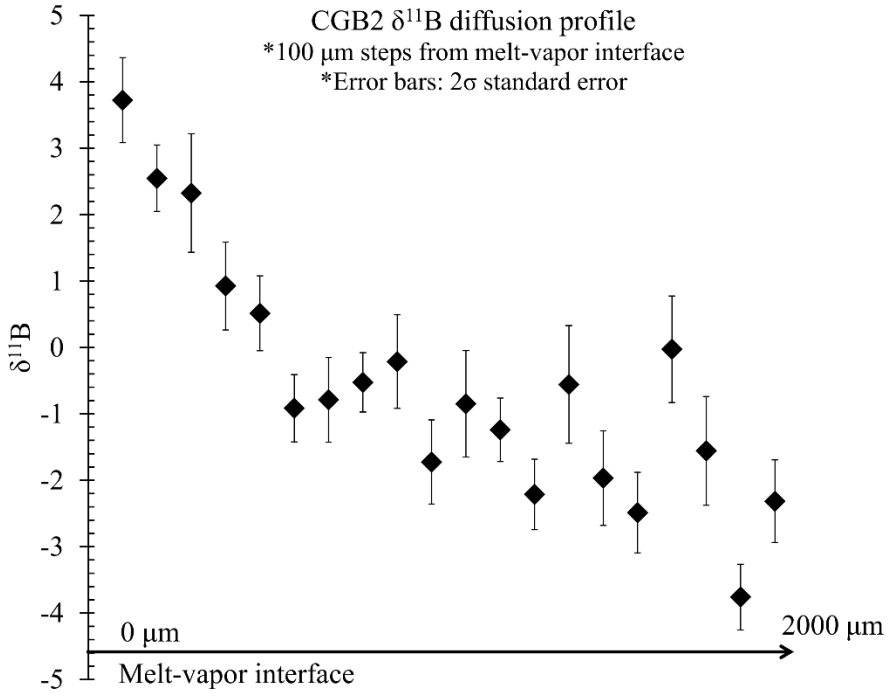

Figure 2-10 SIMS $\delta^{11}B$ profile across B-diffusion profile in hydrous, metaluminous haplogranite glass (experiment CGB2). Internal errors per individual point analyzed (represented as vertical error bars in the diagram) are 2σ standard error of the mean.

Table 2-1 Tourmaline species and chemical formulae

Mineral	Abbreviation	Formula
Schorl	Srl	$NaFe_3Al_6(BO_3)_3Si_6O_{18}(OH)_3OH$
Dravite	Drv	$NaMg_3Al_6(BO_3)_3Si_6O_{18}(OH)_3OH$
Tsilaisite	Tsl	$NaMn_3Al_6(BO_3)_3Si_6O_{18}(OH)_3OH$
Feruvite	Fuv	$CaFe_3(Al_5Mg)(BO_3)_3Si_6O_{18}(OH)_3OH$
Uvite	Uvt	$CaMg_3(Al_5Mg)(BO_3)_3Si_6O_{18}(OH)_3OH$
Olenite	Oln	$NaAl_3Al_6(BO_3)_3Si_6O_{18}((OH)O_2)O$
Foitite	Ftt	$\square(Fe_2Al)Al_6(BO_3)_3Si_6O_{18}(OH)_3OH$
Magnesio-foitite	Mft	$\square(Mg_2Al)_3Al_6(BO_3)_3Si_6O_{18}(OH)_3OH$
Elbaite	Elb	$Na(Li_{1.5}Al_{1.5})Al_6(BO_3)_3Si_6O_{18}(OH)_3OH$
Rossmanite	Rss	$\square(LiAl_2)Al_6(BO_3)_3Si_6O_{18}(OH)_3OH$
Liddicoatite-OH	Ldd	$Ca(Li_2Al)Al_6(BO_3)_3Si_6O_{18}(OH)_3OH$

□ represents site vacancy, abbreviations for schorl, dravite, and elbaite from Whitney and Evans (2010), all others from Morgan (2016)

Table 2-2 Standard Data and IMF for SIMS

Dravite standard ($^{11}B/^{10}B = 4.0169$)

Tourmaline

Date	$^{11}B/^{10}B$ (raw)	α IMF	$\delta^{11}B$ (‰)	Error (‰)
11/19/2014	3.9108	0.9736	-6.4	0.5
11/19/2014	3.9091	0.9732	-6.8	0.4
11/19/2014	3.9081	0.9729	-7.1	0.5
11/19/2014	3.9120	0.9739	-6.1	0.4
11/19/2014	3.9263	0.9775	-7.1	0.4
11/19/2014	3.9310	0.9786	-5.9	0.4
11/19/2014	3.9214	0.9762	-8.3	0.4
11/20/2014	3.9194	0.9757	-5.8	0.3
11/20/2014	3.9185	0.9755	-6.0	0.4
11/20/2014	3.9231	0.9767	-4.8	0.3
11/20/2014	3.9085	0.9730	-8.5	0.4
Average	3.9171	0.9752	-6.6	
1σ StDev	0.0079	0.0020	1.1	
Ext Rep (‰)			2.0	

Danburite/Tourmaline

Date	$^{11}B/^{10}B$ (raw)	α IMF	$\delta^{11}B$ (‰)	Error (‰)
11/21/2014	3.9377	0.9803	-6.1	0.5
11/21/2014	3.9313	0.9787	-7.8	0.5
11/21/2014	3.9251	0.9772	-9.3	0.5
11/21/2014	3.9208	0.9761	-10.4	0.6
11/21/2014	3.9333	0.9792	-7.2	0.5
11/21/2014	3.9221	0.9764	-10.1	0.6
Average	3.9284	0.9780	-8.5	
1σ StDev	0.0068	0.0017	1.7	
Ext Rep (‰)			1.7	

Hambergite

Date	$^{11}B/^{10}B$ (raw)	α IMF	$\delta^{11}B$ (‰)	Error (‰)
11/21/2014	3.8751	0.9647	-6.3	0.4
11/21/2014	3.8786	0.9656	-5.4	0.4
Average	3.8769	0.9651	-5.8	
1σ StDev	0.0024	0.0006	0.6	
Ext Rep (‰)			0.6	

Table 2 cont.

Ferroaxinite standard ($^{11}B/^{10}B$ = 4.0181)

Axinite

Date	$^{11}B/^{10}B$ (raw)	α IMF	$\delta^{11}B$ (‰)	Error (‰)
11/20/2014	3.8910	0.9684	-7.2	0.5
11/20/2014	3.8916	0.9685	-7.0	0.4
11/20/2014	3.8912	0.9684	-7.1	0.4
11/20/2014	3.9036	0.9715	-4.0	0.5
Average	3.8944	0.9692	-6.3	
1σ StDev	0.0062	0.0015	1.6	
Ext Rep (‰)			1.6	

Dravite ($^{11}B/^{10}B$ = 4.0169)

Tourmaline

Date	$^{11}B/^{10}B_{(raw)}$	α IMF	$\delta^{11}B$ (‰)	Error (‰)
10/12/2015	3.8538	0.9594	-6.5	0.6
10/12/2015	3.8516	0.9589	-7.0	0.5
10/12/2015	3.8529	0.9592	-6.7	0.4
10/12/2015	3.8505	0.9586	-7.3	0.4
10/12/2015	3.8529	0.9592	-6.7	0.9
10/12/2015	3.8557	0.9599	-6.0	0.8
10/12/2015	3.8558	0.9599	-6.0	0.9
10/13/2015	3.8510	0.9587	-8.1	0.6
10/13/2015	3.8560	0.9599	-6.8	0.6
10/13/2015	3.8602	0.9610	-5.7	0.6
10/13/2015	3.8563	0.9600	-6.7	0.5
10/13/2015	3.8579	0.9604	-6.3	0.6
10/13/2015	3.8587	0.9606	-6.1	0.7
10/14/2015	3.8608	0.9611	-5.0	0.8
10/14/2015	3.8665	0.9626	-3.5	0.6
10/14/2015	3.8609	0.9612	-5.0	0.6
10/14/2015	3.8616	0.9613	-4.8	0.7
10/14/2015	3.8522	0.9590	-7.2	0.7
10/14/2015	3.8522	0.9590	-7.2	0.7
10/14/2015	3.8495	0.9583	-7.9	0.8
10/14/2015	3.8451	0.9572	-9.1	0.6
10/14/2015	3.8522	0.9590	-7.2	0.8
10/14/2015	3.8453	0.9573	-9.0	0.6
Average	3.8548	0.9596	-6.6	
1σ StDev	0.0066	0.0016	1.7	
Ext Rep (‰)			1.7	

Table 2 cont.: Standard Data and IMF for 2015 SIMS - Micas

IMt-1 ($^{11}B/^{10}B = 4.00723$)

Date	$^{11}B/^{10}B_{(raw)}$	α IMF	$\delta^{11}B$	Error (‰)	$^{11}B/^{28}Si$
10/15/2015	3.8677	0.9652	-8.3	1.7	0.00123
10/15/2015	3.8630	0.9640	-9.5	1.8	0.00121
10/15/2015	3.8738	0.9667	-6.7	1.8	0.0012
10/15/2015	3.8591	0.9630	-10.5	2.2	0.00119
10/15/2015	3.8771	0.9675	-5.9	1.8	0.00126
10/15/2015	3.8484	0.9604	-13.2	1.9	0.00121
10/15/2015	3.8564	0.9624	-9.3	1.3	0.00124
10/15/2015	3.8510	0.9610	-10.7	1.3	0.00128
10/15/2015	3.8780	0.9678	-3.7	1.7	0.00122
10/15/2015	3.8550	0.9620	-9.6	1.2	0.00134
10/15/2015	3.8468	0.9600	-11.7	1.5	0.00130
Average	3.8339	0.9567	-9.0		0.0013
1σ StDev	0.0357	0.0089	2.2		0.00007

Table 2-3 Boron isotopic compositions of minerals from the Main Dike

Mineral	Sample ID	Location	HAB*	$\delta^{11}B$	2σSD	N
Tourmaline	2	Massive Aplite	3	6.4	0.9	3
"	3	"	9	4.5	1.5	4
"	4	"	30	5.7	---	1
"	5c	Layered Aplite	52	3.6	1.3	3
"	5d	"	58	3.5	2.0	2
"	5e	"	62	2.1	1.6	3
"	5f	"	68	2.0	6.1	3
"	6a	"	75	4.7	1.8	2
"	6b	"	79	5.2	0.2	2
"	6c	"	84	4.7	1.4	2
"	6d	"	88	5.4	1.4	4
"	6e	"	92	6.4	1.7	6
"	6f	Lower Intermediate Zone	96	5.3	1.3	2
"	6g	"	100	3.9	2.9	2
"	Elbaite1 (grn/lt grn)	Pocket	100-135	1.0	1.0	7
"	Elbaite2 (grn)	"	100-135	3.5	2.0	2
"	Elbaite2 (lt grn)	"	100-135	3.2	1.8	2
"	Elbaite2 (pnk)	"	100-135	2.5	0.4	2
Lepidolite	Lepidolite	"	100-135	-7.9	3.6	5
Hambergite	Hambergite	"	100-135	20.9	2.2	4
Tourmaline	7a	Upper Intermediate Zone	150	6.0	0.1	2
"	7b	"	145	5.9	0.0	1
"	7c	"	140	2.0	2.0	2
"	8	"	150	5.2	0.3	5

HAB: Height above base of pegmatite (cm)

Table 2-4 Boron isotopic compositions of minerals from Swamp Dike

Mineral	Sample ID	Location	HAB*	$\delta^{11}B$	2σSD	N
Tourmaline	KD1	Lower graphic	3.5	4.7	1.9	2
"	KD2	Massive aplite	10	6.5	0.8	4
"	KD3	Layered aplite	15.5	6.2	0.1	2
"	KD4	"	17	6.4	2.6	2
"	KD5	"	19	7.5	0.7	2
"	KD6	"	20.5	4.6	1.1	2
"	KD7	"	22	6.5	0.1	2
"	KD8	"	23	6.4	0.6	2
"	KD9	Lower Intermediate Zone	25	1.6	1.4	4
"	KD10	"	29	1.5	0.8	4
"	Black Tourmaline	Pocket	30-35	6.7	2.8	3
Danburite	Danburite	"	30-35	-5.6	2.4	3
Tourmaline	KD11	Upper Intermediate Zone	36	2.0	0.8	4
"	KD12	"	38	1.6	3.5	4

HAB: Height above base of pegmatite (cm)

Table 2-5 Boron isotopic compositions of minerals from Spessartine Dike

Mineral	Sample ID	Sample Location	$\delta^{11}B$	2σSD	N
Tourmaline	Herc	Intermediate Zone	4.6	1.8	3
"	LT3core	Pocket	5.7	0.6	3
"	LT3pen	"	5.8	1.2	4
"	TurAx	"	13.8	4.5	3
Axinite	LT3 Ax	"	2.6	3.0	3
Muscovite	MsE	"	-10.1	4.0	5
Tourmaline	SD_ExoTur	Exomorphic	-0.1	3.4	7

Chapter 3 Diffusivities of B, ^{11}B, and ^{10}B in hydrous, granitic melt at 800°C and 200 MPa: Implications for the mass transfer of B and its isotopes in natural systems

1. Introduction

The boron isotopic composition of tourmaline, $\delta^{11}B_{Tur}$, in granites and pegmatites has been used to assess (1) the role and state of water during the primary phase of magmatic crystallization, (2) the assimilation of various geologic materials into granitic melt, and (3) the source materials of granitic melts (Maner and London, 2017; Siegel et al., 2016; Tonarini et al., 1998; Trumbull et al., 2013; Trumbull and Chaussidon, 1999). Most prior studies of $\delta^{11}B_{Tur}$ from granites and pegmatites have assumed that the $\delta^{11}B$ of tourmaline represents an equilibrium distribution of boron isotopes between tourmaline and the melt or aqueous solution from which it grew (cf. Maner and London, 2017). This is an essential condition for the application of Rayleigh modeling of isotopic compositions of minerals and melts (White, 2013). However, diffusion-limited, kinetically controlled fractionation of isotopes between crystals and melt can yield compositions for minerals and melt that differ substantially from compositions predicted by an equilibrium model (Jambon, 1980; Richter et al., 2003; Watson and Müller, 2009). Therefore, it is necessary to evaluate the diffusivity of boron and its isotopes in granitic melt, and then to assess the presumption of equilibrium isotopic fractionation between tourmaline and is growth media.

The diffusivity of boron in granitic melt has been measured through various experimental methods and in a variety of melt compositions (Baker, 1992; Chakraborty

et al., 1993; London, 2009; Mungall et al., 1999). In granitic compositions, diffusion coefficients for B are smaller (faster) in hydrous melts (10^{-8} m^2/s at 1300°C: Mungall et al., 1999) compared to anhydrous melts (10^{-15} m^2/s at 1300°C: Baker, 1992). Only two studies have measured diffusion coefficients for B at temperatures less than 1200°C (London, 2009; Mungall et al., 1999), and London (2009) is the only study to report a diffusion coefficient for B (10^{-12} m^2/s) at 800°C and 200 MPa in hydrous granitic melt.

Diffusion through silicic melt is an efficient process by which to separate isotopes of a given element (Richter et al., 1999). Richter et al. (2003) measured diffusion coefficients for the isotopes of Ca and Li at 1350°C to 1450°C, 1.2-1.3GPa, in anhydrous rhyolite-basalt couples. They found that the difference in diffusivity of the heavy and light isotope was greatest for Li (~ 40‰) and smallest for the Ca (~ 6‰). Chakraborty et al. (1993) found no difference in the diffusivity of ^{11}B and ^{10}B in granitic melt at 1400°C and 1 atm. However, the proportionately large mass differences between ^{11}B and ^{10}B means that they should have different diffusion coefficients, especially at the much lower temperatures of crystallization in granites and their pegmatites.

Thus, the $\delta^{11}B$ signature of tourmaline in granites and pegmatites may result from two kinetic effects. The rate of diffusion of B through melt relative to the rate of growth of tourmaline may be so slow that there is no fractionation of isotopes between tourmaline and melt. In that case, the $\delta^{11}B$ values of tourmaline would not vary with the progress of crystallization, and $\delta^{11}B_{Tur}$ would simply record that value of the bulk melt. If ^{10}B and ^{11}B can be effectively separated from one another via diffusion through

granitic melt, then values of $\delta^{11}B_{Tur}$ in granitic rocks might be vary as crystallization proceeds, but not in accord with the equilibrium distribution of isotopes.

In this study, we report results from experiments designed to evaluate the diffusivity of boron and its isotopes in hydrous granitic melt at 800°C and 200 MPa. Diffusion coefficients are calculated from concentration-distance profiles using two different diffusion equations and two different experimental designs. All combinations of experimental design and calculations yield a consistent value for the diffusion coefficient, D_B that is similar to the value reported by London (2009). In the only two experiments that contained both ^{10}B and ^{11}B added as a single source, we document significant diffusive fractionation of the isotopes through melt. We consider the implications of the diffusion data for boron and its isotopes on the isotopic composition of fluids exsolving from granitic melt and on the isotopic composition of tourmaline in granites and pegmatites.

2. Methods

2.1. Experimental Designs

Two experimental designs were implemented in this study to measure the diffusivity of boron and its isotopes in granitic melt. The first design, from London (2009), entails the diffusion of boron from a B-rich aqueous solution into B-free glass. In these experiments, B was added as boric acid with an unknown boron isotopic ratio. London (2009) used this design to measure the diffusivity of B in hydrous, granitic melt at 800°C and 200 MPa (experiment # CGB2). In this manuscript, we report B isotopic data from the same experiment. The second method, referred to as the diffusion-couple

method, involves stacking two glasses. In this method, the pairs of glass wafers we chose to investigate include:

(1) A B-bearing glass (with a mixed isotope ratio) with a B-free glass,

(2) two B-bearing glasses with different isotopic compositions (^{11}B in one, ^{10}B in the other), and

(3) a B-bearing glass wafer, enriched in either ^{10}B or ^{11}B, with a B-free glass wafer.

2.2. Experimental methods

Four different glass compositions were used in this study. The first glass, which also served as the starting composition for all other glasses, was designed to match the thermal minimum in the hydrous, metaluminous haplogranite system at 200 MPa_{H2O} (CG and HG: Table 3-1). The second and third glasses contain ~ 10 wt.% B_2O_3 as ^{11}B and ^{10}B, respectively (^{11}BHG and ^{10}BHG: Table 3-1). The fourth glass consists of ~ 5 wt.% B_2O_3 with a mixture of ^{11}B and ^{10}B (HGB5: Table 3-1). Each starting material glass was prepared by fusing chemical reagents in Pt dishes in a Deltech bottom-loading furnace at 1600°C for 1 to 4 hours; the resulting glass plates were ~ 3 mm thick. Quenched B-bearing glasses were aphyric and trapped few air bubbles. The B-free glass is aphyric and contains abundant air bubbles. Chips of glass were analyzed by an electron microprobe for their chemical composition and to assess their chemical homogeneity. Upon creating a homogeneous glass, cores measuring 3 x 3 mm were drilled from each glass plate. Several glass cores were hydrated to ~ 6 wt.% H_2O prior to their use in diffusion experiments in case the diffusivity of B depends on the water

content of melt. Hydrous and anhydrous glass cores were cut into ~ 1 mm thick circular wafers for final experimentation.

Gold capsules were loaded with stacked glass wafers, such that their cut surfaces touched, forming a cylinder. Capsules were weighed before and after the addition of each component to record the mass of each component and sealed using a TIG-welder. Sealed capsules were loaded into NIMONIC 105 cold-seal reaction vessels and heated to 800°C and 200 MPa for zero to 28 days. The zero-day experiment was quenched immediately upon reaching the target temperature. Experiments were quenched nearly isobarically at an average rate of ~30°C/min to room temperature. All capsules were weighed again after quench to check for leaks produced during the experiment. Capsules showing no signs of leakage were prepared for chemical and/or isotopic analyses.

2.3. Preparation of glasses for analysis

Glasses were sectioned and mounted in 1" circular molds using EpoThin™ (Beuhler) epoxy. Molds were initially ground using diamond-embedded plates on a lapidary wheel followed by a polish using a combination of diamond-embedded films. A final, fine-finish polish was applied to each sample using a series of solutions containing 3 µm to ¼ µm diamond grit. Polished mounts were cleaned, dried, and coated with either C (for EMPA) or Au (for SIMS) prior to analysis.

2.4. Electron microprobe (EMPA)

The Cameca SX-100 at the University of Oklahoma was used to chemically characterize all glasses. Glasses were analyzed for Si, Al, K, Na, and B using a 2-

condition analytical routine. The first condition used a 10 kV accelerating voltage, 2 nA beam current, and 20 µm spot diameter to analyze Si, Al, K, and Na. The second condition used the same accelerating voltage and spot size, but a 40 nA beam current to analyze B. Individual point analyses were separated by a distance of 50 µm to 100 µm. Detection limits for Si, Al, Na, and K are ~ 0.1 wt.% oxide, and ~ 0.5 wt.% for B_2O_3. Data reduction used the PAP method (Pouchou and Pichoir, 1985).

2.5. Secondary ion mass spectrometry (SIMS)

Boron concentrations and boron isotopic ratios were measured using the Cameca 6f secondary ion mass spectrometer (SIMS) at the Arizona State University. The SIMS instrument was setup to measure ^{11}B, ^{10}B, and ^{30}Si for 1s each using an energy window offset of -75 V and a window of ± 20 V. The total impact energy was 21.5 kV with a primary ion beam current between 1 and 5 nA. Boron isotopic ratios were measured using a similar instrument setup as reported by Maner and London (2017). All boron isotopic ratios are reported using standard units (‰) and isotopic notation, using the zero point reference of Catanzaro et al. (1970).

Boron content was calculated using a calibration curve developed for this study using SIMS signals for ^{10}B, ^{11}B, and ^{30}Si on hydrous and anhydrous glasses. Standards include six hydrous, granitic glasses (E10, B5, 2.5AN, 2.5FN, 5AN, 5CN: Table 3-2), the Macusani obsidian (MAC: Table 3-2), and three glasses from the Johns Manville company (JM253, JM902, JM901F: Table 3-2). The B contents of glasses E10 and B5 were analyzed at Activation Laboratories (Ancaster, Ontario) using wet-chemical (ICP) methods. Glasses 2.5AN, 2.5FN, 5AN, 5CN were analyzed using an electron microprobe. The B content of MAC is from (London et al., 1988). The Johns Manville

company provided compositional data for each of the JM glasses. The sum of the $^{11}B/^{30}Si$ and $^{10}B/^{30}Si$ ratios was multiplied by the SiO_2 content of the glass and plotted against the B content (in ppm). The result is a single linear array ($r^2 = 0.99$) through the data (Fig. 3-1).

3. Calculation of a diffusion coefficient from concentration-distance profiles

3.1. Pertinent diffusion terminology

The experiments were designed to measure the movement of B from B-bearing liquid into B-free liquid, and inter-diffusion of B isotopes between two liquid reservoirs. Chemical gradients exist in the former experiments, whereas, in the latter experiments, ^{10}B and ^{11}B are exchanged from opposing liquid reservoirs with nearly identical B content. Where chemical gradients do exist, the movement of atoms from the high concentration reservoir to the low concentration reservoir is termed chemical diffusion. Where chemical gradients do not exist, the transfer of isotopes between two reservoirs has been referred to as self-diffusion (Mungall et al., 1999).

Diffusion coefficients can be calculated from concentration versus distance profiles in chemical- and self-diffusion experiments. However, selecting the proper model by which to effectively describe concentration-distance data depends on whether diffusion of the element of interest is associated with other elements (multi-component diffusion), or only the single element in question (binary diffusion). We elected to treat the diffusion of B in terms of a binary diffusion problem because, aside from B content, the major element compositions of each starting material glass are similar to one another.

3.2. Pertinent diffusion equations

Effective binary (chemical) diffusion and self-diffusion coefficients are calculated from concentration-distance profiles using the inverse error function (1) and Boltzman-Matano (2) equations (Crank, 1975).

$$(1)\ C = C_O erfc \frac{x}{2\sqrt{(Dt)}}$$

$$(2)\ D_{C=C1} = -\frac{1}{2t}\frac{dx}{dC}\int_0^{C1} x dC$$

The following conditions must be met to obtain accurate solutions to each equation: (1) the concentration of the diffusing component (diffusant) must remain constant, i.e. at its starting concentration, in the melt region at the beginning of the diffusion profile, and (2) the concentration of the diffusant must attain background levels before reaching the end of the diffusant-free melt region. The durations of experiments in this study were short enough to prevent complete equilibration of B throughout the melt region, but long enough to produce concentration-distance profiles with sufficient length to produce accurate models.

The inverse error function and Boltzman-Matano equations differ in that the former does not account for changes in diffusivity as a function of the concentration of the diffusant. If the diffusant changes the properties of the liquid in ways that influence its diffusivity, then the Bolzman-Matano equation provides a more accurate numerical representation of the diffusion coefficient. For the Boltzman-Matano solution, all concentration-distance data were fit to the mathematical expression that most closely matches the data. All concentration-distance profiles were fit to 3rd-order polynomial expressions, which produced high correlation coefficients between the modeled and

measured data ($r^2 > 0.94$). The inverse error function was solved by making trial-and-error estimations of a diffusion coefficient until the calculated concentration-distance profile closely matched the measured data. A goodness-of-fit statistical evaluation allows comparison of the calculated and measured concentration-distance profiles, which provides an unbiased means by which a diffusion coefficient could be selected to solve the inverse error function equation.

4. Results

4.1. Chemical compositions of glasses

The concentrations of Al_2O_3, Na_2O, and K_2O are constant within measurement by EMPA across each diffusion profile (Figures 3-2 and 3-3). The concentration of SiO_2, however, decreases into the high-B melt region (Figure 3-2 and 3-3). Note that the initial concentrations of SiO_2 in the HGB5 and HG glasses (Table 3-1) are not the same. Therefore, the difference in the concentration of SiO_2 from one melt region to another is controlled by differences in the initial concentrations of SiO_2 in each starting material (i.e. not a result of multi-component diffusion).

The water (H_2O) content of each glass, as determined by difference of EMPA totals from 100%, is zero for the single anhydrous experiment and between ~ 6 and 8 wt% in hydrous experiments. A gradient in water content was observed in one experiment (CGB91: Figure 3-2); however, this is most likely a result of small differences in the amount of water added to glass cores during the pre-hydration step. Water was found to be completely homogenized (across ~ 2 mm of glass) in less than 1 hr, and B had not noticeably diffused from one wafer into the other (CGB34).

Therefore, the diffusion of B should not depend on whether glasses began hydrated or were hydrated during the B diffusion experiment.

4.2. Directionality of B diffusion

Calculation of a diffusion coefficient requires comprehensive knowledge of the direction in which B moves from one region of melt into another. In experiments that used the diffusion-couple design, which includes the chemical- and self-diffusion experiments, measured concentration-distance profiles are very similar in multiple profiles across the two-glass interface. In contrast, concentration-distance profiles measured in experiment CGB2, which did not use the same diffusion-couple design, differ substantially depending on the location of the transect across the glass. For CGB2, the directionality of the diffusion of B was assessed by measuring more than 500 EMPA data points across the half of the glass surface adjacent to the boric acid source. The data were incorporated into SigmaPlot 13.0 (Systat Software), smoothed using a locally weight smoothing (LOESS) method, and then plotted as concentration of B versus the X and Y dimensions of the glass. The data (Figure 3-4) show that B diffused from all sides of the glass (melt) cylinder. Moreover, it is clear from the data in Figure 3-4 that the distance B moved through melt from the cylinder walls is shorter than from the end of the core. Therefore, for experiment CGB2, we chose to use data from a profile down the center of the glass along its long axis, the same direction of profile utilized by London (2009).

4.2. Diffusion coefficients for B

Diffusion coefficients for B are between ~ 10^{-13} m^2/s and 10^{-14} m^2/s in all experiments (CGB2 and the new experiments presented here) using chemical- and self-

diffusion couples (Table 3-3). Diffusion coefficients calculated using the inverse error function are similar to the slowest (smallest) diffusion coefficients calculated using the Boltzman-Matano equation (Tables 3-3 and 3-4). For instance, as shown in Figure 3-5 for experiment CGB2, the diffusion coefficient used to solve the inverse error function equation produces the best match to the concentration-distance data toward the left-hand side of the profile. The data on the left-hand side of Figure 3-5 corresponds to the slowest (smallest) diffusion coefficient calculated using the Boltzman-Matano equation.

Note that the diffusion coefficients calculated from some experiments using the Boltzman-Matano equation change by an order of magnitude as a function of position along all concentration-distance profiles; compare BM(min) and BM(max) in Table 3-4. The diffusion coefficients do not appear to correlate with any chemical parameter, e.g. the concentration of B_2O_3. Diffusion coefficients calculated using the Boltzman-Matano equation are sensitive to the slope of the regression through the data. All concentration-distance profiles were fit to 3rd-order polynomial expressions, and the fit between the expression and the data is good (high r^2 values: Table 3-4). Therefore, it is unlikely that the variability of the diffusion coefficients for B are related to the data fitting method. However, the coefficients in each 3rd-order polynomial expression are different for each experiment due to differences in concentration-distance profiles as a result of experiment duration. Therefore, the variability of calculated diffusion coefficients along a concentration-distance profile most likely stems from small changes in the slope of concentration-distance data.

4.3. Diffusion coefficients for ^{10}B and ^{11}B

Diffusion coefficients for ^{10}B and ^{11}B in hydrous granitic melt are on the order of ~ 10^{-13} m^2/s, whereas, in anhydrous granitic melt, diffusion coefficients are on the order of ~ 10^{-14} m^2/s (Tables 3-3 and 3-4). Figure 3-6 displays an example of the measured $^{11}B/^{30}Si$ (CGB49: Table 3-3) from which chemical diffusion coefficients were calculated. Self-diffusivities for ^{11}B and ^{10}B (Table 3-4) were calculated from similar concentration-distance data (Figs. 3-7a and 3-7b). Self- and chemical-diffusivities for ^{10}B and ^{11}B are very similar to one another and to chemical diffusivities for B (Tables 3-3 and 3-4).

4.4. Diffusive separation of ^{10}B and ^{11}B

Experiments CGB2 and CGB96 employed a single mixed isotopic source of boron from laboratory reagent boric acid. Though different batches of material, the starting glasses in both experiments were synthesized to match the minimum composition of hydrous haplogranite at 200 MPa H_2O ($Ab_{38}Or_{29}Qtz_{33}$). Both experiments were conducted at 800°C, 200 MPa. Experiment CGB2 was performed for 6 days, and the concentration of B_2O_3 in glass ranges from ~20 wt.% to 0 wt.% over ~ 1600 μm. Experiment CGB96 was held at temperature for 21 days; this is a diffusion-couple experiment, in which B diffuses from one glass wafer into a B-free glass wafer. The concentration of B_2O_3 in CGB96 ranges from ~3 wt.% to 0 wt.% over ~ 800 μm.

Boron isotopic analyses of glasses from CGB2 and CGB96 reveal an enrichment of ^{10}B relative to ^{11}B in the direction of decreasing B concentration (Figs 3-8 and 3-9). The $\delta^{11}B$ of melt (glass) decreases ~ 6‰ in CGB2 (Fig. 3-8) and ~ 25‰ in CGB96 over 1600 μm (Fig. 3-9). Both experiments display slight undulations or plateaus in $\delta^{11}B$

along the length of the diffusion profile. These are not the result of experimental or analytical effects as far as can be known. However, they do not negate the principal observation that the rate of diffusion of ^{10}B was substantially faster than was ^{11}B in both experiments. Differences in diffusivity of the isotopes lead to very large fractionation effects along the diffusion profiles, even (or especially) at the relatively high temperatures of these experiments.

5. Discussion

5.1. Low diffusivity of boron in hydrous granitic melts

All measured diffusion coefficients for boron in these hydrous granitic melts at 800°C, 200 MPa H_2O, are in the range of 10^{-13} to 10^{-14} m^2/s. These include the coupled self-diffusion experiments (Table 3-4), which contained 10-11 wt% B_2O_3 added to hydrous haplogranite composition. The low diffusivity of boron in these experiments is surprising, considering that the addition of several weight percent of boron and other fluxes to hydrous granite liquids at comparable P-T conditions resulted in melt viscosities from 3 to 60 Pa·s (Bartels et al., 2011). The measured diffusion coefficients for boron are similar to those of Al in hydrous haplogranite at the same P-T conditions (Acosta-Vigil et al., 2002), in which Al exists almost entirely in four-fold coordination (Xue and Kanzaki, 2007). However, and for comparison, the calculated viscosity of the granitic melt in which Acosta-Vigil et al. (2002) measured the diffusivity of Al is ~ 10^4 Pa·s (from Baker, 1996).

5.2. Kinetic fractionation of isotopes via diffusion

The two experiments reported here, CGB2 and CGB96, in which boron was added as a single mixed source, produced extensive fractionation of ^{10}B and ^{11}B along

the diffusion profile, with the lighter ^{10}B diffusing at a faster rate. The higher diffusivity of ^{10}B conforms to theoretical and experimental expectations as observed in other light isotope systems (e.g., Li: Richter et al., 2003). These results with Li (Richter et al., 2003) and B (this study) are consistent with a model for diffusive fractionation of light isotopes (Watson and Müller, 2009). In their model, Watson and Müller (2009) show that the compositions of crystals and their growth media differ from an equilibrium composition as determined by

(1) the rate of crystallization relative to the diffusivity of the isotopes (R/D),

(2) the relative diffusivities of the isotopes,

(3) the thickness of a boundary-layer liquid at the interface of the growing crystal, and

(4) the elemental partition coefficient between crystal and melt.

Their model predicts that diffusion-limited kinetics dictates the distribution of isotopes between a crystal and its growth medium when the crystal growth rate, R, is fast in relation to the diffusivity of the isotopes in question, D, and especially when the elemental partition coefficient deviates significantly from unity. Moreover, the kinetic fractionation and boundary-layer effects are greater for unidirectional (1-dimensional) crystal growth than for spherical (2-dimensional) crystallization, because the interfacial surface area remains constant in the first case but increases in the second case. In granites and pegmatites, tourmaline exhibits strongly 1-dimensional and unidirectional (base to tip) growth habits in highly undercooled and viscous granitic systems.

6. Applications to geologic systems: Degassing of granitic liquid and crystallization of tourmaline

Boron isotopic fractionation factors in the system tourmaline-aqueous solution were reported by Meyer et al. (2008) and Palmer et al. (1992). Results of both studies indicate that tourmaline is isotopically lighter than the aqueous solution from which it crystallizes. Hervig et al. (2002) indicate that an aqueous solution will be isotopically heavier than its coexisting granitic melt. Based on these data, and an assumption of equilibrium distributions of the isotopes in all cases, tourmaline that crystallizes from melt should be isotopically heavier than melt. The result is two populations of $\delta^{11}B$ values for tourmaline, such those that crystallize from aqueous solution should be heavier than those that crystallize from melt. Siegel et al. (2016) and Trumbull et al. (2013) interpreted a decrease in the $\delta^{11}B$ of tourmaline from core to rim of single crystals to result from exsolution of H_2O from melt and loss of ^{11}B from melt to aqueous solution. Alternatively, if $\Delta^{11}B$ for tourmaline-melt is positive, then the continuous crystallization of tourmaline from melt should also result in a decrease of $\delta^{11}B$ from core to rim, irrespective of the exsolution of aqueous solution from melt.

Though equilibrium between tourmaline and aqueous solution is likely due to the rapid diffusivity of B in solution (Ildefonse et al., 1979), equilibrium between tourmaline and melt is unlikely based on the results reported in this study for the diffusivity of B and its isotopes in hydrous granitic melt. For example, London et al. (2012) calculated a rate of cooling for a tourmaline-rich pegmatite near Ramona, California, that required the crystallization front to advance into melt at the rate of a few centimeters per day. At the low temperature of crystallization of this dike, ~ 450°C, the

diffusivity of B through melt should be approximately zero. Maner and London (2017) observed little to no variation in the average values of $\delta^{11}B_{Tur}$ from an aplitic unit into a miarolitic cavity. For this reason, Maner and London (2017) concluded that the isotopic composition of tourmaline in the massive portion of the pegmatite was that of the bulk melt, and that essentially no fractionation had occurred across the tourmaline-melt and melt-aqueous solution interfaces. Tonarini et al. (1998) found the same constancy of $\delta^{11}B$ from massive pegmatite into a miarolitic cavity across a narrow pegmatite dike from Elba, Italy. However, they construed this as an equilibrium distribution of isotopes, and on that basis proposed that the equilibrium value of $\Delta^{11}B_{Tur\text{-}melt}$ is zero.

The isotopic separation of ^{10}B from ^{11}B via diffusion as reported here is applicable when a large chemical gradient in B is suddenly imposed on the melt. In the event that an aqueous solution rapidly exsolves from melt, we would expect the melt adjoining the aqueous fluid to become enriched in ^{11}B, as the greater diffusivity of ^{10}B depletes its concentration in the melt. Koga et al. (2011) reported precisely these results from experiments that entailed the rapid degassing of rhyolitic magma. They noted a strong depletion of ^{10}B in glass along interfaces with bubbles, much greater than any plausible equilibrium value. Therefore, they appear to have described the same kinetic fractionation as has been demonstrated here, wherein ^{10}B diffuses faster than ^{11}B through granitic melt.

7. Concluding Remarks

Based on the experimental calibrations to date, and these are incomplete at present, the utilization of the $\delta^{11}B$ signature of tourmaline in granite-pegmatite systems is fraught with complexity. From an initial $\delta^{11}B$ value for granitic melt, tourmaline

should be heavier than the melt from which it crystallizes, but get lighter with the progress of crystallization from melt alone. Aqueous fluid that exsolves from granitic melt should be isotopically heavier than melt (Hervig et al., 2002), but the magnitude of that fractionation remains in doubt (e.g., Maner and London, 2017; Siegel et al., 2016; Trumbull et al., 2013). Tourmaline that crystallizes from aqueous solution will be lighter than that solution (Meyer et al., 2008; Palmer et al., 1992) and get heavier with continued crystallization (Marschall et al., 2009). Thus, the isotopic compositions of tourmaline that crystallizes from melt and from aqueous solution should diverge away from one another with the progress of crystallization. The kinetic fractionation of ^{10}B from ^{11}B as reported here and in the degassing experiments by Koga et al. (2011) have the opposite effect, leading to an isotopically lighter fluid and heavier melt.

At the pegmatite-forming temperature of ~ 450°C, the value of $\Delta^{11}B_{\text{melt-aqueous solution}}$ is -15.2‰ based on the results of Hervig et al. (2002), and $\Delta^{11}B_{\text{Tur-aqueous solution}}$ is -2.4‰ (Meyer et al., 2008) to -4.9 (Palmer et al., 1992). In this case, the values of $\delta^{11}B$ in tourmaline crystallized from aqueous solution should be significantly heavier than for tourmaline crystallized from melt if isotopic equilibrium prevails. In contrast, if the fractionation of boron isotopes between melt and aqueous fluid is diffusion-controlled, as shown here and by Koga et al. (2011), then $\Delta^{11}B_{\text{melt-aqueous solution}}$ will initially possess a positive value. Thus, the two fractionation trends, one kinetic and one toward equilibrium, might offset to the extent that little isotopic fractionation occurs between melt and aqueous solution. It is notable, then, that three studies of $\delta^{11}B$ of tourmaline show no significant change in isotopic values from tourmaline in massive pegmatite to

tourmaline that crystallized in miarolitic cavities (Maner and London, 2017; Tonarini et al., 1998; Trumbull et al., 2013).

Add to this complexity the exceedingly low chemical diffusivity of boron through melt, and the large fractionation of ^{10}B from ^{11}B along boron concentration gradients in melt (e.g., between B-rich boundary layer liquids and a B-poorer bulk melt: London, 2008) and at melt-vapor interfaces (Koga et al., 2011). The cumulative results are those of no fractionation due to low diffusivity of B, and opposing trends in isotopic fractionation between kinetic effects and equilibrium trends. In their comprehensive survey, Trumbull et al. (2013) observed that mean values of $\delta^{11}B_{Tur}$ did not vary from the source granitic plutons to the miarolitic stage of the most fractionated pegmatite dikes of their study region in northeastern Brazil, yet $\delta^{11}B_{Tur}$ varied by as much as 20‰ within a single body. Based on the study of diffusivity presented here, we suggest that neither of these results is expected or accountable as an equilibrium distribution of boron isotopes among granitic melt, aqueous solution, and tourmaline.

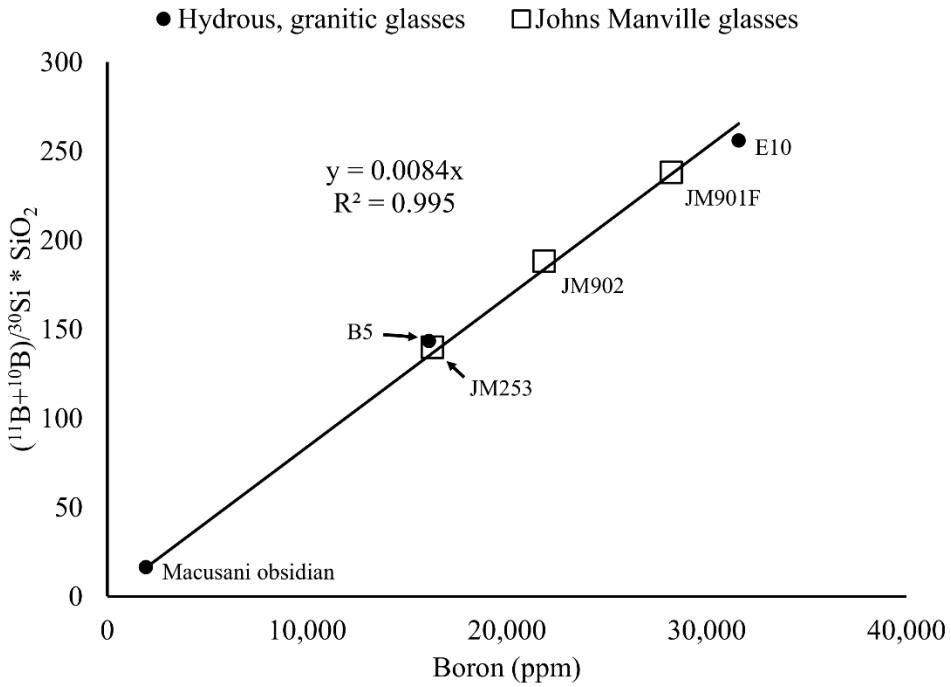

Figure 3-1 Calibration curve for calculating B content. See section 2.5 in text for details.

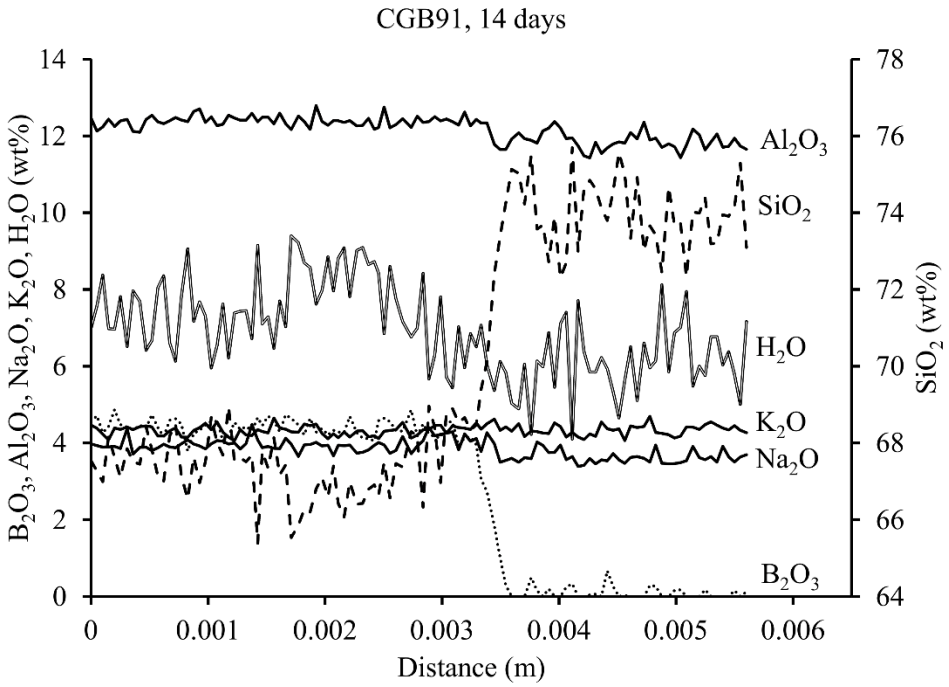

Figure 3-2 Chemical composition (wt% oxides) of glass from experiment CGB91 as a function of distance (m) across the glass. Experiment CGB91 was held at 800°C for 14 days. The starting glasses differ in that one is B-free and the other contains ~ 5 wt% B_2O_3 (HGB5: Table 1). The concentrations of Al_2O_3, Na_2O, K_2O, and H_2O do not vary across the glass. Where the concentration of B_2O_3 is highest (left-hand side), the concentration of SiO_2 is lowest, and vice versa.

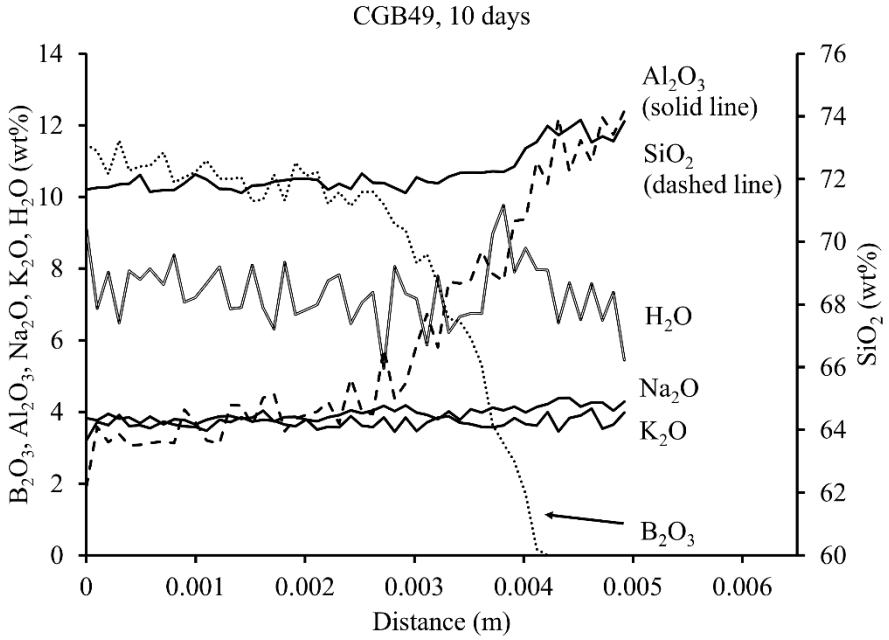

Figure 3-3 Chemical composition (wt% oxides) of glass from experiment CGB49 as a function of distance (m) across the glass. Experiment CGB49 was held at 800°C for 10 days. The starting glasses differ in that one is B-free and the other contains ~ 10 wt% B_2O_3 (11BHG: Table 1). The concentrations of Al_2O_3, Na_2O, K_2O, and H_2O do not vary across the glass. Where the concentration of B_2O_3 is highest (left-hand side), the concentration of SiO_2 is lowest, and vice versa.

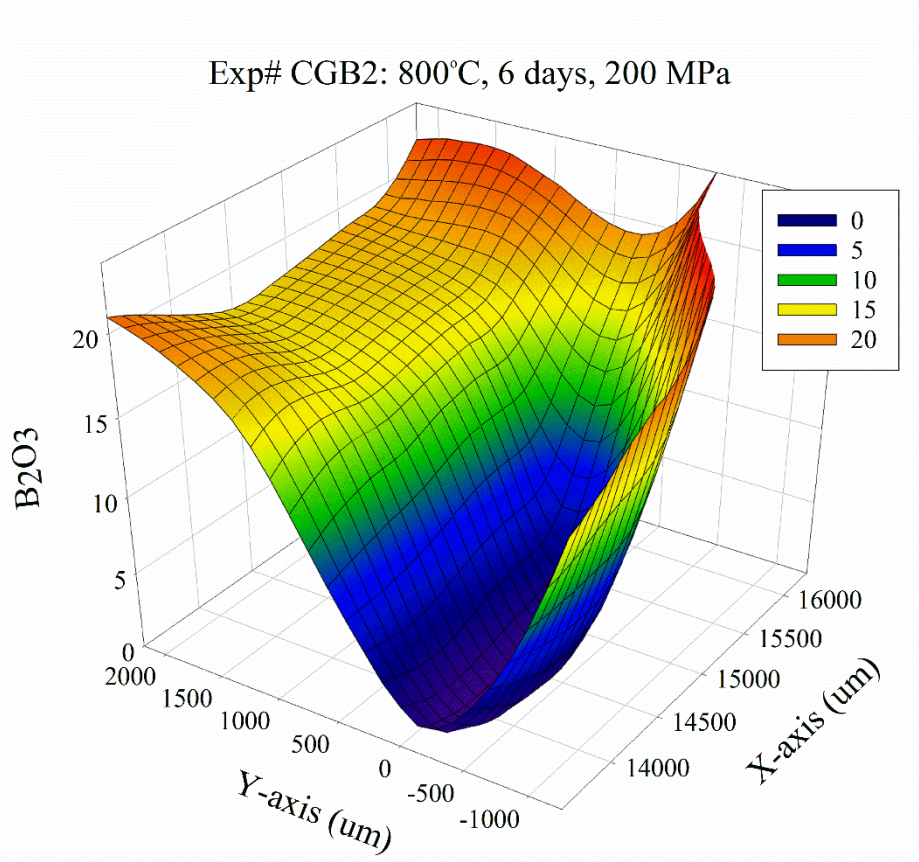

Figure 3-4 3-D plot of B concentration in glass from experiment CGB2 (Table 3). Plots represents a collection of over 500 EMPA data points that were smoothed using a loess based algorithm in SigmaPlot 13.0 (Systat Software). Units for the z-axis are weight percent (wt.%) and micrometers (μm) for the x- and y-axes. The illustration clearly shows that B diffused from the sides and end of the glass cylinder.

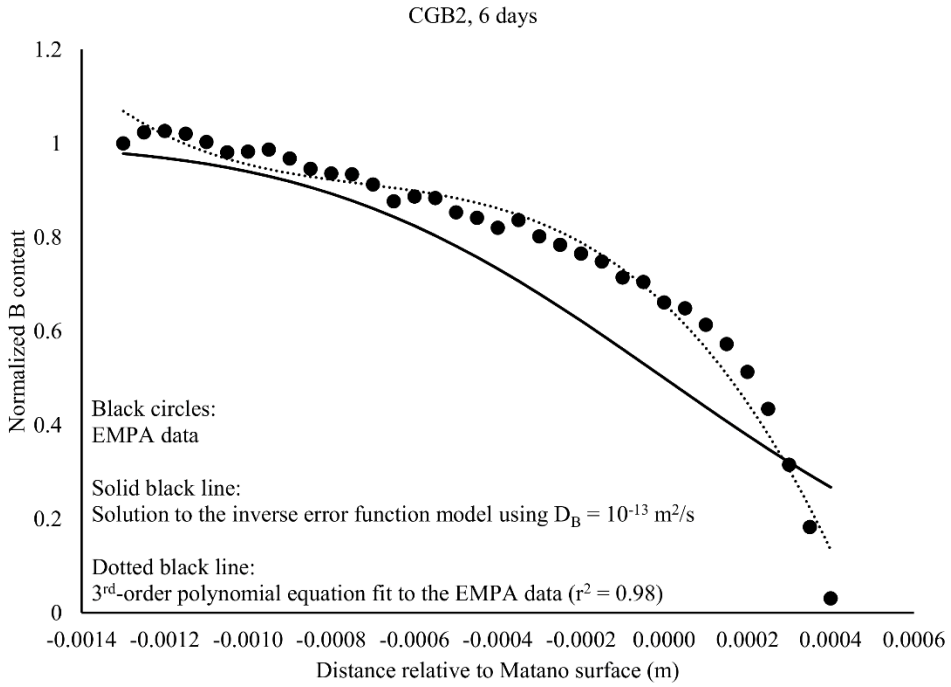

Figure 3-5 Normalized B content of glass in experiment CGB2 against distance (meters) relative to the Matano surface. Circles are EMPA data. Solid line represents a solution to the inverse error function using a diffusion coefficient for B of 10^{-13} m^2/s. Dotted line represents 3rd-order polynomial expression fit to the EMPA data. Diffusion coefficients were calculated using the Boltzman-Matano equation from the 3rd-order polynomial expression. Diffusion coefficients calculated using both equations are similar for the high concentration end (higher y-axis values). At lower concentrations, the diffusion coefficient calculated using the Boltzman-Matano equation is an order of magnitude smaller (faster) than the coefficient used in the inverse error function equation.

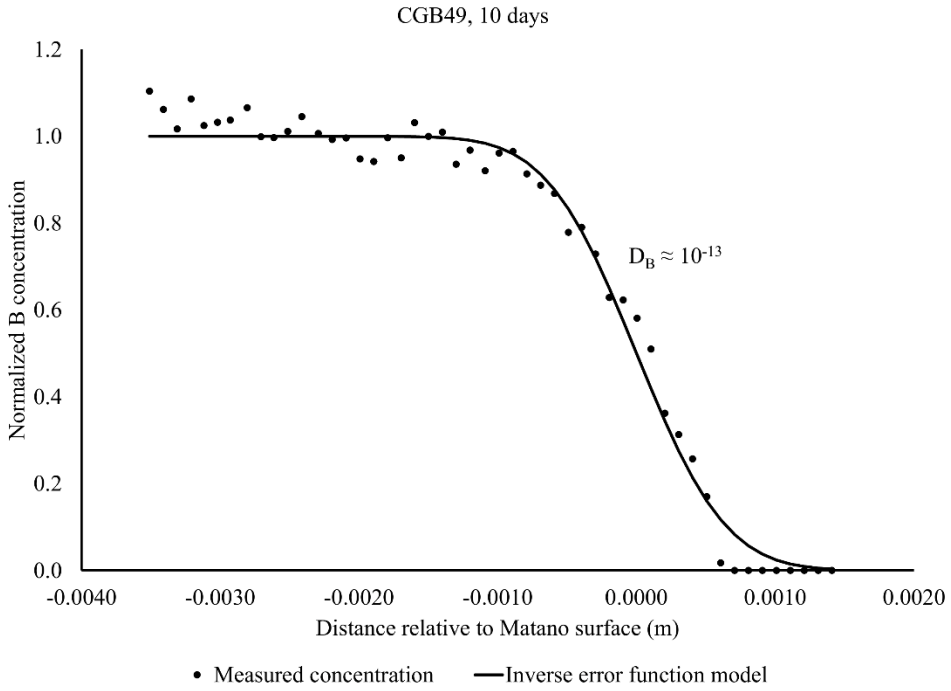

Figure 3-6 Concentration-distance profile representative of experiments that were designed to assess the chemical diffusivity of individual B isotopes. Shown in this diagram is data from experiment CGB49 which used a ^{11}B enriched glass as a source of B. Y-axis is normalized B content of glass, X-axis is distance (meters) relative to the Matano surface. Circles are EMPA data. Solid line represents a solution to the inverse error function using a diffusion coefficient of 10^{-13} m^2/s (Table 3).

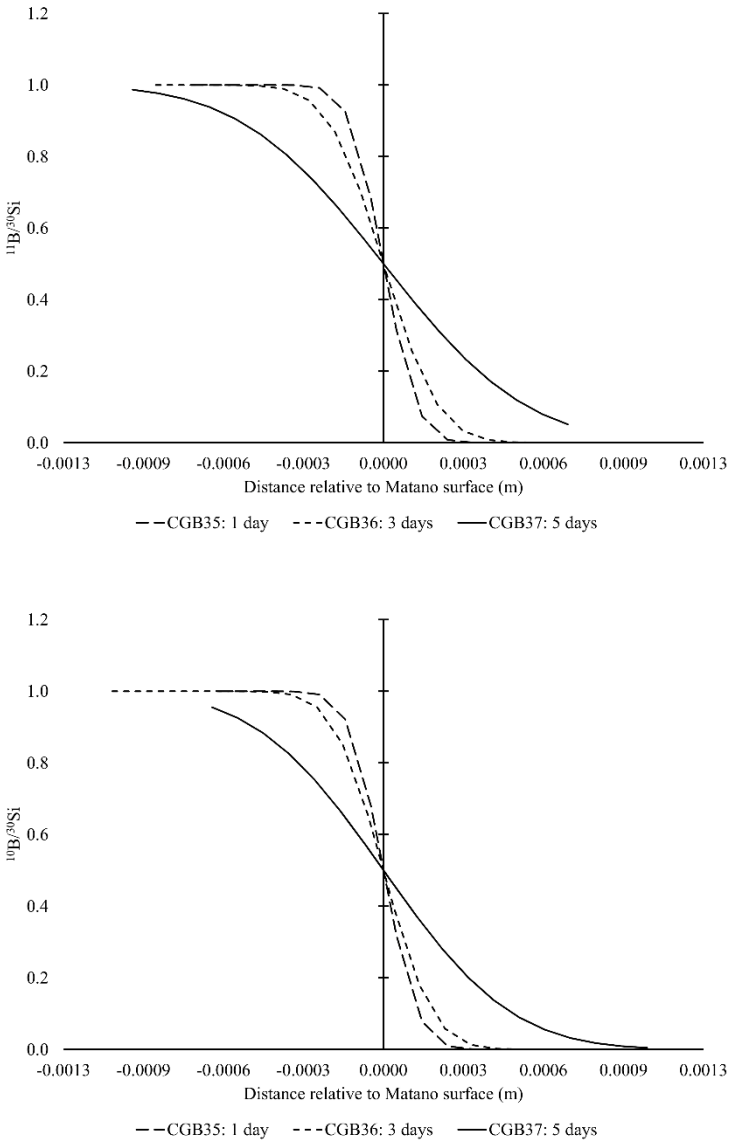

Figure 3-7 Time-series of hydrous experiments involving the inter-diffusion of ^{11}B (a) and ^{10}B (b). Y-axis is the normalized $^{11}B/^{30}Si$ (a) or $^{10}B/^{30}Si$ (b) ratios measured using SIMS. X-axis is distance, relative to the Matano surface, across the glass (in meters). Lines represent solutions to the inverse error function equation. Long, dashed line is for a 1-day experiments; short, dashed line is for a 3-day experiment; solid line is for a 5-day experiment.

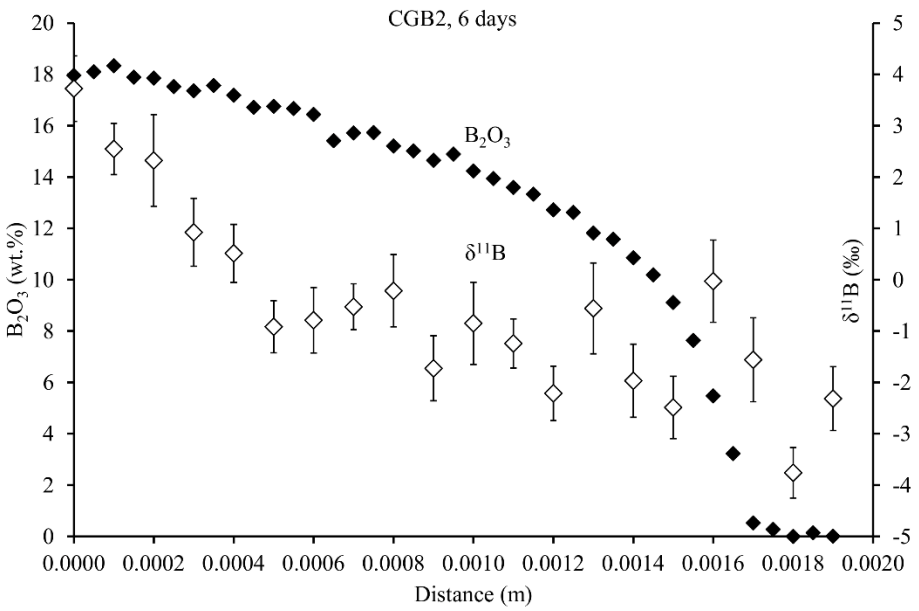

Figure 3-8 Boron and boron isotopic profile across glass in experiment CGB2. Y-axis on left-hand side is the concentration (wt.%) of B_2O_3 and, on the right-hand side, the boron isotopic composition. X-axis is distance (in meters) from the edge of the glass. The boron isotopic composition of the glass decreases by ~ 5‰ over ~ 500 μm, then plateaus across the remainder of the B diffusion profile.

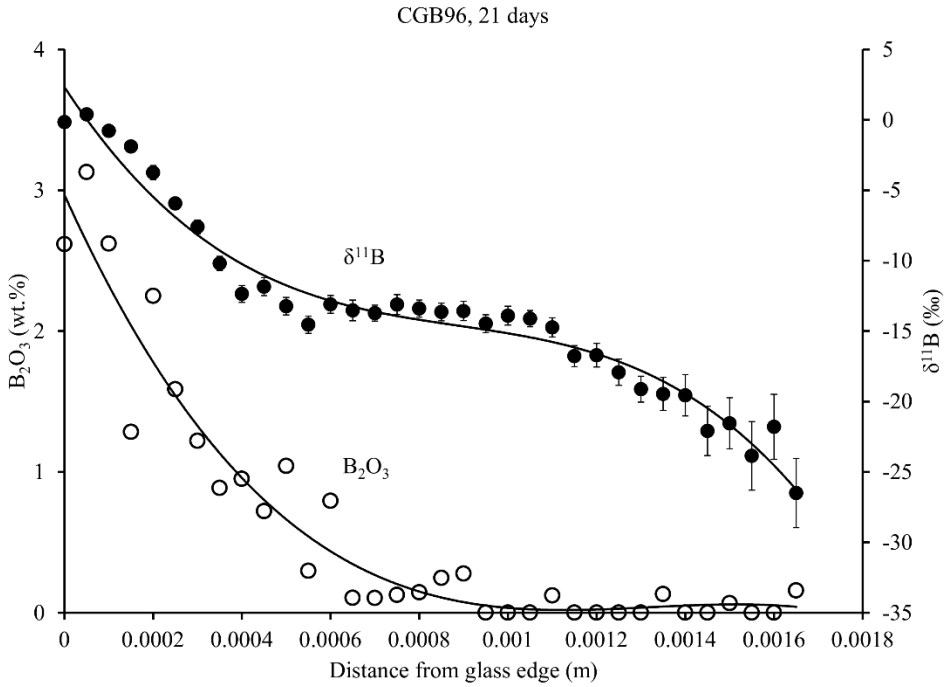

Figure 3-9 Boron and boron isotopic profile across glass in experiment CGB96. Y-axis on left-hand side is the concentration (wt.%) of B_2O_3 and, on the right-hand side, the boron isotopic composition. X-axis is distance (in meters) from the edge of the glass. The boron isotopic composition of the glass decreases by ~ 10‰ over the first ~ 500 μm, plateaus across the center of the experiment (at the contact of the starting material glasses), then decreases ~ 10‰ at the right-hand side of the diffusion profile.

Table 3-1 Compositions of starting material glasses

	CG	HG[1]	HG	HGB5[1]	HGB5[2]	[11]BHG	[10]BHG
SiO_2	77.68	73.43	78.01	68.37	73.20	69.98	70.17
B_2O_3	---	---	---	4.32	4.63	10.45	11.13
Al_2O_3	12.70	11.74	12.51	12.38	13.25	11.30	11.20
Na_2O	4.49	3.86	4.21	3.96	4.24	3.78	3.76
K_2O	4.85	4.52	4.87	4.37	4.68	4.22	4.22
Total	99.72	93.55	99.60	93.40	100.00	99.72	100.48
N	ICP	50	50	15		20	20

[1]Hydrous glass

[2]HGB5 calculated on an anhydrous basis

Table 3-2 Compositions of EMPA/SIMS glass standards

	Hydrous							Anhydrous		
	MAC	2.5EN	2.5FN	5AN	5CN	B5	E10	JM253	JM902	JM901F
SiO_2	72.32	70.67	70.31	68.22	67.89	70.12	63.63	65.50	66.30	56.30
B_2O_3	0.62	3.13	2.60	5.63	6.16	5.26	10.41	5.24	7.04	9.09
Al_2O_3	15.63	11.12	11.26	11.00	10.81	11.68	10.39	2.92	1.76	5.12
MgO	---	---	---	---	---	---	---	2.78	3.15	4.84
CaO	0.23	---	---	---	---	---	---	5.85	4.59	7.38
Na_2O	4.10	3.63	3.60	3.45	3.45	3.89	3.43	16.40	16.20	15.90
K_2O	3.53	4.36	4.38	4.19	4.21	4.31	3.83	0.60	0.51	1.17
Total	96.43	92.92	92.15	92.49	92.51	95.26	91.69	99.29	99.55	99.80
N		25	25	25	25	13	15			

N: Number of EMPA data points

MAC: Macusani obsidian, London et al. (1988)

Anhydrous glasses (JM) produced and characterized by the Johns Manville company

Table 3-3 Effective binary diffusion coefficients for boron

Exp#	Design	T (°C)	t (days)		BM (max)	BM (min)	r^2	erf	r^2	ln(D)-BM (max)	ln(D)-BM (min)	ln(D)-erf
CGB2	H_3BO_3 + CG	800	6	H	3.0E-12	1.3E-13	0.977	1.0E-13	0.942	-26.5	-29.7	-29.9
CGB91	HGB5 + HG	800	14	H	1.6E-13	3.0E-14	0.978	1.0E-14	0.996	-29.5	-31.1	-32.2
CGB92	HGB5 + HG	800	14	H	1.0E-13	2.0E-14	0.941	1.0E-13	0.989	-29.9	-31.5	-29.9
CGB96	HGB5 + HG	800	21	H	---	---	---	---	---	---	---	---
CGB48	^{10}BHG + HG	800	10	H	2.9E-12	3.3E-13	0.950	9.0E-13	0.965	-26.6	-28.7	-27.7
CGB49	^{11}BHG + HG	800	10	H	2.0E-12	3.0E-13	0.992	3.0E-13	0.994	-26.9	-28.8	-28.8

A: Anhydrous starting material glass; hydration during B diffusion

H: Pre-hydrated starting material glass or hydration during B diffusion

BM: Boron diffusion coefficient using Boltzman-Matano equation

erf: Boron diffusion coefficient using inverse error function

r^2: correlation coefficient for 3rd-order polynomial fit to concentration-distance profile (BM) and for linear regression comparing measured and calculated concentrations (erf)

---: insufficient data to calculate D

Table 3-4 Self diffusivities of boron isotopes

					^{11}B							
Exp#	T (°C)	t (days)	H_2O (wt.%)		BM (max)	BM (min)	r^2	erf	r^2	ln(D)-BM (max)	ln(D)-BM (min)	ln(D)-erf
CGB34	800	0	7.68	H	---	---	---	---	---	---	---	---
CGB35	800	1	5.55	H	3.3E-12	5.3E-13	0.999	1.3E-13	0.999	-26.4	-28.3	-29.7
CGB36	800	3	5.94	H	2.4E-12	2.6E-13	0.999	1.1E-13	0.995	-26.8	-29.0	-29.8
CGB75	800	3	0.00	A	2.7E-13	5.3E-14	0.996	1.3E-14	0.998	-28.9	-30.6	-32.0
CGB37	800	5	7.25	H	5.1E-12	4.6E-13	0.999	4.5E-13	0.996	-26.0	-28.4	-28.4

					^{10}B							
Exp#	T (°C)	t (days)	H_2O (wt.%)		BM (max)	BM (min)	r^2	erf	r^2	ln(D)-BM (max)	ln(D)-BM (min)	ln(D)-erf
CGB34	800	0	7.68	H	---	---	---	---	---	---	---	---
CGB35	800	1	5.55	H	3.3E-12	4.0E-13	0.999	1.3E-13	0.999	-26.4	-28.5	-29.7
CGB36	800	3	5.94	H	2.0E-12	2.2E-13	0.998	9.0E-14	0.999	-26.9	-29.1	-30.0
CGB75	800	3	0.00	A	3.1E-13	3.5E-14	0.997	1.4E-14	0.998	-28.8	-31.0	-31.9
CGB37	800	5	7.25	H	7.3E-12	2.4E-13	0.999	3.6E-13	0.999	-25.6	-29.1	-28.7

H_2O: calculated as the difference of EMPA totals from 100%

A: Anhydrous starting material glass; hydration during B diffusion

H: Pre-hydrated starting material glass or hydration during B diffusion

BM: Boron diffusion coefficient using Boltzman-Matano equation

erf: Boron diffusion coefficient using inverse error function

r^2: correlation coefficient for 3rd-order polynomial fit to concentration-distance profile (BM) and for linear regression comparing measured and calculated concentrations (erf)

---: insufficient data to calculate D

Chapter 4 Fractionation of the isotopes of boron between granitic melt and aqueous solution at 700°C and 800°C (200 MPa)

1. Introduction

Boron is a trace element in the continental crust, yet, its concentration is 10 to 100 times greater than in the mantle (Leeman and Sisson, 1996; Marschall et al., 2017). The enrichment of B in the crust is due to its incompatibility in most rock-forming minerals (Brenan et al., 1998; London, 2008; London et al., 1996; Marschall et al., 2017) and natural silicate liquids (Dingwell et al., 1996; Hervig et al., 2002; London et al., 1988). The boron isotopic composition, $\delta^{11}B$, of minerals and rocks from various crustal, mantle, and marine environments spans a range of ~ 90‰ (Xiao et al., 2013). The large range of $\delta^{11}B$ values has prompted many studies, all of which conclude that the large range of $\delta^{11}B$ values on Earth must result from (1) interaction of minerals with fluids (aqueous solution or melt) that have distinct isotopic compositions and (2) temperature-dependent isotopic fractionation between mineral and fluid (Hervig et al., 2002; Jiang et al., 2008; Marschall et al., 2017, 2009, 2006; Meyer et al., 2008; Palmer et al., 1992; Palmer and Swihart, 1996; Siegel et al., 2016; Tonarini et al., 1998, 2003; Trumbull et al., 2013; van Hinsberg and Marschall, 2007; Williams et al., 2001a, 2001b).

In the continental crust, the most abundant B-rich mineral is tourmaline (tur) (Grew, 1996; London et al., 1996); however, muscovite (ms), which is volumetrically more abundant than tourmaline, also constitutes a large reservoir of B (London et al., 1996). Therefore, most boron isotopic studies of crustal materials have focused on the

compositions of tourmaline and mica (Maner and London, 2017; Marschall et al., 2006; Siegel et al., 2016; Tonarini et al., 2003, 1998, Trumbull et al., 2013, 2009, 2008; Trumbull and Chaussidon, 1999; van Hinsberg and Marschall, 2007). The average $\delta^{11}B$ of the continental crust is ~ -10‰ (Kasemann et al., 2000; Leeman and Sisson, 1996; Marschall et al., 2017). The negative average, -10‰, is attributed to the loss of ^{11}B to water during devolatization of metamorphic rocks with increasing metamorphic grade (Kasemann et al., 2000; Romer and Meixner, 2014b) and to the exsolution of water from granitic melt (Hervig et al., 2002) during ascent and crystallization.

The $\delta^{11}B$ values of tourmaline from granites and pegmatites have been used to assess (1) the role of water in the crystallization of granites and pegmatites, (2) assimilation of various geologic materials into granitic melt, and (3) the source materials of granitic melts (Maner and London, 2017; Siegel et al., 2016; Smith and Yardley, 1996; Tonarini et al., 1998; Trumbull et al., 2013; Trumbull and Chaussidon, 1999; Yang et al., 2015). Three studies have focused on the $\delta^{11}B$ values of tourmaline from the massive and miarolitic portions of granitic pegmatites, in the hope of using these data to elucidate the point at which an aqueous solution exsolved from, and coexisted with, an H_2O-saturated granitic melt (Maner and London, 2017; Tonarini et al., 1998; Trumbull et al., 2013). For this purpose, it is necessary to know the equilibrium distribution of ^{10}B and ^{11}B between hydrous granitic melt and coexisting aqueous solution at granite- and pegmatite-forming temperatures. Kinetic fractionation related to diffusion may also play a role (e.g., Maner and London, submitted), but the first step to assessment entails a firm knowledge of equilibrium values of $\Delta^{11}B_{melt\text{-}aq.sln}$. That is the goal and purpose of this study.

1.1. Boron isotopic fractionation in the system tourmaline-granitic melt-aqueous fluid

Boron isotopic fractionation between tourmaline and aqueous solution has been experimentally measured (Meyer et al., 2008; Palmer et al., 1992) and calculated using *ab initio* first-principles methods (Kowalski et al., 2013). The results of each study reveal that tourmaline crystallizing from an aqueous solution will be isotopically lighter than the aqueous solution. In a closed system, the isotopic composition of the aqueous fluid and of tourmaline will evolve toward heavier compositions with progressive growth of tourmaline. Fractionation factors for 'rhyolite' melt-aqueous fluid have been experimentally measured (Hervig et al., 2002), and these results (two experiments utilizing the Macusani obsidian as representative of rhyolitic melts) predict that an aqueous fluid that exsolves from melt will be isotopically heavier than the melt. The accuracy of these values has been questioned based on the $\delta^{11}B$ of tourmaline in, presumably, water-saturated pegmatites (Maner and London, 2017; Siegel et al., 2016; Trumbull et al., 2013). Isotopic fractionation factors for tourmaline-melt have not been measured experimentally. Some studies (Maner and London, 2017; Siegel et al., 2016; Trumbull et al., 2013, 2008) calculated a fractionation factor for tourmaline-melt using the datasets of Hervig et al. (2002), Meyer et al. (2008), and Palmer et al. (1992). Differences in values of $\Delta^{11}B$ for different mineral-fluid pairs at a given temperature and pressure are controlled by the change in coordination of B in each phase (cf. Meyer et al., 2008; Wunder et al., 2005). The maximum amount of isotopic fractionation between two phases is expected when the coordination of B in one phase is different than the coordination of B in the other phase.

1.2. The coordination of B in melt and aqueous solution

Boron adopts two different coordination polyhedra when bonded with oxygen: 3-fold trigonal planar, ^{III}B, and 4-fold tetrahedral, ^{IV}B (Dingwell et al., 1996; Palmer and Swihart, 1996). The ^{III}B-O bond is shorter than the ^{IV}B-O bond (Hawthorne et al., 1996), resulting in a preference of ^{10}B in the longer ^{IV}B-O bond (Palmer and Swihart, 1996). In aqueous solution at room temperature, the majority of B adopts 4-fold coordination when pH is > 10 and 3-fold when pH is < 6 (Kakihana et al., 1977). Polyborate rings comprising ^{III}B-^{III}B, ^{IV}B-^{IV}B, and ^{III}B-^{IV}B linkages form in solution when the concentration of B is greater than 0.5 mol/L B (Kakihana et al., 1977; Maya, 1976). Schmidt et al. (2005) reported that increasing temperature results in the disappearance of polyborate rings and the formation of orthoborate ^{III}B species. In acidic solutions, the amount of ^{IV}B increases with temperature (Schmidt et al., 2005). The dominant coordination of B in aqueous solution at magmatic temperatures, i.e. ≥ 500°C, is as ^{III}B (Schmidt et al., 2005). Therefore, the fractionation of ^{11}B and ^{10}B between their III- and IV-fold coordination polyhedra, respectively, which is the principal determinant in their fractionation, should be nil at magmatic temperatures.

1.2.1. Boron in anhydrous glasses

In silicate melt, boron can form large clusters of polyborate rings comprised of ^{III}B-^{III}B, ^{IV}B-^{IV}B, or ^{III}B-^{IV}B polyanionic domains (Morgan et al., 1990) in addition to the orthoborate ^{III}B and ^{IV}B geometries mentioned above (Geisinger et al., 1988). Spectroscopic data of anhydrous sodium and calcium aluminosilicate compositions shows that the fraction of ^{III}B increases with increasing temperature, field strength of the modifier cation (Ca^{2+} > Na^{+}), B content, and aluminosity of melt (Wu et al., 2011;

Wu and Stebbins, 2013, 2010, 2009). Geisinger et al. (1988) measured the coordination of B in melt along the dry albite (Ab: $NaAlSi_3O_8$)-reedmergnerite (Rd: $NaBSi_3O_8$) join and found that the amount of ^{III}B decreases from ~ 60% at $Ab_{80}Rd_{20}$ to ~ 25%Rd_{100}.

1.2.2. Boron in hydrous glasses

Schmidt et al. (2004) observed that the fraction of ^{III}B in anhydrous and hydrous (~ 4 wt% H_2O) albite glasses with B contents of 4.8, 9.1, and 16.7 wt% B_2O_3 is ~ 0.94. Increasing B_2O_3 and H_2O led to a slight (< 2 %) increase in the fraction of ^{IV}B. Schmidt et al. (2004) conclude by suggesting that B forms trigonal units that strongly interact with the aluminosilicate framework, forming Al-O-B and Si-O-B bonds. Morgan et al. (1990) found that a large fraction of B forms insular clusters with ^{11}B in 3-fold coordination in a hydrous metaluminous (A/CNK = 1) sodium aluminosilicate glass containing 4 wt% H_2O and 15 wt% B_2O_3 derived from standard reagent boric acid. They observed a negligible component of ^{11}B in 4-fold coordination; however, we would expect TO_4 units to be populated mostly by ^{10}B. Borate domains exhibited little interaction with the aluminosilicate framework components of the glass, except to scavenge Na and H (as OH) to the borate domains and thereby create a component of ^{VI}Al in the glass. In summary, based on what is known or inferred about the coordination of B in hydrous granitic melt, most B is expected to be in 3-fold coordination.

The available data indicate that ^{III}B should predominate in hydrous granitic or pegmatite-forming melts and in aqueous solutions in equilibrium with those melts. If that is the case, then we would anticipate only slight fractionation of boron's isotopes between melt and aqueous solution at magmatic temperatures as a function of their

difference in mass, but not influenced by the extent of ^{III}B-^{IV}B coordination in either fluid. This prediction is at odds with the large and negative fractionation factor for $\Delta^{11}B_{melt\text{-}aq.sln.}$ reported by Hervig et al. (2002), which they attribute to a large fraction of ^{IV}B in the melt.

1.3. Goal of the present study

Disparities between the predicted and measured values of $\Delta^{11}B_{melt\text{-}aq.sln.}$, and the limited data (two experiments) of Hervig et al. (2002) prompted the present study. The goal of this investigation is to quantify the isotopic fractionation factors for boron between granitic melt and aqueous solution at 700°C and 800°C, 200 MPa_{H2O}. Fractionation factors are presented for two hydrous, B-bearing, metaluminous granitic compositions and for the Macusani obsidian (London et al., 1988). The results are compared with the melt-aqueous solution data reported by Hervig et al. (2002). Based on the results of this study, we include a preliminary assessment of the coordination of B in hydrous granitic melt based on the $\Delta^{11}B$ data. Lastly, we discuss implications of the data on the isotopic composition of aqueous fluids exsolving from granitic melt and the isotopic composition of tourmaline in granites and pegmatites.

2. Methods

2.1. Preparation of starting materials

Glass HG (Table 4-1) was prepared to match the thermal minimum in the hydrous, metaluminous haplogranite system at 200 MPa_{H2O}. The glass was fused from mixed powdered chemical reagents in Pt dishes in a Deltech bottom-loading furnace at 1600°C for 1 to 4 hours. Chips of this glass were analyzed by an electron microprobe for their chemical composition and to assess chemical homogeneity. Upon creating a

homogeneous glass, it was crushed and milled to a fine powder. Boron, as NIST SRM 951a boric acid (Catanzaro et al., 1970), was added to two aliquots of the powdered glass to bring the concentration of B_2O_3 to 2.5 wt% and 5 wt% B_2O_3, respectively.

Mixtures of powdered glass plus boric acid were loaded into 5 different gold capsules with enough H_2O to bring the concentration of H_2O in the resultant glass to ~ 7 wt% H_2O. This produced 5 glasses containing 2.5 wt% B_2O_3 and 5 glasses containing 5 wt% B_2O_3. Sealed capsules were pressurized at room temperature and then heated to 800°C at 200 MPa for 30 days. After 30 days, the vessels were quenched to room temperature (section 2.2) at which point the capsules were removed from the vessel. Each capsule was reweighed to check for leaks that might have occurred while at P and T in the pressure vessels. Capsules showing no signs of leaks were prepared for chemical and isotopic analysis and experimentation (section 2.3). Some hydrous, B-bearing glasses were sectioned into ~ 1 mm thick wafers using a low-speed saw with a diamond-embedded blade. These wafers were used in experiments designed to measure B isotopic fractionation and elemental partitioning. One capsule from the 2.5 wt% (2.5CN: Table 4-1) and 5 wt% (5DN: Table 4-1) glass series was sectioned such that only one 1 mm thick wafer was cut from the end of the capsule; the remainder of each glass was sent to ALS Scandinavia (Luleå, Sweden) for boron isotopic analyses. The boron isotopic compositions of all other synthetic starting material glasses (Table 4-1) were measured by SIMS (section 2.5) using the two glasses sent to ALS Scandinavia as boron isotope standards. The concentration of B in each starting material glass was measured by EMPA and SIMS.

The Macusani obsidian, hereafter referred to as MAC (Table 4-1), was used in series of experiments to re-assess the fractionation factors measured by Hervig et al. (2002). A 0.5 cm thick section was cut from one pebble of MAC. Cores measuring ~ 3 x 4 mm were taken from the 0.5 cm thick section of MAC. One core was sent to ALS Scandinavia for boron isotopic analysis. Wafers ~ 1 mm thick were sectioned from several MAC cores to be used in experiments.

2.2. Experimental methods

Loaded gold capsules containing borosilicate glass plus deionized ultra-filtered water were weighed before and after welding with a TIG-welder. Capsules that did not lose weight during welding or in a drying oven at ~ 125°C for ≥ 4 hrs were loaded into NIMONIC 105 cold-seal reaction vessels. Most experiments were heated to either 700°C or 800°C and 200 MPa for 30 days. One experiment using MAC was heated to 750°C for 90 days at 200 MPa. Two experiments were heated to 750°C and 850°C, 200 MPa, for 1 and 2 days, respectively, to compare to the experimental results of Hervig et al. (2002).

All experiments were quenched nearly isobarically at an average rate of ~30°C/min to room temperature. All capsules were weighed again after quench to check for leaks produced during the experiment. Capsules showing no signs of leakage were punctured to allow water to evaporate. Punctured capsules were placed in an ultrasonic bath filled by deionized and distilled water to dissolve any soluble borates that may have crystallized during quench and evaporation. The mass of the final, equilibrated glass was recorded and the mass of the aqueous solution was calculated using mass-balance (section 3). Glasses were then prepared for chemical and/or isotopic analyses.

2.3. Preparation of glasses for analysis

Five to six pieces of glass from experiments and starting material glasses were embedded in a 1" circular mold using EpoThin™ (Beuhler) epoxy. Molds were initially ground using diamond-embedded plates on a lapidary wheel followed by a polish using a combination of diamond-embedded films. A final, fine-finish polish was applied to each sample using a series of solutions containing 3 µm to ¼ µm diamond grit. Polished mounts were cleaned, dried, and coated with either C (for EMPA) or Au (for SIMS) prior to analysis.

2.4. Electron microprobe (EMPA)

The Cameca SX-100 at the University of Oklahoma (OU) was used to chemically characterize all glasses. Glasses were analyzed for Si, Al, K, Na, and B using a 2-condition analytical routine. The first condition used a 10 kV accelerating voltage, 2 nA beam current, and 20 µm spot diameter to analyze Si, Al, K, and Na. The second condition used the same accelerating voltage and spot size, but a 40 nA beam current to analyze B. Individual point analyses were dispersed evenly across each glass forming a linear transect from one edge of the glass to the other. Counting times were chosen to yield the best possible detection limits while obviating beam damage to the sample and the need for a time-dependent intensity correction. Detection limits for SiO_2, Al_2O_3, Na_2O, and K_2O of ~ 0.1 wt.% and ~ 0.5 wt.% for B_2O_3. Data reduction used the PAP method (Pouchou and Pichoir, 1985). Chemical compositions of starting material glasses are reported in Table 4-1.

2.5. Secondary ion mass spectrometry (SIMS)

Boron concentrations and isotopic ratios were measured using the Cameca 6f secondary ion mass spectrometer (SIMS) at the Arizona State University. Individual point analyses were measured as transects from a location as close to the edge of the glass as reasonably possible toward the center of the glass. Measurement of B and $\delta^{11}B$ used an instrument setup similar to that reported by Maner and London (2017). The total impact energy was 21.5 kV with a primary ion beam current between 1 and 5 nA for all analyses. Boron content was calculated using a calibration reported by Maner and London (submitted). For measurement of B, the SIMS instrument was setup to measure ^{11}B, ^{10}B, and ^{30}Si for 1s each using an energy window offset of -75 V and a window of ± 20 V.

Boron isotopic ratios were measured by counting ^{11}B for 8 seconds and ^{10}B for 2 seconds, using a mass resolving power (MRP) ≥ 1400. An energy window offset was not applied and the width of the window was ± 20 V. Count rates for the abundant isotope, ^{11}B, were kept at or below 300 kcps to obviate dead time issues on the photoelectron multiplier. Standard errors (2σ) are less than 1 ‰ for individual spots (internal errors) and less than 2 ‰ based on spot-to-spot reproducibility on standards (external errors). All boron isotopic ratios are reported using standard units (‰) and isotopic notation and the zero point reference of Catanzaro et al. (1970). Boron isotopic compositions of the starting material glasses are reported in Table 4-1.

3. Mass-balance calculation of isotopic fractionation factors and partition coefficients

Partition coefficients for B, $D_B^{M/V}$, between melt (M) and aqueous solution (V) were calculated using mass-balance equations and B content measured by SIMS. The masses of the starting glass, initial H_2O, final glass, and final H_2O are presented in Table 4-2. The mass of B in the starting glass was calculated by dividing the measured concentration of B_2O_3 (in wt%) by 100 and then multiplying that figure by the mass of the starting glass. The B_2O_3 content of the final glass was calculated in the same way as the starting glass. The difference, by mass, of B_2O_3 in the starting and final glasses is the B_2O_3 content of the aqueous solution at run conditions. The concentration of B_2O_3 in the aqueous solution was calculated by dividing the mass of B_2O_3 by the mass of the aqueous solution and multiplying by 100, to arrive at units of wt%. Partition coefficients for B, as B_2O_3, between melt and aqueous solution were calculated by dividing the concentration of B_2O_3 in the aqueous solution by the B_2O_3 in glass (Equation 1).

$$(1)\ D_B^{V/M} = \frac{B_2O_{3(V)}}{B_2O_{3(M)}}$$

Boron isotopic fractionation factors were calculated in much the same way as the partition coefficients, with one exception. The B isotope ratio of the starting and final glasses was used to calculate the B isotope ratio of the final aqueous solution (Table 4-2). The mass of B was converted into moles of B. The moles of total B were converted into moles of ^{11}B and moles of ^{10}B using the B isotope ratio measured by SIMS. The moles of ^{11}B and ^{10}B in the aqueous solution were calculated by taking the

difference between the moles of ^{11}B and ^{10}B of the starting and final glasses. Boron isotopic fractionation factors are reported in two ways: in alpha, α (Equation 2), and delta, Δ (Equation 4), notation. The B isotope ratio of the aqueous solution (V) was divided by the B isotope ratio of the final glass (M) for α notation.

$$(2)\ \propto = \frac{\left({}^{11}\mathrm{B}/{}_{10}\mathrm{B}\right)_V}{\left({}^{11}\mathrm{B}/{}_{10}\mathrm{B}\right)_M}$$

For Δ notation, the calculated B isotope ratio of the aqueous solution (V) was converted into delta, δ (Equation 3), notation and subtracted from the B isotopic composition, in δ units, of the final glass (M).

$$(3)\ \delta^{11}\mathrm{B} = \left(\left(\frac{\frac{^{11}\mathrm{B}}{^{10}\mathrm{B}}_{M\ or\ V}}{\frac{^{11}\mathrm{B}}{^{10}\mathrm{B}}_{NIST\ SRM\ 91a}}\right) - 1\right) * 1000$$

$$(4)\ \Delta^{11}\mathrm{B} = \delta^{11}\mathrm{B}_M - \delta^{11}\mathrm{B}_V$$

4. Results and Discussion

4.1. Approach to equilibrium

The experiments reported in this manuscript were designed to transfer B from melt into aqueous solution. The duration of experiments was chosen by calculating the time required to diffuse B one millimeter through hydrous, granitic melt at 800°C and 200 MPa using the diffusion data of London (2009); that value of the diffusion

coefficient, $D_B = 10^{-13}$ m^2/s, has been confirmed in a more comprehensive series by Maner and London (submitted).

Experiments CGB86 and CGB87, using MAC obsidian, were conducted for 24 and 48 hrs at 750°C and 850°C, respectively. Boron isotopic measurements across each glass reveal no fractionation of the starting isotopic signature of the obsidian. However, the B content of the glass is strongly depleted within a ~ 10 μm domain toward the glass-vapor interface. Therefore, the results from experiments CGB86 and CGB87 do not represent equilibrium distributions of B or its isotopes between melt and aqueous solution.

Experiments using the synthetic granitic glass were held at 700°C and 800°C for 30 days. The compositions of these experiments have small analytical errors (Table 4-3), which indicates that the glasses (melts) equilibrated with the aqueous fluid. Moreover, the boron isotopic ratios of glass, measured from edge-to-center of each glass, lie within the 2‰ external error (section 2.5). The B content and B isotopic ratio of the glass from experiment CGB88, which was conducted at 750°C for 90 days using MAC glass, is homogeneous from edge-to-core. Based on the homogeneous nature of B and its isotopes across all glass products in experiments held at temperature for at least 30 days, we conclude that the isotopic fractionation factors and partition coefficients reported in this study represent near-equilibrium values.

4.2. Chemical compositions of glass products and partitioning of B between melt and aqueous solution

4.2.1. Comparison of B_2O_3 by SIMS and EMPA

The chemical compositions of glass products are reported in Table 4-3. A comparison of B content measured by EMPA and SIMS is shown in Figure 4-1. Boron measured using EMPA is ~ 10% higher relative to the B_2O_3 measured using SIMS. The relative difference between B_2O_3 measured by EMPA and SIMS is greatest at low concentrations where background measurements by EMPA become problematic, i.e. greater relative standard deviations near the detection limit. Though the relative difference between B_2O_3 measured by EMPA and SIMS improves with increasing B_2O_3 in the glass, the error associated with measuring B at low concentrations is much better for SIMS than EMPA. Therefore, the B_2O_3 content of glass determined by SIMS is used to calculate the B_2O_3 of the aqueous solution, melt-fluid partition coefficients, and melt-fluid isotopic fractionation factors.

4.2.2. Analyses of SiO_2, Al_2O_3, Na_2O, K_2O

The difference between the starting and final glass compositions, excluding B, for the series of experiments that used the synthetic granitic composition is zero. Therefore, the metaluminous granitic melt seems to dissolve congruently into aqueous solution, regardless of the amount of B in melt or aqueous solution. On the contrary, data for the Macusani obsidian from the current study shows that Na_2O is removed from melt to the aqueous solution (~ 5% relative) and that the concentration of K_2O in the residual melt increases ~ 5% relative. Silica appears to dissolve congruently into the aqueous solution, and Al_2O_3 is enriched in the residual melt by ~ 2.4 %. The

experimental study of London et al. (1988), using the Macusani obsidian, reported congruent dissolution of melt into aqueous fluid. Small (< 1.5%) relative standard deviations associated with the calculation of Na_2O and K_2O between the starting and final glasses is evidence that the observed differences are real. The difference in SiO_2 and Al_2O_3 between the starting and final glasses is negligible. Based on these observations, it appears that the solubility of granitic melt in aqueous solution is not perfectly congruent for complex granitic liquids such as the Macusani obsidian.

4.2.3. Analyses of B_2O_3 and H_2O

There is a negative correlation between B_2O_3 and H_2O in melt, and their concentrations are not sensitive to changes in temperature (Table 4-3). In the experimental study of Holtz et al. (1993), the authors found that the solubility of water, which was measured using Karl Fischer titration (KFT), increases with increasing B_2O_3. Similarly, London (2009) conducted B diffusion experiments in which water, which was calculated as the difference of EMPA totals from 100%, was found to increase with increasing B content along a diffusion profile. The concentration of H_2O in glass reported in this manuscript are within ~ 10% relative to those measured by Holtz et al. (1993), which is within the relative error associated with calculating H_2O as the difference of EMPA totals from 100% (Morgan and London, 2005; Morgan and London, 1996). The errors associated with SIMS analyses of B in glass are small (< 1% relative). Therefore, the negative correlation between B_2O_3 and H_2O in glass appears to be real.

4.2.4. Concentrations of B_2O_3 in melt and aqueous solution

The concentration of B_2O_3 in each glass from the series of experiments using the synthetic granite is depleted ~ 50% relative to the starting glass composition. The partition coefficient for B_2O_3 between melt and aqueous solution is ~ 1.3 and ~ 1 for the glasses with an initial 5 wt% and 2.5 wt% B_2O_3, respectively (Table 4-4 and Figure 4-2). Partition coefficients are not temperature-dependent and agree with an earlier estimate provided by Hervig et al. (2002). London et al. (1988), however, observed a temperature-dependency on the partition coefficient for B between 675°C and 750°C.

4.3. Isotopic fractionation factors

The boron isotopic compositions of melt (glass) and aqueous solution, and the isotopic fractionation factors between these two phases, are found in Table 4-4. Figure 4-3 shows the $\Delta^{11}B$ values for melt-aqueous solution measured in this study as a function of temperature, and compares the present data to the 'III-IV' fractionation trend (Hervig et al., 2002; Wunder et al., 2005). Figure 4-4 shows the $\Delta^{11}B$ values for melt-aqueous solution reported in this study in addition to $\Delta^{11}B$ values for tourmaline-aqueous solution (Meyer et al., 2008; Palmer et al., 1992), melt-aqueous solution (Hervig et al., 2002), boromuscovite-aqueous solution (Wunder et al., 2005), and illite-aqueous solution (Williams et al., 2001a).

The $\Delta^{11}B$ value from experiment CGB88 (Figure 4-4), using MAC glass, is identical to the value reported by Hervig et al. (2002). Moreover, the values of $\Delta^{11}B$ for the synthetic granitic glasses tend to cluster around the $\Delta^{11}B$ measured using MAC glass. The experiments labeled 'Low B' and 'High B' used the synthetic granitic glasses with 2.5 wt% and 5 wt% B_2O_3, respectively. There is a slight, ~ 3‰, difference between

the $\Delta^{11}B$ values measured in this study for the 'High B' melt composition. It is possible that the larger, more negative, values of $\Delta^{11}B$ in the 'High B' experiments are a result of a higher proportion of ^{IV}B in melt compared to experiments using the 'Low B' melt composition. Values of $\Delta^{11}B_{melt\text{-}aq.sln.}$ measured in the 'Low B' experiments do not correlate with temperature, whereas, those measured from 'High B' experiments increase with increasing temperature. Because isotopic fractionation is expected to increase with decreasing temperature, we suspect that the coordination of B in the melt compositions in this study has a substantial effect on the $\Delta^{11}B$ between melt and aqueous solution.

Also shown in Figure 4-4 is a boron isotopic fractionation factor for melt-aqueous solution from experiment MAC230 (London and Morgan, 2017). In that experiment, a core of the Macusani obsidian was hydrated to 5.4 wt.% H_2O, then partially crystallized at 500°C, 200 MPa, for 1512 hrs. The resultant core contained 7 volume % of void space as miarolitic cavities in crystalline and glassy domains, together with 12.7 % of glass and 80.2% crystals. Crystals that terminate into miarolitic cavities are euhedral. Therefore, the aqueous solution exsolved from the melt in response to crystallization over the course of the experiment; that solution is not a sudden result of quenching. The isotopic composition of glass in experiment MAC230 was compared to an unreacted piece of MAC glass, both of which have the same composition. Therefore, at 500°C, $\Delta^{11}B_{melt\text{-}aq.sln.}$ appears to be zero, at least for the compositionally complex MAC glass at this condition.

4.4. Assessment of B coordination in hydrous, granitic melt based on $\Delta^{11}B_{melt\text{-}aq.sln.}$ data

With one exception, the fractionation factors reported in this study are significantly non-zero, are substantially larger than fractionation factors for tourmaline-aqueous solution at comparable pressure and temperature, and lie near the 'III-IV' fractionation trend (Figures 4-3 and 4-4). The negative signature of $\Delta^{11}B_{melt\text{-}aq.sln.}$ leads us to suggest, as did Hervig et al. (2002), that a significant proportion of B in hydrous granitic melt must be in 4-fold coordination. Spectroscopic studies of these glasses would be the logical next step to quantifying the coordination number of boron oxyanions in hydrous, granitic melt.

We have explained our reasoning that the high-temperature results of this study are consistent with an equilibrium distribution of boron's isotopes between granitic melt and aqueous solution. That is not the case for experiment MAC230, which was undercooled 245°C prior to the onset of crystallization, and may never have reached a final equilibrium among crystals, melt, and exsolved aqueous fluid. Though the apparent lack of isotopic fractionation of boron between the melt and aqueous solution could be related to the evolved composition of the resultant melt (e.g., 3.55 wt.% B_2O_3: see Electronic Appendix 4 of London and Morgan, 2017), low diffusivity of boron at these conditions might also account for the disparity with our high-temperature data. The diffusion coefficient for B in hydrous granitic liquid at 800°C, 200 MPa, is $D_B = 10^{-13}$ m^2/s (London, 2009; Maner and London, submitted), which is approximately that same diffusivity as Al (e.g., Acosta-Vigil et al., 2002). As low as this diffusivity is, it would be orders of magnitude lower at the temperature of MAC230. London and Morgan (2017) cited textural evidence that the melts produced from the hydrous

Macusani obsidian at these conditions were sufficiently viscous as to sustain brittle fracture. To the extent that the residual melt and aqueous solution in MAC230 approached a chemical equilibrium, we suggest that this was achieved principally by the dissolution of the bulk melt into the aqueous vapor, such that partition coefficients for elements and isotopes remained essentially at unity. This is analogous to the conclusions reached by Bea (1996) for the partitioning of trace elements between minerals and partial melts.

4.5. Applications to geologic systems

4.5.1. Degassing of granitic melt and crystallization of tourmaline from granitic melt and aqueous solution

The results of this study show significant fractionation of boron's isotopes between granitic melt and aqueous fluid at liquidus temperatures. At isotopic equilibrium, an aqueous fluid will be enriched in ^{11}B relative to coexisting granitic melt. The $\delta^{11}B$ of tourmaline that crystallizes from the aqueous solution should be markedly heavier than tourmaline that crystallizes from the melt, if tourmaline crystallization proceeds simultaneously from both fluids. The difference in the $\delta^{11}B$ of tourmaline crystallizing in melt and aqueous fluid at high temperature (> 700°C) should be small due to the convergence of fractionation factors for tourmaline-aqueous solution and granitic melt-aqueous solution. However, at ~450°C, the temperature at which pegmatites crystallize (London, 2008; London et al., 2012; Morgan and London, 1999; Siegel et al., 2016), the populations of $\delta^{11}B$ values for tourmaline that crystallize within miarolitic cavities, which presumably represent products of crystallization from an aqueous solution (Simmons et al., 2012), and tourmaline that crystallize in the massive

intermediate zones of pegmatites, which represent products of crystallization from melt (London, 2008), should be resolvable using modern methods of boron isotopic measurements (e.g. SIMS).

The only $\delta^{11}B$ values reported for tourmaline in which the $\delta^{11}B$ increases from coarse pegmatite into miarolitic cavity are for pegmatites that also contain minerals whose B is in 4-fold coordination (De Vito et al., 2002; Dini et al., 2002). Crystallization of minerals containing B in 4-fold coordination will increase the $\delta^{11}B$ of the fluid from which they grew (Wunder et al., 2005). Maner and London (2017) and Tonarini et al. (1998) found little variation in the $\delta^{11}B$ of tourmaline from the wall zone (near the outer margins of the pegmatites) through massive pegmatite interior zones into miarolitic cavities; these pegmatites do not contain a significant amount of B-bearing mineral other than tourmaline. Tonarini et al. (1998) suggested that the nearly identical values $\delta^{11}B$ of tourmaline from intermediate zone and miarolitic cavity result from either: (1) no fractionation of boron's isotopes between granitic melt and aqueous solution at equilibrium, or (2) a delicate balance between dwindling thermal energy and isotopic fractionation between tourmaline-melt-aqueous solution. In contrast, Maner and London (2017) concluded that an equilibrium distribution of boron's isotopes between tourmaline and granitic melt could not be achieved due to the rapid rate of crystallization of thin pegmatite dikes and the slow diffusivity of B in hydrous granitic melt at pegmatite-forming temperatures of 450°-500°C. On that basis, Maner and London (2017) suggested that the $\delta^{11}B$ of tourmaline in pegmatites represents the $\delta^{11}B$ of the bulk melt.

The apparent paradox presented by $\Delta^{11}B_{melt\text{-}aq.soln.}$ for MAC230 may resolve this ambiguity. From this study, $\Delta^{11}B_{melt\text{-}aq.soln.}$ should be ~ -11 to -10 ‰ if isotopic equilibrium is attained between melt and aqueous solution at 450°-500°C. Therefore, hypothesis 1 above (Tonarini et al., 1998) is incorrect. The lack of isotopic fractionation in MAC230 is consistent with the conclusion that the diffusivity of B and its isotopes through melt at pegmatite-forming temperatures is so slow that tourmaline that grows from melt or vapor will have isotopic compositions close to that of the bulk melt (Maner and London, 2017).

5. Conclusions

The boron isotopic fractionation factors reported in this study confirm that significant boron isotopic fractionation occurs between granitic melt and aqueous solution at liquidus temperatures, and that the aqueous solution becomes isotopically heavy relative to the granitic melt (Hervig et al., 2002). Like Hervig et al. (2002), we suggest that this isotopic fractionation reflects a substantial proportion of B in hydrous granitic melt that is in 4-fold coordination. Furthermore, this conclusion rests upon the fractionation of the isotopes of boron between III- and IV-coordinate polyhedra that has been demonstrated only in relatively low-temperature aqueous solutions (Sanchez-Valle et al., 2005). The data plot along a line through previous data for the systems melt-aqueous solution (Hervig et al., 2002), boromuscovite-aqueous solution (Wunder et al., 2005), and illite-aqueous solution (Williams et al., 2001a), and are larger than reported values for fractionation in the system tourmaline-aqueous solution (Meyer et al., 2008; Palmer et al., 1992).

The large fractionation factors observed in these high-temperature experiments lead us to conclude that the boron isotopic composition of tourmaline that crystallizes from granitic melt at pegmatite-forming temperatures should be markedly different from that of tourmaline crystallized from a coexisting aqueous solution. The absence of isotopic fractionation that has been documented in miarolitic pegmatites most likely reflects a lack of chemical and isotopic equilibration between melt and aqueous solution.

Figure 1

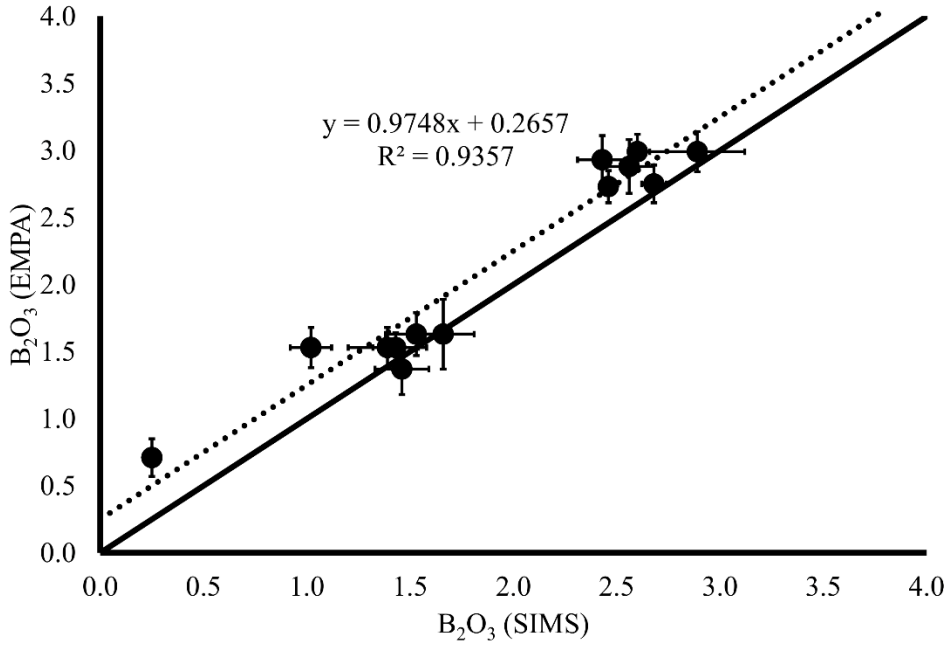

Figure 4-1 Comparison of B_2O_3 (wt%) measured by EMPA and SIMS. The solid black line represents a 1:1 correlation. Solid black circles represent average compositions of 13 glasses. Error bars are the propagated 2σ standard error of ~ 5 SIMS and 15-30 EMPA data points per glass sample. The dotted black line is a linear regression through the EMPA and SIMS data. At low concentration, < 1 wt% B_2O_3, the relative difference between the EMPA and SIMS data approaches 50%; whereas, at higher concentrations, the relative difference is < 10%. The SIMS measurement of B_2O_3 were used throughout this study to calculate partition coefficient and isotopic fractionation factors between melt and aqueous solution.

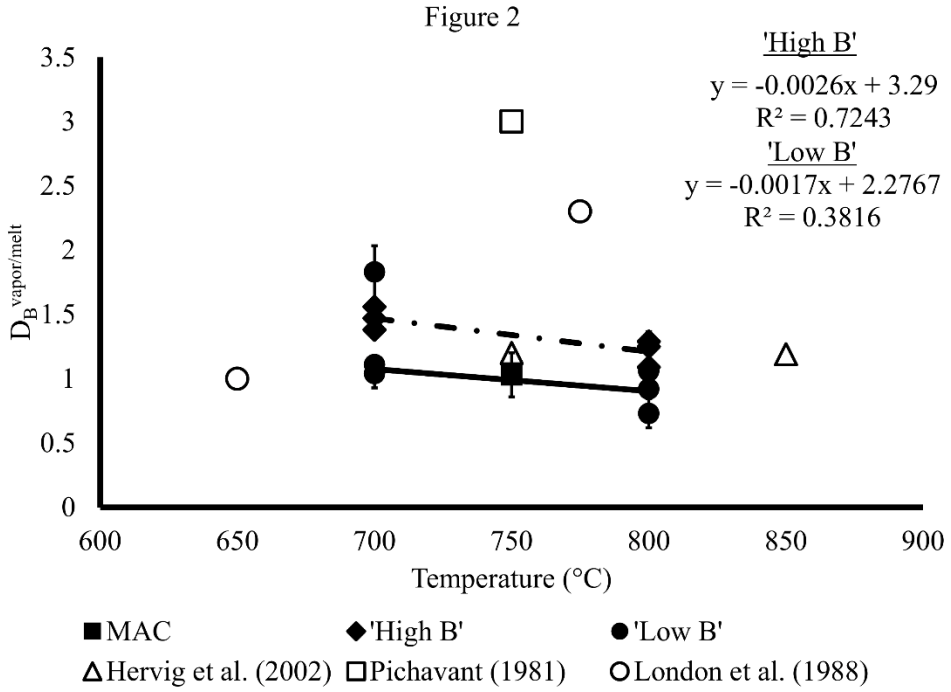

Figure 4-2 Partition coefficients for B, D_B, between aqueous solution (vapor) and melt as a function of temperature. 'High B' and 'Low B' refer to experiments using starting materials with ~ 5 and ~ 2.5 wt% B_2O_3, respectively. Solid black triangles represent data from 'High B' experiments, and solid black circles for 'Low B' experiments. Data collected from experiment CGB88, using MAC glass (labeled 'MAC' on diagram), is plotted as a solid black square. Also plotted are data from Hervig et al. (2002) (open triangles), Pichavant (1981) (open square), and London et al. (1988) (open circles). Error bars represent 2σ standard errors which were propagated through the calculation of partition coefficients. Values of D_B from the current study are not temperature sensitive, but do increase with increasing B content of melt, and are similar to data reported by Hervig et al. (2002) and London et al. (1988).

Figure 3

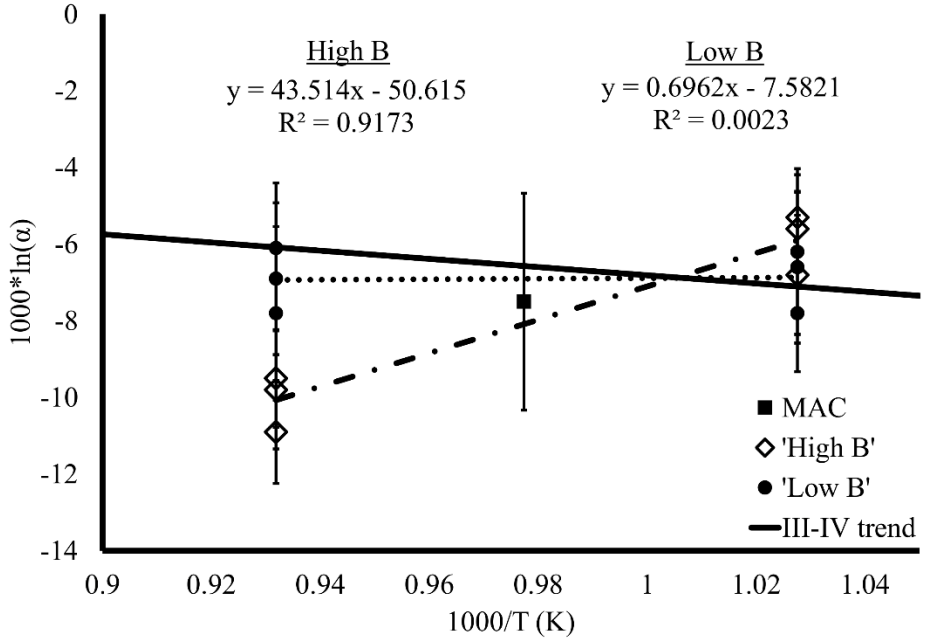

Figure 4-3 Boron isotopic fractionation factors (1000*lnα) from the current study plotted against reciprocal temperature (1000/T(K)). Data from 'High B' and 'Low B' experiments are plotted as open diamonds and solid circles, respectively. The solid square represents data from experiment CGB88, which used MAC glass (labeled as 'MAC' on the diagram). The dash-dot line is a linear regression through the 'High B' data, and the dotted line is a linear regression through the 'Low B' data. The solid black line is the 'III-IV' fractionation trend of Hervig et al. (2002), Williams et al. (2001a), and Wunder et al. (2005). Error bars are 2σ standard errors propagated through the calculation of fractionation factors for melt-aqueous solution.

Figure 4

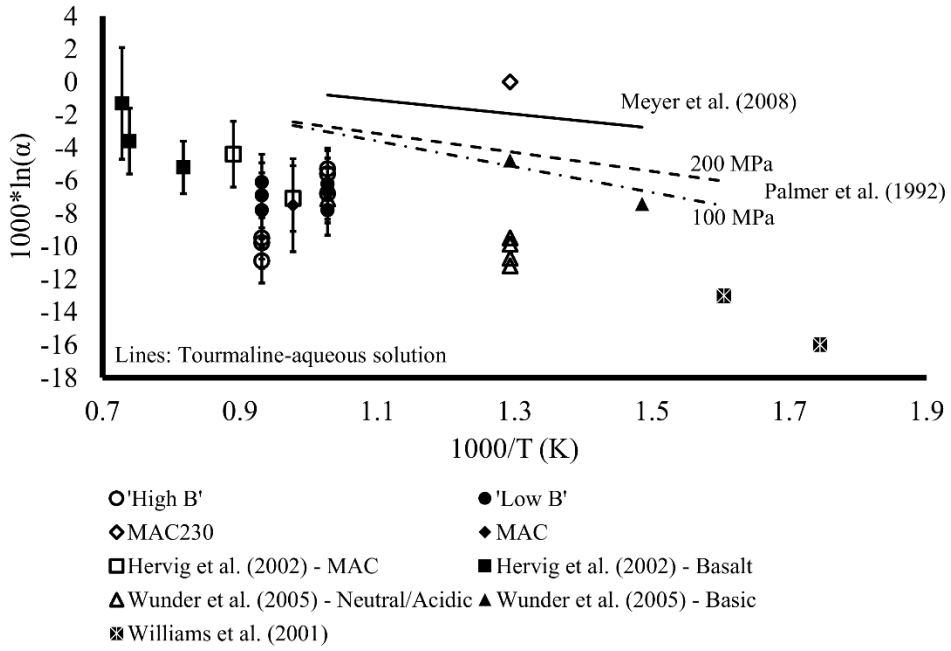

Figure 4-4 Comparison of boron isotopic fractionation factors (1000*lnα) measured in this and other studies plotted against reciprocal temperature (1000/T(K)). Data from other studies includes tourmaline-aqueous solution (Meyer et al., 2008: solid black line; Palmer et al., 1992: dashed line (200 MPa) and dash-dot line (100 MPa)), boromuscovite-aqueous solution (Wunder et al., 2005: open triangles (basic fluid) and solid triangles (neutral and acidic fluid)), illite-aqueous solution (Williams et al., 2001a: black squares with white asterix in center), and melt-aqueous solution (Hervig et al., 2002: solid squares (MAC) and open squares (basalt)). Open circles ('High B'), solid circles ('Low B'), open diamond (MAC230), and solid diamond (CGB88: using MAC glass) are from the current study. It is clear that the data from the current study plots, mostly, along a line through the data of Hervig et al. (2002), Williams et al. (2001a), and Wunder et al. (2005). Error bars represent 2σ standard errors propagated through the calculation of isotopic fractionation factors.

Table 4-1 Compositions of Starting Materials (SMs)

	HG	1σS.D.	2.5AN	1σS.D.	2.5CN	1σS.D.	2.5FN	1σS.D.	5AN	1σS.D.	5CN	1σS.D.	5DN	1σS.D.	MAC[1]
SiO_2	78.01	(0.76)	70.61	(0.50)	70.89	(0.57)	70.31	(0.70)	68.22	(0.60)	67.89	(0.62)	67.75	(0.67)	72.32
B_2O_3	---		2.53	(0.35)	2.63	(0.27)	2.60	(0.41)	5.63	(0.45)	6.16	(0.43)	5.85	(0.43)	0.62
Al_2O_3	12.51	(0.24)	11.26	(0.20)	11.36	(0.12)	11.26	(0.15)	11.00	(0.13)	10.81	(0.14)	10.81	(0.14)	15.63
Na_2O	4.21	(0.21)	3.60	(0.15)	3.57	(0.11)	3.60	(0.17)	3.45	(0.11)	3.45	(0.15)	3.43	(0.14)	4.10
K_2O	4.87	(0.11)	4.35	(0.13)	4.40	(0.17)	4.38	(0.11)	4.19	(0.13)	4.21	(0.14)	4.25	(0.11)	3.53
Total	99.6		92.35	(0.53)	92.84	(0.71)	92.15	(0.82)	92.49	(0.64)	92.51	(0.79)	92.10	(0.81)	96.20
H_2O[2]	---		7.65		7.16		7.85		7.51		7.49		7.90		
N[3]	50		25		25		25		25		25		25		
$\delta^{11}B$[4]			0.4		-1.2		-0.4		-0.5		-0.2				
2σS.E.			0.8		0.4		0.7		0.6		0.4				
N[5]			9		3		3		3		3				
$\delta^{11}B$[6]					-1.8								-0.7		-11.1
2σS.E.					0.7								0.6		0.7

[1]Macusani obsidian (London et al. 1988), total does not include minor and trace elements (e.g. F, Li, Cs)
[2]H_2O calculated as the difference of EMPA totals from 100%
[3]Number of EMPA data points (Cameca SX-100; University of Oklahoma, Norman, OK, USA)
[4]SIMS (Cameca IMS 6f; Arizona State University, Tempe, AZ, USA)
[5]Number of SIMS data points for $\delta^{11}B$
[6]MC-ICP-MS (Neptune Plus, ThermoScientific; analyses by ALS Scandinavia AB, Luleå, Sweden)

Table 4-2 P-T conditions for experiments and masses of glass and water

				Masses of materials (g)			
Exp#	T (°C)	t (days)	SM[1]	Initial glass	Initial H_2O	Final glass	Final aq. sln.
CGB86	750	1	MAC	0.01023	0.01477	0.01080	0.01420
CGB87	850	2	MAC	0.01485	0.02445	0.01564	0.02366
CGB88	750	90	MAC	0.01715	0.02332	0.01408	0.02639
CGB97	800	30	5AN	0.01110	0.00995	0.01040	0.01065
CGB98	800	30	5AN	0.02122	0.02006	0.02010	0.02118
CGB99	800	30	5AN	0.02198	0.01969	0.02086	0.02081
CGB100	700	30	5CN	0.03292	0.03478	0.03130	0.03640
CGB101	700	30	5CN	0.02045	0.01996	0.01968	0.02073
CGB102	700	30	5CN	0.02494	0.02501	0.02327	0.02668
CGB103	800	30	2.5AN	0.02916	0.02995	0.02749	0.03162
CGB104	800	30	2.5AN	0.02069	0.01969	0.02012	0.02026
CGB105	800	30	2.5AN	0.01641	0.01495	0.01585	0.01551
CGB106	700	30	2.5FN	0.01921	0.02031	0.01938	0.02014
CGB107	700	30	2.5FN	0.02402	0.02515	0.02374	0.02543
CGB108	700	30	2.5FN	0.02124	0.02207	0.02071	0.02260

[1]Starting material glass (refer to Table 1 for compositional information)

Table 4-3 Chemical composition of glass products

	CGB86	CGB87	CGB88	CGB97	CGB98	CGB99	CGB100	CGB101
T (°C)	750	850	750	800	800	800	700	700
t (days)	1	2	90	30	30	30	30	30
SM[1]	MAC	MAC	MAC	5AN	5AN	5AN	5CN	5CN
SiO_2	65.82 (0.41)	65.98 (0.28)	66.77 (0.26)	71.89 (0.31)	72.04 (0.38)	71.58 (027)	71.39 (0.27)	71.13 (0.38)
B_2O_3	0.56 (0.11)	0.43 (0.09)	0.71 (0.14)	2.75 (0.14)	2.88 (0.20)	2.99 (0.15)	2.93 (0.18)	2.73 (0.12)
Al_2O_3	14.69 (0.10)	14.78 (0.12)	14.70 (0.08)	11.45 (0.10)	11.47 (0.05)	11.39 (0.08)	11.32 (0.09)	11.42 (0.10)
Na_2O	3.54 (0.06)	3.64 (0.04)	3.53 (0.07)	3.77 (0.10)	3.76 (0.08)	3.72 (0.12)	3.64 (0.09)	3.64 (0.11)
K_2O	3.40 (0.04)	3.51 (0.04)	3.40 (0.06)	4.39 (0.10)	4.29 (0.08)	4.32 (0.07)	4.31 (0.04)	4.31 (0.07)
Total[2]	88.02 (0.49)	88.34 (0.34)	89.11 (0.32)	94.26 (0.49)	94.42 (0.41)	94.01 (0.41)	93.58 (0.38)	93.22 (0.47)
N	30	25	15	15	15	15	15	15
H_2O[3]	11.98	11.66	10.89	5.74	5.58	5.99	6.42	6.78
ASI[4]	1.55 (0.02)	1.51 (0.02)	1.55 (0.02)	1.05 (0.02)	1.06 (0.01)	1.06 (0.02)	1.06 (0.02)	1.07 (0.02)

[1]SM: Starting material glass (refer to Table 1 for composition)

[2]Totals for CGB86, 87, 88 do not include several minor to trace elements (e.g. Rb, Cs, F, Li)

[3]H_2O calculated as difference of EMPA totals from 100%; For MAC exps, H_2O estimate represents a maximum

[4]ASI: Aluminum saturation index (molar Al/Na+K)

Table 4-4 Boron isotopic fractionation factors and partition coefficients

				B_2O_3 (wt%)[2]					$\delta^{11}B$ (‰)					
Exp#	T (°C)	time (days)	SM[1]	Final glass	2σS.E.	Final aq. sln.	D_B	2σS.E.	Glass	2σS.E.	Aq. Sln.	Δ	2σS.E.	α
CGB86	750	1	MAC	---	---	---	---	---	-11.2	0.8	-10.8	-0.3	---	1.0001
CGB87	850	2	MAC	---	---	---	---	---	-10.4	0.7	-11.4	1.1	---	0.9993
CGB88	750	90	MAC	0.25	0.03	0.26	1.03	0.17	-16.0	2.0	-8.4	-7.5	2.8	0.9924
CGB97	800	30	5AN	2.68	0.06	3.36	1.25	0.04	-5.9	0.9	+3.7	-9.5	1.3	0.9905
CGB98	800	30	5AN	2.56	0.12	3.31	1.29	0.08	-6.2	1.1	+3.6	-9.8	1.5	0.9902
CGB99	800	30	5AN	2.89	0.23	3.16	1.09	0.12	-6.2	1.0	+4.7	-10.9	1.3	0.9891
CGB100	700	30	5CN	2.43	0.12	3.57	1.47	0.09	-4.5	1.1	+2.3	-6.8	1.6	0.9933
CGB101	700	30	5CN	2.46	0.04	3.84	1.56	0.03	-3.7	1.0	+1.9	-5.6	1.4	0.9944
CGB102	700	30	5CN	2.60	0.02	3.58	1.38	0.01	-3.5	0.9	+1.9	-5.3	1.3	0.9947
CGB103	800	30	2.5AN	1.66	0.15	1.20	0.73	0.11	-2.8	1.4	+4.1	-6.9	2.0	0.9931
CGB104	800	30	2.5AN	1.53	0.15	1.41	0.92	0.13	-2.6	1.2	+3.5	-6.1	1.7	0.9939
CGB105	800	30	2.5AN	1.46	0.13	1.54	1.06	0.13	-3.6	1.6	+4.2	-7.8	2.3	0.9922
CGB106	700	30	2.5FN	1.02	0.10	1.87	1.83	0.20	-5.5	1.1	+2.3	-7.8	1.5	0.9922
CGB107	700	30	2.5FN	1.43	0.11	1.49	1.04	0.11	-3.7	1.1	+2.5	-6.2	1.6	0.9938
CGB108	700	30	2.5FN	1.39	0.03	1.54	1.11	0.03	-4.0	1.4	+2.6	-6.6	2.0	0.9934

[1]Starting material glass (refer to Table 1 for compositional information)

[2]SIMS measurement

Chapter 5 The relationship of Mn enrichment and spessartine saturation in granite-pegmatite systems

1. Introduction

Garnet rich in spessartine (Sps) component, $Mn_3Al_2Si_3O_{12}$, occurs principally in three geologic environments. One is in coticules, which are products of metamorphism of Mn-rich oxide nodules in aluminous marine sediment (Romer et al., 2011). A second setting is as euhedral crystals within lithophysae formed in lava flows of F-rich rhyolites, and in their analogous miarolitic granites (Christiansen et al., 1984). The third, and far more common, occurrence is in association with highly-fractionated peraluminous granites and pegmatites, those that are characterized as S-type (Chappell and White, 2001). The study presented here applies entirely to the third environment.

Melt generated by the anatexis of metasedimentary rock, the source material of peraluminous S-type granites, contains minor to trace concentrations of the mafic elements Fe, Mg, and Mn (e.g., Acosta-Vigil et al. 2007). However, the end stages of crystallization of S-type granitic magmas culminate in pegmatites that commonly contain spessartine-rich garnet and several phosphates near their Mn end-member compositions. Černý et al. (1985) showed that the Fe/Mn ratio decreases and Mn content of garnet increases with the progress of crystallization from parental granites to the most evolved types of granitic pegmatites The evolutionary trend in garnet (Černý et al. 1985) could be construed to signify that Fe is more compatible in garnet than is Mn, such that the eventual crystallization of spessartine results mostly from the depletion of Fe in melt through the crystallization of garnet. Experiments that entailed

the crystallization of garnet from silicic melt at the moderate pressure and temperature (600°-750°C, 200 MPa) of the cordierite-andalusite facies demonstrated that Mn is more compatible than Fe in garnet at these conditions (Icenhower, 1995). Therefore, other mafic phases (biotite, cordierite, and tourmaline) in which Mn is less compatible than Fe apparently control the fractionation patterns for garnet in these rocks (London et al., 2001). The experimental study present here serves as a test of that hypothesis.

1.1. Prior Experimentation

The exchange of Fe and Mg between biotite and garnet (Holdaway 2004, and references therein) and between garnet and cordierite (Dwivedi et al. 1998, and references therein) have been thoroughly investigated. Most such studies entailed hydrothermal synthesis, and a melt was not present. Partition coefficients for mafic components between tourmaline and other mafic minerals or melt are similarly unknown. Van Hinsberg and Schumacher (2009) attempted to calibrate the distribution of Fe and Mg between tourmaline and biotite at hydrothermal conditions, but their experimental results showed almost no correlation between Fe-Mg exchange and temperature.

The compatibility of Mn in biotite, garnet, and cordierite, and the partition coefficients for Mn between minerals and melt, are essentially unstudied through experimentation. Though mineral-melt partition coefficients for Fe and Mg might be extracted from a few experimental investigations in which mafic minerals coarse enough for analysis grew from the melt, that is not true for Mn. Because of low Mn concentrations in typical starting materials, the concentrations of Mn in most experimental products are at or below detection levels by electron microprobe analysis.

Maner et al. (2013) attempted to calibrate the exchange of Fe and Mn between garnet and tourmaline as a potential geothermometer for peraluminous granitic pegmatites. Like van Hinsberg and Schumacher (2009), Maner et al. (2013) documented a wide spread in the partition coefficients and a poor correlation of element exchange with temperature. Moreover, very low compatibility of Mn in tourmaline brought that phase to saturation in Mn at nearly trace levels.

Though progress has been made toward understanding the mechanisms that control the compositions of garnet crystals in granitic igneous rocks, the partition coefficients for Mn among garnet, tourmaline, biotite, cordierite, and hydrous, boron-bearing peraluminous granitic melt have not been ascertained. These data are necessary for quantitative chemical modeling (e.g., via Rayleigh fractionation) of the Mn contents of granitic liquids. Toward this end, the primary goals of this study are to present mineral-melt partitioning measurements for Mn, Fe, and Mg between boron-bearing, hydrous, peraluminous granitic melt and garnet, tourmaline, and cordierite. Other experimental data ($D_M^{Bt\text{-}melt}$ and $D_M^{Ms\text{-}melt}$: Icenhower 1995; Icenhower and London 1995) are included as needed for Rayleigh modeling. The Rayleigh model serves as a test of the validity of the experimental data for the accumulation of Mn from anatexis to crystallization of two-mica granite. Starting with an appropriate liquid composition and mineral modes, the model should, and does, predict spessartine saturation only after extended crystallization of the initial melt at near-minimum temperatures.

2. Methods

2.1. Experimental Design

Experiments were designed to crystallize tourmaline, garnet, and cordierite from nearly crystal-free hydrous, boron-bearing, peraluminous granitic melt. Several experiments were heated to 800°C or 850°C and quenched to check for crystallinity and chemical homogeneity of the resultant liquid (quenched to glass). Experiments intended to produce crystalline phases were either (1) quenched to room temperature from 850°C then heated directly to the temperature of interest, or (2) dropped down from 850°C in a single isobaric cooling step to a synthesis temperature. The former experiments are referred to as forward-direction experiments and the latter as reverse-direction experiments. Replicate experiments conducted at 650°C, 700°C, and 750°C had run durations between 1 and 30 days, forming a time-series for these temperatures. The compositions of glasses and minerals produced in these experiments were monitored for changes over time. A period of 14 days at 750°C and 30 days at 650°C proved to be sufficient for attainment of steady-state conditions, as indicated by constancy of the compositions of garnet rims and immediately adjacent glass. Partition coefficients were determined using the compositions of crystal rims and adjacent liquid (glass) from all experiments, both forward and reverse thermal direction[1], on the grounds that steady-state results (i.e., constancy of mineral and melt compositions with time) reflected a close approach to local equilibration between crystal and melt.

[1] Mineral-melt exchange coefficients are equivalent to Nernst distribution coefficients, which represent the product of a homogeneous exchange reaction. In this case, the reaction is between crystal and melt. Crystallization of minerals from melt represents the principal and only feasible means of measuring the elemental partition coefficients. A reversal of this reaction requires diffusion of the element(s) of interest out of a crystal into melt until both phases, crystal and melt, have been equilibrated. Solid-state diffusion of mafic components through a crystalline phase is impossibly slow on the time frames of experiments. Moreover, a crystal that is not in equilibrium with melt will dissolve at a rate much greater than that of the solid-state diffusion of ions through the crystal (e.g., Bea 1996)

2.2. Preparation of Starting Materials for Experiments

Starting materials for experimental work included high-purity chemical reagents, a fabricated glass, and natural minerals. The base compositions of all starting material mixtures were designed to be near the minimum composition of the metaluminous haplogranite system at 200 MPa_{H2O} (Tuttle and Bowen, 1958). This was accomplished by either using a synthetic glass (HG glass, Table 5-1) or by combining natural and synthetic minerals (Table 5-1) and chemical reagents.

The experimental study of Wolf and London (1997) provided the starting point for our experiments. Wolf and London (1997) showed that the stability of tourmaline in granitic melt is a function of the B content and the aluminum saturation index (ASI) of melt, calculated as molar Al/(Na+K+2Ca), such that at 750°C, tourmaline will crystallize in granitic melts having an ASI of at least 1.2 and B_2O_3 contents above 2 wt.% oxide. The ASI of each starting mixture used in the present study was controlled by adding aluminous minerals (Table 5-1) or aluminum oxide/hydroxide chemical reagents to starting material mixtures to achieve a value of at least 1.2. Boron was added to all starting material mixtures as either (1) B_2O_3 glass, made by dehydrating boric acid in a Pt dish over a Bunsen burner, or (2) reagent-grade borax ($Na_2B_4O_7{\cdot}10H_2O$). Mixtures GT1.2 and GT1.2+ contained ~3 to 4 wt.% B_2O_3 whereas others (GT1.3 and MnGT-BC-4.1) contained between 6 and 8 wt.% B_2O_3. The higher boron contents ensured a yield of tourmaline crystals at the final run temperatures that was sufficient for microanalysis.

The minimum concentrations of mafic oxide components in glass (melt) that are necessary to promote the growth of tourmaline were reported by Wolf and London

(1997), and those values served as a baseline for this study. All starting material mixtures contained more than 1 wt.% MnO to facilitate the growth of Mn-rich garnet (Icenhower, 1995). Mafic components of each mixture were added as natural minerals (Table 5-1), Fe metal, and/or MnO (see Appendix 2 for details of preparation).

2.3. Experimental Procedure

Each experiment began by adding deionized and ultra-filtered water (DIUF; Fisher Scientific) to a gold capsule of 20 x 3 mm and a wall thickness of 0.2 mm, followed by 50 to 100 milligrams of a starting material mixture. Loaded capsules were wrapped with a sleeve of damp paper, frozen using cryogenic spray to reduce volatilization of water during welding, and sealed by TIG (Tungsten-Inert Gas: argon) welding. The capsule was then weighed to check for loss of water during welding, labeled with the appropriate experiment number, reweighed, placed in an oven at ~120°C for at least 1 hour, and then reweighed again to check for leaks in the capsule (detected as water loss by weight loss). Only capsules showing no leakage after sealing were utilized.

Experiments were conducted open to a 2-liter pressure buffer in NIMONIC© 105 or UDIMET cold-seal pressure vessels with water (plus a trace of Immunol™ as a rust inhibitor) as the pressure medium. The cool end of each vessel was tilted ~5° below horizontal to prevent the convection of water within the vessel. Hastelloy-C filler-rods, which surround the thermocouple, also reduced convection of water and heat. Temperature was monitored with an internal Chromel-Alumel thermocouple, and pressure was monitored with a factory-calibrated Heise bourdon tube gauge. Uncertainties in temperature and pressure are <10°C and <10 MPa, respectively.

Isobaric quenching was performed by removing the vessel from the furnace and applying a jet of compressed air. The average rate of cooling is approximately 200-300°C/min; vessels were cooled to below 150°C before de-pressurization. Once the vessel was cool enough to handle, capsules were removed, rinsed with water, dried, weighed to check for leaks produced in the capsule during the experiment, punctured to check for free water or volatiles, and then opened to examine the products.

2.4. Fugacity of Oxygen in Experiments

The oxygen fugacity, $f(O_2)$, of the experimental system is buffered by a reaction between the water pressure medium and the Ni-based vessel and filler rod alloys. The $f(O_2)$ of the experimental apparatus is half a log unit below the Ni-NiO oxygen buffer (NNO) (Wolf et al., 1994) as determined from the solubility of cassiterite in reference to values cited by Taylor and Wall (1992). At this $f(O_2)$, the fraction of Fe^{3+}/Fe^{2+} is less than 0.1, based on the work of Moore et al. (1995) and Baker and Rutherford (1996) for metaluminous granitic melts at NNO and temperatures below 900°C. The fugacity of oxygen at the NNO oxygen buffer is below that of the $Mn_{1-x}O/Mn_2O_3$ oxygen buffer (Huebner and Sato, 1970); therefore, all Mn should carry 2+ charge.

2.5. Preparation of Experimental Products for Analysis

Experimental products were initially examined by using a stereoscopic binocular zoom microscope and oil- and/or epoxy-immersed grain mounts using a transmitted light petrographic microscope. Products were prepared for qualitative and quantitative electron microprobe analysis (EMPA) by placing products in 1" circular molds or ¼" brass holders and impregnated with EpoThin™ epoxy (Buehler). Epoxy mounts were progressively ground down with lapping films to a 3 μm grit size, and then polished

using diamond in water to a final grit size of ≤ ¼ μm. Polished experimental products were rinsed with alcohol, dried in a jet of air, and then placed in a desiccator prior to application of a carbon coat.

2.6. Electron Beam Analytical Methodology

Most of the imaging and analyses were performed with a CAMECA SX50 electron microprobe at the University of Oklahoma. This instrument was equipped with five wavelength-dispersive spectrometers, a PGT Prism 2000 Energy-Dispersive X-ray Analyzer (EDXA) with Moxtek polymer entry window, and PC-based SAMx^{TM} automation system for both analysis and imaging. A small number of analyses were performed using a CAMECA SX100 microprobe beginning in 2015. Qualitative phase identification was accomplished using backscattered electron imaging coupled with EDXA using either a 15 or 20 kV accelerating voltage and 20 nA beam current.

Quantitative analyses were performed by Wavelength-Dispersive Spectrometry (WDS). Analytical conditions for tourmaline, garnet, and cordierite utilized a 15 kV accelerating voltage, 20 nA beam current, and 2 μm spot. Elements analyzed in tourmaline included B, F, Na, Mg, Al, Si, Ca, Ti, Mn, Fe, and Zn and detection limits were less than 0.05 wt.% oxide except for B and F which have detection limits of 0.24 wt.% oxide and 0.20 wt.% element, respectively. Garnet and cordierite crystals were analyzed for Fe, Mn, Na, Si, Cr, Ti, Al, Mg, K, and Ca; detection limits were below 0.06 wt.% oxide. Glass analyses used a two-condition routine to mitigate the migration of Na during analysis (Morgan and London 1996; Morgan and London 2005). The first condition used 15 kV accelerating voltage, 2 nA beam current, and 20 μm spot for analysis of Na, K, Ca, Al, and Si; the second condition used 15 kV accelerating voltage,

40 nA beam current, and 20 µm spot for analysis of Mg, Mn, Fe, Ti, F and B. Counting times for all elements resulted in detection limits less than 0.05 wt.% oxide except for B and which had detection limits of 0.24 wt.% oxide and 0.13 wt.% element, respectively. Data reduction employed the PAP method (Pouchou and Pichoir, 1985).

2.7. Mineral Formula Calculations

Chemical formulae for garnet and cordierite crystals were calculated from EMPA chemical data based on 12 and 18 oxygen atoms, respectively. The chemical formula of the garnet group is $\{X_3\}[Y_2](Z_3)O_{12}$ (Grew et al., 2013). Site assignments follow the method of Grew et al. (2013), and only include elements analyzed in this study. The chemical formula of the cordierite group is $M_2Al_4Si_5O_{18}$, where M can be occupied by Fe, Mg, and Mn.

The chemical formula for minerals of the tourmaline supergroup is $XY_3Z_6(BO_3)_3(T_6O_{18})(V)_3(W)$ (Henry et al., 2011). Cations were calculated from EMPA data on a 29 oxygen atom basis. An Excel^{TM} spreadsheet developed by Morgan (2016) was used to calculate the percentages of end-member tourmaline components from the EMPA data.

3. Results and Discussion of Results

3.1. Synthetic phases

Synthetic crystalline products include tourmaline, cordierite, and garnet, along with quartz and alkali feldspar, corundum/mullite and spinel-group oxides. Quartz and alkali feldspar crystallized only in experiments conducted below 700°C (Figs.5-1D, 5-1H, 5-1I), whereas minor to trace amounts of corundum/mullite and mafic oxides precipitated in all experiments.

Tourmaline formed euhedral, prismatic crystals in experiments between 750° and 700°C, in both forward and reverse experiments (Figures 5-1B & 5-1C). Below 700°C, tourmaline crystallized as radial clusters intergrown with quartz (Figure 5-1) and as isolated skeletal (soda–straw) crystals irrespective of thermal direction.

Garnet and/or cordierite were produced above 750°C. Garnet and cordierite crystallized prior to and simultaneously with tourmaline in some experiments below 750°C. Garnet and cordierite consistently formed euhedral crystals and display abrupt core-rim chemical zonation in all experiments (cordierite: Figure 5-1H).

3.1. Chemical Compositions of Garnet, Tourmaline, Cordierite, and Glass

3.1.1. Garnet

Garnet crystals are a solid solutions of spessartine (Sps), almandine (Alm), and pyrope (Prp) components (Table 5-2). The compositions of garnet generally follow a temperature-dependent trend from $Sps_{51}Alm_{23}Prp_{25}$ to $Sps_{81}Alm_{15}Prp_{4}$ with decreasing temperature (Figure 5-2). A full Y-site, i.e. two Al cations, is supportive evidence of a low fraction of Fe^{3+} in melt.

3.1.2. Tourmaline

Tourmaline crystals are dominantly a solid-solution of schorl, dravite, and foitite with minor amounts of uvite (Table 5-3). The MnO content of tourmaline increases linearly from 0.67 wt% at 750°C to 2.17 wt% at 650°C. Tourmaline crystals produced at 700°C display weak hourglass sector-zonation; the *a* and c^- axial sectors are Al- and Ca-rich and Mg-poor relative to the c^+ axial sector (Maner et al., 2014).

3.1.3. Cordierite

Cordierite (Crd) crystals are Mg-rich at high temperature and evolve toward higher Fe (sekaninaite, Sek) compositions with decreasing temperature (Figure 5-3). The Mn contents of cordierite increase with decreasing temperature up to 7.37 wt% MnO (Table 5-4). Five cordierite crystals from experiment GBT-103 (650°C, 200 MPa, 456 hrs) were analyzed using the analytical method for tourmaline and were found to contain 2.59 wt.% B_2O_3 (1σSD: 0.22), with analytical totals near 100% (i.e. little to no water content). Sodium contents are above detection limit; no systematic relationship between Na and (1) any other compositional parameter of cordierite or (2) temperature was not identified.

3.1.4. Glass

Compositions of all glasses (melts) are reported in Table 5-5. Apart from composition GT1.3, which has a higher normative quartz component, glass (melt) compositions lie near the thermal minimum of the haplogranite system. The sum of FeO, MnO, and MgO decreases from 1.56 wt% to 0.62 wt% from 750°C to 650°C in experiments that produced both garnet and tourmaline. Concentrations of MnO, FeO, and MgO in glass increase exponentially with temperature (Figures 5-4a through 5-4c). The normative corundum component of glass increases with temperature (Figures 5-5a and 5-5b). The B_2O_3 content is either ~3 wt.% or ~8 wt.%, depending on the composition of the starting material mixture.

3.2. Mineral-Melt Partition Coefficients and Exchange Coefficients

Partition coefficients, $D_M^{\alpha/L}$, where α is a mineral and L is melt, were calculated as the concentration in weight percent of an oxide in mineral divided by the weight

percent oxide in glass (Beattie et al., 1993). Partition coefficients for MnO, FeO, and MgO between garnet- and cordierite-melt were measured in the temperature interval 650°C to 850°C and 650°C to 750°C for tourmaline-melt, (Table 5-6). Data for $D^{Ms/melt}$ and $D^{Bt/melt}$ (Icenhower and London, 1995), and $D^{Crd/melt}$ (Icenhower, 1995) are reported in Table 5-6 to complement and compare to the data measured in this study. All values of $D_M^{\alpha/L}$ measured in the present study increase with decreasing temperature (Figures 5-6a though 5-6c) and, except for $D_{MnO}^{Tur\text{-}melt}$ above 650°C, all partition coefficients are ≥ 1. It is for these reasons that the total mafic component of anatectic granitic melts (saturated in one or more of these mafic minerals) is < 2 wt% total oxides and < ~ 4 % of normative mafic mineral components (e.g., Table 5-5), and those values decrease with crystallization toward the thermal minimum, resulting in nearly mafic-free leucogranites and pegmatites.

Exchange coefficients, given the symbol $K_{DM/N}$ where *M* and *N* are different oxides (Beattie et al., 1993), compare pairs of oxide partition coefficients for the same mineral (see footnote 1). All exchange coefficients are constant over the range of temperatures investigated. Average values of $K_{DM/N}$ are reported in Table 5-6. Figures 5-7a and 5-7b show exchange coefficients MgO/FeO and MnO/FeO for garnet, tourmaline, muscovite, biotite, and cordierite. In these diagrams, the slope of the line regressed through the data represents the exchange coefficient, e.g. $K_{DMnO/FeO}$. A slope greater than one indicates that the element in the numerator will be depleted from melt faster than the element in the denominator.

4. Discussion

4.1. The evolution of MgO/FeO and MnO/FeO of melt during fractional crystallization

The MgO/FeO ratios of granites decrease (Frost et al. 2001, and references therein) and MnO/FeO increase (Černý et al., 1985) during the fractional crystallization of primary S-type granitic melts. An increase in the MnO/FeO ratio during fractional crystallization of granitic magma must be controlled by the crystallization of minerals in which Mn is less compatible than Fe and Mg. Similarly, the MgO/FeO ratio decreases due to the greater compatibility of Mg compared to Fe in mafic phases at high temperature. The data plotted in Figures 5-7a and 5-7b show that crystallization of biotite, muscovite, and cordierite depletes the melt in MgO relative to FeO most effectively, whereas the crystallization of tourmaline, muscovite, and biotite promotes an increase in the MnO content of melt relative to FeO. These trends are seen more clearly in solutions to the Rayleigh fractionation equation,

$$\frac{C}{C_o} = F^{\alpha-1}$$

by which the individual effects of biotite, garnet, cordierite, and tourmaline crystallization on the exchange coefficients MgO/FeO (Figure 5-8a) and MnO/FeO (Figure 5-8b) of residual melt are modeled. The vertical axis in Figures 5-8a and 5-8b represents values of C/C_o, where C is the final concentration and C_o is the initial concentration, and the horizontal axis is F, the fraction of liquid (melt) remaining. Alpha, α, is the bulk partition coefficient. An increase in C/C_o reflects an increase in the MgO/FeO or MnO/FeO ratio of the residual melt. The curves representing MgO/FeO and MnO/FeO in Figures 5-8a and 5-8b, respectively, show that crystallization of garnet

will increase the MgO/FeO ratio and decrease the MnO/FeO of melt, whereas crystallization of muscovite, biotite, tourmaline, and cordierite has the opposite effect on melt composition. Values of $K_D^{MnO/FeO}$ decrease in the sequence from garnet to cordierite to biotite/muscovite to tourmaline (Figure 5-7b). Thus, the crystallization of garnet only will produce a steady decrease in the MnO/FeO ratio of melt and of garnet (e.g., Müller et al. 2012). Among all mafic phases, the MnO/FeO ratio of the melt increases most rapidly with the crystallization of tourmaline.

The $K_{DMnO/FeO}$ for cordierite-melt is noteworthy because it is greater than the $K_{DMnO/FeO}$ for biotite- or muscovite-melt, which means that cordierite-bearing S-type granites will require a greater extent of crystallization to reach saturation in Mn-rich garnet (Figure 5-8b), or may not achieve that saturation at all (e.g. Phillips et al. 1981; Pereira and Bea 1994; White et al. 2001). The paucity of garnet in the cordierite-bearing S-type granites of western Europe likely results from low-pressure fractional crystallization involving cordierite as the dominant ferromagnesian phase (e.g., Peña Negra complex, Avila batholith, Spain: Pereira and Bea 1994; Albuquerque pluton, Spain: London et al. 1999; Land's End pluton, U.K.: Müller et al. 2006).

4.2. Modeling the concentrations of MnO, FeO, and MgO during fractional crystallization

As a test of the $D_M^{\alpha/L}$ data reported in this manuscript, we use the garnet solubility data and $D_M^{\alpha/L}$ values (Tables 5-5 and 5-6) in a Rayleigh model to evaluate the concentrations of FeO, MnO, and MgO during fractional crystallization. By design, the model pertains to the crystallization of cordierite-bearing S-type granitic melt of anatectic origin that has migrated to pressures below ~ 400 MPa (i.e., in the stability

field of andalusite), such that almandine-pyrope solid solutions would likely not crystallize (Clemens and Wall, 1981; Pereira and Bea, 1994; Stevens et al., 2007). These results would apply to the cordierite-bearing granites of the Lachlan fold belt, Australia (White et al., 2001) and similar granites in Western Europe (e.g., Strong and Hammer 1981; Pereira and Bea 1994; Villaseca et al. 1998).

The model begins with the average composition of 63 analyses of vitreous melt inclusions (MI) hosted by garnet in a quartz-absent, Grt-Bt-Sil metapelitic enclave within the El Hoyazo dacites, SE Spain, (Acosta-Vigil et al., 2007). Acosta-Vigil et al. (2010) concluded that the MIs in garnet were formed during the dehydration-melting of muscovite at a temperature of ~685°-750°C and pressure of 5-7 kb. Though garnet is stable in the metapelitic enclave, at lower pressure (<4 kb), cordierite (sekaninaite) will form at the expense of garnet (almandine) (Mukhopadhyay and Holdaway, 1994) in a peraluminous liquid. Therefore, at 2 kb and 800°C, cordierite and biotite are stable phases that could crystallize from the liquid represented by the MI in garnet. Details regarding the calculation of mineral modes, bulk distributions coefficients, and how mineral modes and bulk distribution coefficients were varied as a function of temperature (T) and liquid fraction (F) are presented in Appendix 2.

The result of the Rayleigh model is depicted in Figure 5-9. In addition to the Rayleigh curve shown in Figure 5-9, we also plot the saturation surface for garnet in B-bearing, hydrous granitic melt based on the experimental data in Table 5-5. The model shows that the MnO content of melt intersects the saturation surface for garnet after ~90% fractional crystallization (F≈0.10; ~665°C, ~0.4 wt.% MnO). Variations in melt composition and the choices of mafic minerals and their proportions will of course

change the results (see a discussion in Appendix 2). Nonetheless, the Rayleigh model presented here using the partition coefficients of this study produce a result with a hypothetical, but realistic, S-type granitic liquid that is consistent with natural occurrences of spessartine. To that extent, the agreement between the Rayleigh model and the natural occurrences leads to the conclusion that the partition coefficients derived from this study are applicable to natural settings, and that Rayleigh fractional crystallization, wherein the entire bulk melt remains in chemical equilibrium with the rims of growing crystals, is applicable to the relatively large masses of normal granite plutons. That is not the case for granitic pegmatites, which are derived from the extended fractional crystallization of such plutons.

4.3. Spessartine in granitic pegmatites

The condition of equilibrium between crystals and a bulk melt whose composition changes continuously with crystallization does not apply to the internal evolution of granitic pegmatites. These have been shown to crystallize at ~ 450°C, which is ~ 200°C below the likely liquidus temperature (e.g., Morgan and London 1999; London et al. 2012). At such low temperatures, hydrous granitic liquids possess high viscosity (~ 10^8 Pa·s based on Giordano et al. 2004). That high viscosity will result in commensurately low diffusivity, especially of high field-strength (HFSE) cations (e.g., Mungall 2002). Whereas alkalis such as Cs exhibit exponential changes in abundance from margin to core that are similar to Rayleigh fractionation trends (London et al., 2012), Mn and Fe in garnet and tourmaline define "L" shaped patterns that are not those of Rayleigh fractionation (Morgan and London, 1999). The "L" shaped patterns of HFSE could result from constitutional zone refining (Morgan and

London, 1999), or they may reflect no fractionation of melt because of the low diffusivity of cations through melt in relation to the rate of advance of the crystallization front (London, 2014, 2008). It is for these reasons that Rayleigh modeling of the MnO content and $K_{DMnO/FeO}$ is invalid for granitic pegmatites.

Our partitioning data do show, however, that among the mafic minerals and muscovite, the crystallization of tourmaline alone is the most effective driver of the melt composition to the high MnO/FeO ratios and MnO content that would foster the crystallization of spessartine. Tourmaline is a characteristic mineral of the border and wall zones of pegmatites (Cameron et al., 1949), where it tends to crystallize in abundance (e.g., Fig. 2 of Černý et al. 2012). As a result, spessartine, or Mn-phosphate equivalents (London et al., 1999; London and Burt, 1982), are common phases in the interior zones of tourmaline-rich pegmatites.

5. Implications

The experimentally derived mineral-melt partition coefficients, $D_M^{\alpha/L}$, and exchange coefficients, $K_{DM/N}$, presented in this study confirm that the general fractionation trend of garnet, in which the MnO/FeO ratio increases with increasing fractional crystallization (Černý et al., 1985), is controlled not by garnet but by other minerals that accommodate Fe and Mg over Mn. The data show that crystallization of garnet alone at the moderate pressures cited here will result in a decrease in the concentration of MnO in melt that would likely preclude garnet saturation at pressures below ~ 400 MPa.

Among the minerals examined in this study, tourmaline is shown to be the most efficient at driving the concentration of MnO in melt to garnet saturation. Though Mn

behaves compatibly in cordierite, muscovite, and biotite, Fe and Mg are so much more compatible that the MnO content of melt increases when biotite or even cordierite dominates the mafic mineral assemblage. Granites that contain cordierite may never reach garnet saturation.

This study elucidates part of the geochemical cycle of Mn in the continental crust: the accommodation and enrichment of Mn in granitic liquids from deep sources of anatexis to shallow levels of solidification and crystallization of spessartine-bearing granites and pegmatites. These results bear directly on the formation of highly-prized, gem-quality spessartine, which is mined from granitic pegmatites (Laurs and Knox, 2001). The measured partition coefficients may also be pertinent to other types of Mn ores (e.g., Roy 1997).

The model presented here indicates that extensive fractional crystallization ($\geq$ 90%) of a starting anatectic melt is necessary to bring granitic liquids to saturation in spessartine at near-solidus conditions. Likewise, beryl (Be), tourmaline (B), spodumene (Li), and pollucite (Cs) achieve saturation in pegmatite-forming melts only after very extended fractional crystallization, and mostly at subsolidus temperatures of crystallization (i.e., in highly undercooled melt: London 2008). This study adds one more piece of evidence to the paradigm for rare-element pegmatites: such bodies arise only from extended fractionated of large granitic bodies, and cannot arise directly from small batches of anatectic melts (cf. Stewart 1978; Shearer et al. 1992; Simmons et al. 1996).

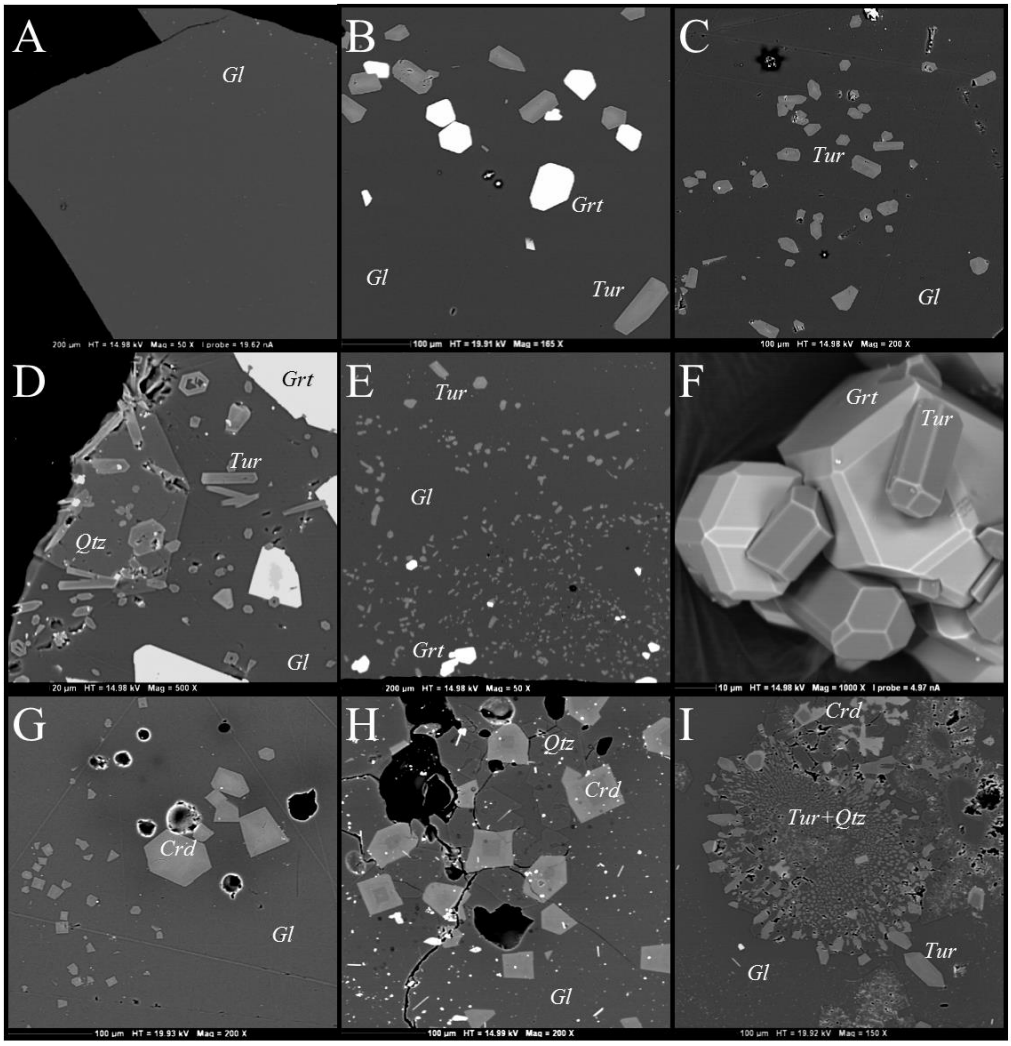

Figure 5-1 Back-scattered electron images (BSEI) of experimental run products. Grt garnet, Tur tourmaline, Crd cordierite, Qtz quartz, Gl glass. (A) Glass run product (Exp#: MnGT-80, 850°C). Experiments represented in (B) through (F), (H), and (I) were heated to 800°C or 850°C (pre-conditioning step) prior to quenching and 'forward' direction to crystallization temperature or 'reverse' direction from the pre-conditioning step. (B) Grt and Tur growth (Exp#: MnGT-49, 'forward' to 700°C). (C) Grt and Tur growth (Exp#: MnGT-56, 'reverse' to 700°C). (D) Grt, Tur, and Qtz growth (Exp#: MnGT-57, 'forward' to 600°C). (E) Grt and Tur growth (Exp#: MnGT-58, 'reverse' to 600°C). (F) Euhedral Grt and Tur crystals dissolved out of glass using hydrofluoric acid (Exp#: MnGT-56). (G) Crd growth (Exp#: GBT-90, 850°C). (H) Crd and qtz growth (Exp#: GBT-102, 'forward' to 700°C). (I) Crd, Tur, and Qtz growth (Exp#: GBT-103, 'forward' to 650°C).

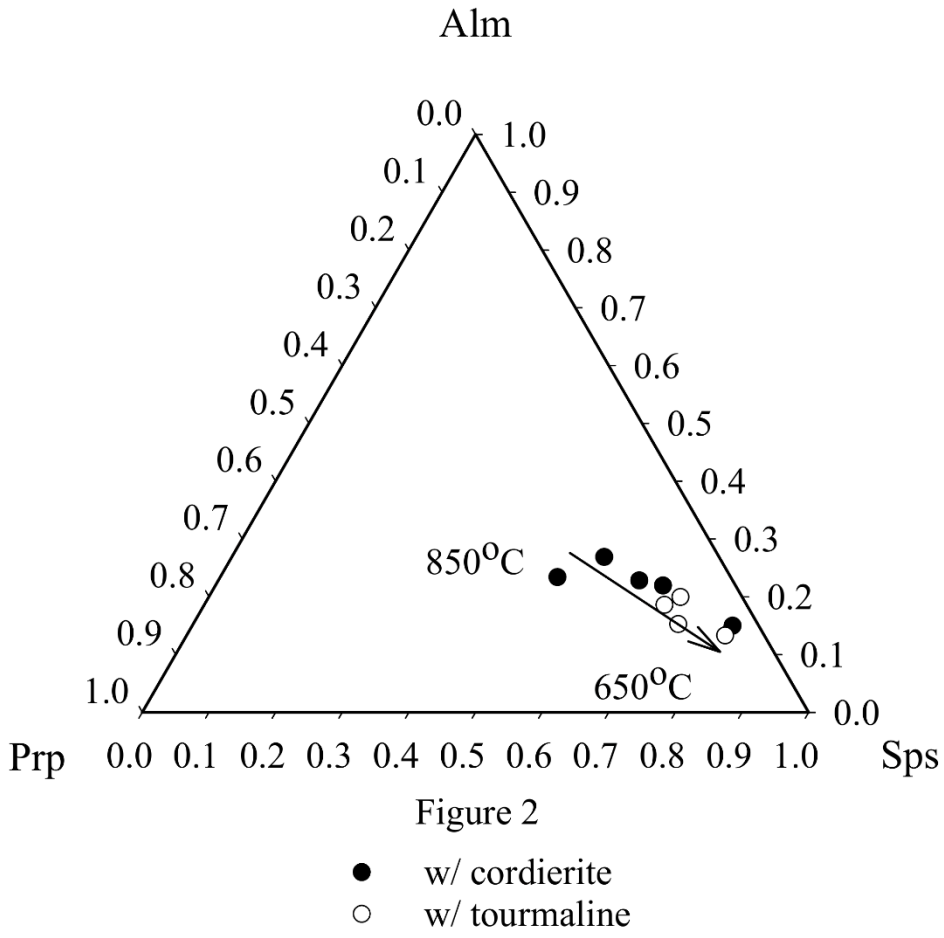

Figure 5-2 Ternary diagram of end-member garnet components produced in experiments. Sps spessartine, Alm almandine, Prp pyrope. Solid circles represent data from experiments that produced cordierite with garnet. Open circles represent data from experiments that produced tourmaline with garnet. Note a general linear trend perpendicular to the almandine-pyrope binary at $Alm_{50}Prp_{50}$. Garnet compositions become more Mn-rich (move toward the Sps apex) with decreasing temperature.

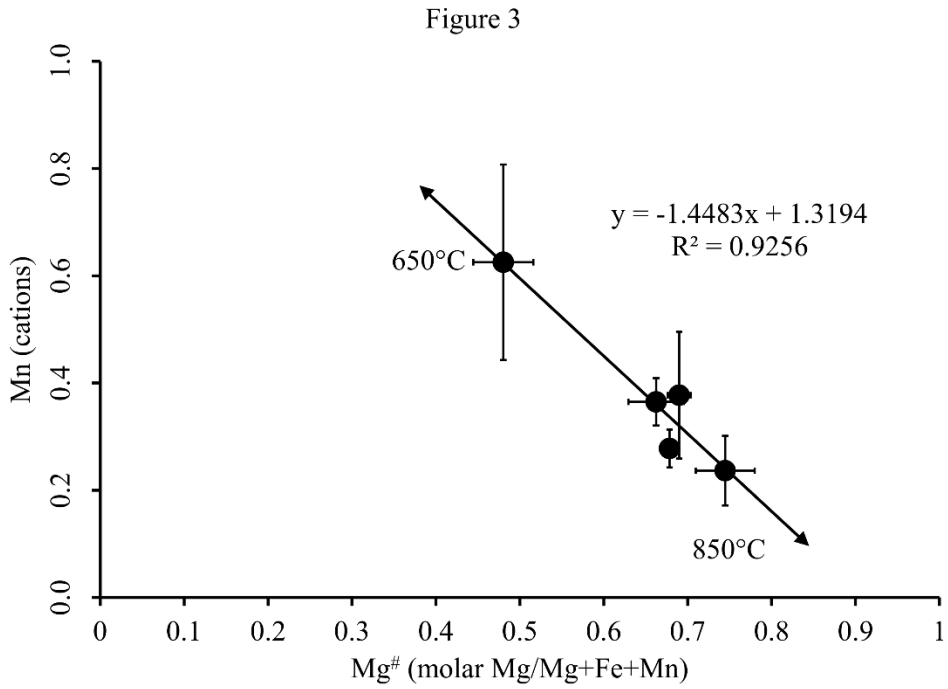

Figure 5-3 Compositions of cordierites produced in experiments. Mn content increases with decreasing temperature. Note at $Mg^{\#}=0$, Mn≈Fe and Mn+Fe≈2 (a full M-site).

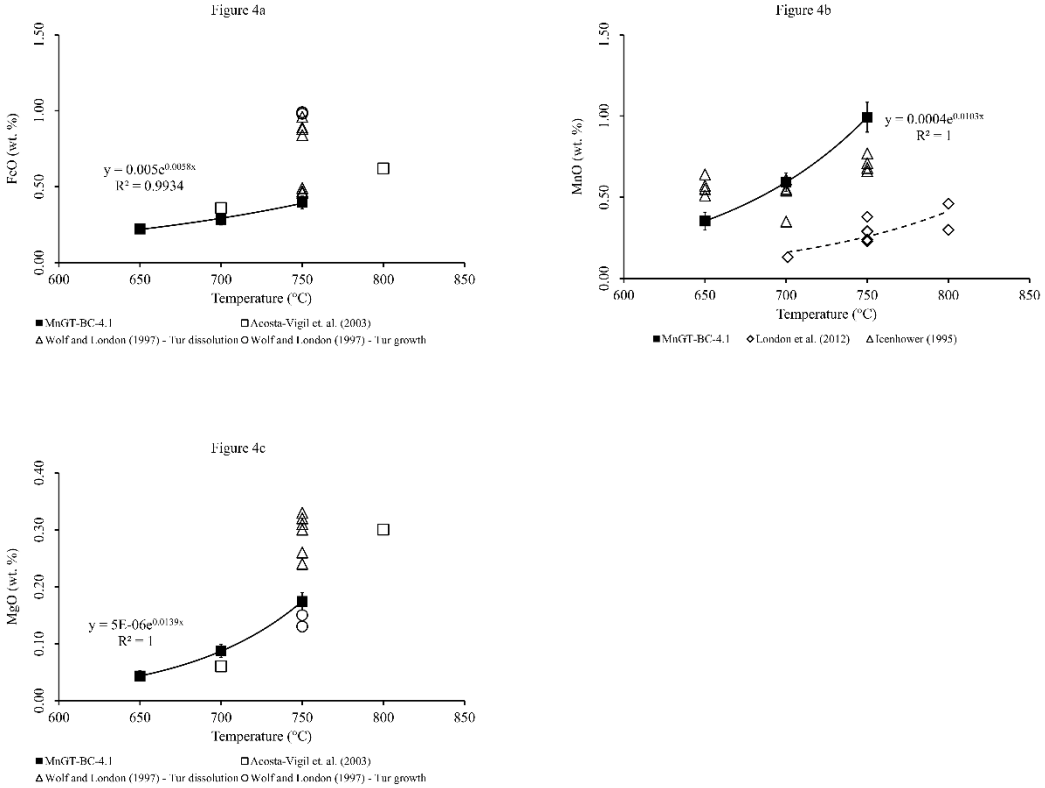

Figure 5-4 (a) Solubility of FeO in melt at garnet and tourmaline (MnGT-BC-4.1: solid squares). Open circles and open diamonds are data from Wolf and London (1997) for tourmaline growth and dissolution, respectively, from/into granitic melt. Open squares are from Acosta-Vigil et al. (2003) for tourmaline dissolution in granitic melt. Note the higher solubility of FeO in melt reported by Wolf and London (1997) for some of their experiments. The experiments reported by Wolf and London (1997) were conducted for a similar duration as those reported in this manuscript. We offer no explanation for the departure of their data from that reported in this manuscript. Error bars represent 2σ standard deviations. (b) Solubility of MnO in melt at garnet and tourmaline (from 650°C to 750°C). Data shown are from long-duration (720 hrs) experiments in which steady-state conditions have been validated via a time-series of experiments. Error bars represent 2σ standard deviations. Data from F-rich (~ 1wt.% F) experiments of Icenhower (1995) and from B- and F-free, hydrous (~ 5-7% H_2O) experiments of London et al. (2012) are shown for comparison. The garnet saturation surface for B- and F-free, hydrous granitic melt (e.g. London et al. 2012) is lower than the B- and/or F-rich saturation surface. (c) Solubility of MgO in melt at garnet and tourmaline (MnGT-BC-4.1: solid squares) saturation. Open circles and open diamonds are data from Wolf and London (1997) for tourmaline growth and dissolution, respectively, from/into granitic melt. Open squares are from Acosta-Vigil et al. (2003) for tourmaline dissolution in granitic melt. Note the higher solubility of FeO in melt reported by Wolf and London (1997) for some of their experiments. The experiments reported by Wolf and London (1997) were conducted for a similar duration as those reported in this manuscript. We offer no explanation for the departure of their data from that reported in this manuscript. Error bars represent 2σ standard deviations.

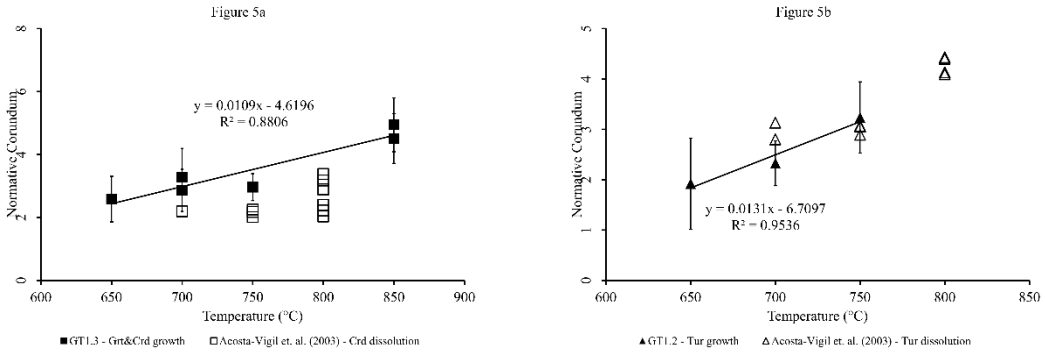

Figure 5-5 (a) Normative corundum component of boron-bearing, peraluminous, hydrous granitic glasses (melts) that produced garnet and cordierite crystals (solid squares). Data from Acosta-Vigil et al. (2003) for dissolution of cordierite into boron-free, hydrous granitic glass (open squares). Errors for solid squares are 2σ standard deviations. Errors for open squares are similar to the size of the symbol. Note the lower normative corundum for cordierite dissolution into B-free granitic melt compared with the data for B-bearing granitic melt. (b) Normative corundum component of boron-bearing, peraluminous, hydrous granitic glasses (melts) that produced tourmaline crystals (solid triangles). Data from Acosta-Vigil et al. (2003) for dissolution of cordierite into boron-free, hydrous granitic glass (open triangles). Errors for solid squares are 2σ standard deviations. Errors for open squares are similar to the size of the symbol.

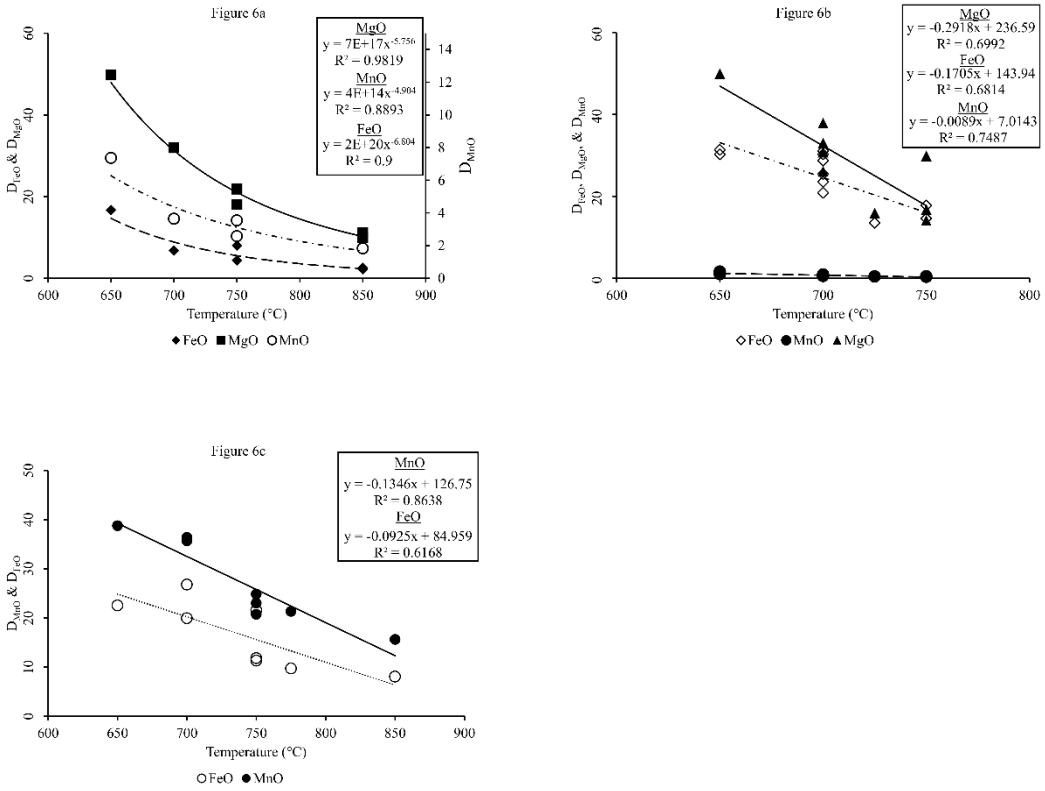

Figure 5-6 (a) Crd-melt partition coefficients, D_M, plotted against temperature. Individual points represent average values from individual experiments. (b) Tur-melt partition coefficients, D_M, plotted against temperature. Individual points represent average values of multiple experiments conducted at a given temperature. D values increase with decreasing temperature. (c) Grt-melt partition coefficients, D_M, plotted against temperature. Individual points represent average values of multiple experiments conducted at a given temperature. D values increase with decreasing temperature, except for MgO (not shown in figure).

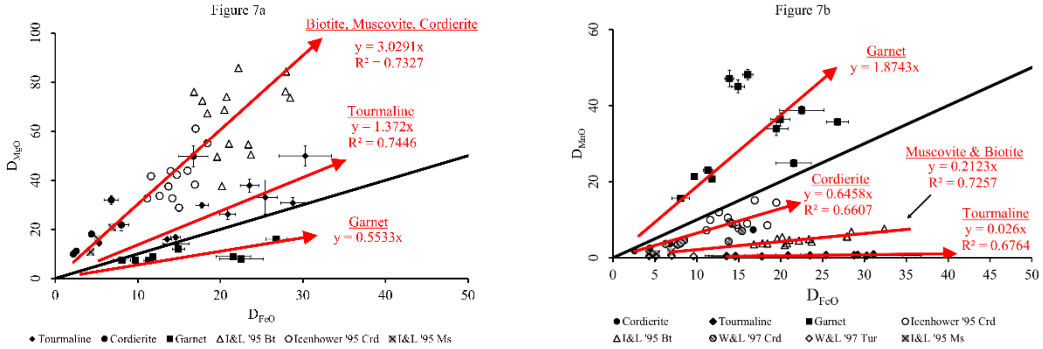

Figure 5-7 (a) Mineral-melt exchange coefficients, $K_{DMgO/FeO}$, calculated as the slope of a linear regression through the D_{FeO} and D_{MgO} data for garnet-, tourmaline-, cordierite-, muscovite-, and biotite-melt. Solid symbols represent data described in from this manuscript. Open symbols represent data from Icenhower and London (1995) and Icenhower (1995). The solid black line without an arrow represents a one-to-one correlation of D_{FeO} and D_{MgO}. The slope of each linear regression (red lines with arrows) represents an exchange coefficient for each mineral, $K_{DMgO/FeO}$. Arrows point in the direction of decreasing temperature. Exchange coefficients for tourmaline-melt (diamonds), cordierite-melt (solid and open circles), and biotite-melt (open triangles) indicate that crystallization of these three minerals will consume MgO from melt at a faster rate than FeO thereby decreasing the MgO/FeO ratio of the residual melt. On the contrary, crystallization of garnet will result in an increase of the MgO/FeO ratio of melt. Note that the exchange coefficient for biotite is identical, within statistical certainty, to that of cordierite. Individual points represent average values calculated per individual experiment. Error bars show 2σ standard errors of the mean, which were propagated through the calculation of partition coefficients. (b) Mineral-melt exchange coefficients, $K_{DMnO/FeO}$, calculated as the slope of a linear regression through the D_{FeO} and D_{MnO} data for garnet-, tourmaline-, cordierite-, muscovite-, and biotite-melt. Solid symbols represent data presented in this manuscript. Open symbols represent data from Icenhower and London (1995) and Icenhower (1995). The solid black line without an arrow represents a one-to-one correlation of D_{FeO} and D_{MnO}. The slope of each linear regression (red lines with arrows) represents an exchange coefficient for each mineral, $K_{DMnO/FeO}$. Arrows point in the direction of decreasing temperature. Exchange coefficients for tourmaline-melt (diamonds), cordierite-melt (solid and open circles), and biotite-melt (open triangles) indicate that crystallization of these three minerals will consume FeO from melt at a faster rate than MnO resulting in an increase of the MnO/FeO ratio of melt. Crystallization of garnet alone will result in a decrease of the MnO/FeO ratio of melt. Individual points represent average values calculated per individual experiment. Error bars show 2σ standard errors of the mean, which were propagated through the calculation of partition coefficients.

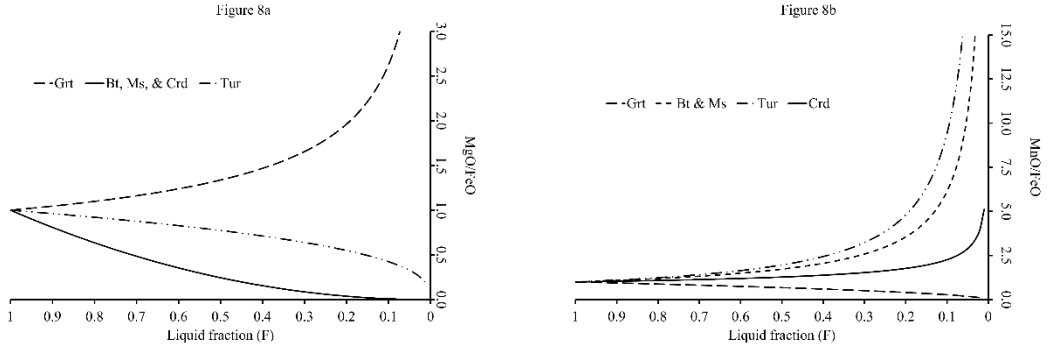

Figure 5-8 (a) Evolution of the MgO/FeO ratio of granitic melt resulting from fractional crystallization involving garnet, biotite, tourmaline, and cordierite individually. F=1 represent 100% melt (liquid) and F=0 represents complete crystallization. The vertical axis represents values of C/C_o. Values of C/C_o that are greater than one or less than one indicate MgO enrichment or depletion relative to FeO, respectively. Crystallization of garnet alone produces an increase in the MgO/FeO ratio (at 200 MPa). Higher pressures (> 4 kb) may result in a different partitioning behavior. (b) Evolution of the MnO/FeO ratio of granitic melt resulting from fractional crystallization involving garnet, biotite, tourmaline, and cordierite individually. F=1 represent 100% melt and F=0 represents complete crystallization. The vertical axis represents values of C/C_o. Values of C/C_o that are greater than one or less than one indicate MnO enrichment or depletion relative to FeO, respectively. Crystallization of garnet alone results in a decrease of MnO/FeO in melt, whereas, for all other minerals presented, the MnO/FeO ratio of melt increases.

Figure 9

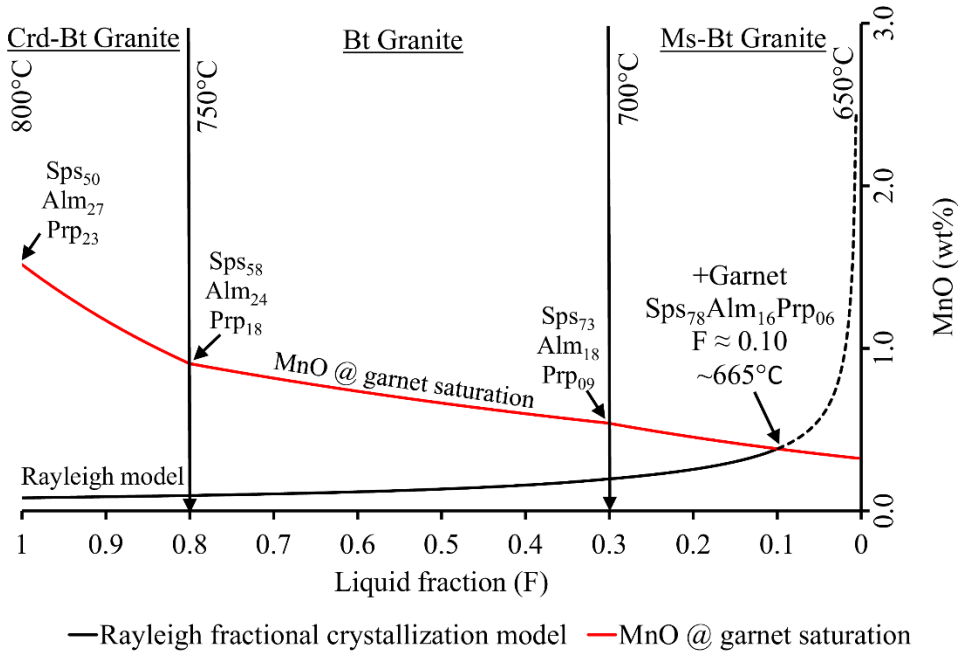

Figure 5-9 Rayleigh fractional crystallization model for a parental, S-type granite liquid. The black line represents results of Rayleigh model and the red line denotes the MnO saturation surface for garnet in B-bearing, hydrous granitic melt. The model entails crystallization of a cordierite-biotite granite between F=1.0 and F=0.8, a biotite granite between F=0.8 and F=0.3, and a muscovite-biotite granite between F=0.3 and 0.0. The inflection of the red line at F=0.8 and F=0.3 is caused by a change in the slope of T/F (temperature/liquid fraction) at those points. Parameters for the Rayleigh model are reported in Table 7 (Appendix 2).

Table 5-1 Compositions of Starting Materials

Mineral	Orthoclase	Albite	Forsterite	Mn-Fayalite	Rhodonite	Spessartine	Almandine	HG Glass
SiO_2	64.96	68.83	40.80	30.01	47.10	35.59	36.09	77.51
Al_2O_3	18.52	19.76	0.01	0.01	0.01	20.43	20.73	12.87
Fe_2O_3	ND	ND	ND	ND	ND	ND	ND	ND
FeO*	0.01	0.01	9.08	62.64	4.01	2.35	19.83	ND
MnO	ND	ND	0.12	5.60	40.96	41.67	23.16	ND
MgO	ND	ND	50.17	1.12	1.91	0.00	0.05	ND
CaO	0.00	0.07	0.07	0.05	5.41	0.14	0.33	0.01
Na_2O	0.85	11.59	ND	0.00	0.00	ND	ND	4.54
K_2O	15.35	0.24	ND	0.00	ND	ND	ND	4.77
F	ND	ND	ND	ND	ND	ND	ND	ND
O=F	ND	ND	ND	ND	ND	ND	ND	ND
Total	99.72	100.82	100.67	99.65	99.41	100.18	100.19	99.70
N	60	5	45	15	25	20	20	267

Orthoclase: Little Three pegmatite mine, Ramona, CA

Albite: Copelinha, Brazil

Forsterite: San Carlos, AZ

Mn-Fayalite: Sardinia, Italy

Rhodonite: Brazil

Spessartine: Little Three pegmatite mine, Ramona, CA

Almandine: location unknown, University of Oklahoma mineral collection

HG Glass: composition matches the thermal minimum in the haplogranite system at 200 MPa_{H2O}

Table 5-2 Garnet (Grt) compositions

	GT 1.3									
	GBT-90		GBT-88		GBT-89		GBT-101		GBT-103	
T (°C)	850		850/750		750		850/750		850/650	
t (hrs)	45		24/168		168		42/456		42/456	
Location of Analysis	Rim		Rim		Rim		Rim		Rim	
	Weight Percent Oxides									
SiO_2	36.00	(0.26)	35.80	(0.53)	34.76	(0.27)	35.33	(0.28)	33.75	(0.54)
TiO_2	0.98	(0.11)	1.11	(0.14)	1.27	(0.29)	1.19	(0.07)	0.95	(0.30)
Al_2O_3	20.37	(0.30)	20.26	(0.17)	19.25	(0.68)	19.28	(0.23)	19.20	(0.20)
FeO*	10.62	(1.02)	12.38	(0.18)	10.05	(0.53)	10.56	(0.70)	6.78	(0.63)
MnO	22.68	(0.67)	25.42	(0.51)	30.39	(0.89)	28.89	(1.30)	36.23	(0.57)
MgO	6.61	(0.56)	4.46	(0.31)	2.80	(0.26)	3.64	(0.45)	0.99	(0.07)
CaO	0.18	(0.01)	0.17	(0.02)	0.35	(0.04)	0.19	(0.02)	0.36	(0.04)
Na_2O	0.01	0.00	0.01	(0.01)	0.02	(0.04)	0.01	(0.01)	0.01	(0.01)
K_2O	0.04	(0.01)	0.02	(0.01)	0.05	(0.01)	0.02	(0.01)	0.03	(0.01)
Total	97.58	(0.34)	99.67	(0.59)	98.96	(0.48)	99.12	(0.28)	98.39	(0.39)
# Pts (N)	3		21		18		10		12	
	Atoms per formula unit (based on 12 oxygens)									
Si	2.923	(0.006)	2.905	(0.026)	2.892	(0.019)	2.914	(0.016)	2.868	(0.032)
Ti	0.060	(0.007)	0.068	(0.009)	0.079	(0.018)	0.074	(0.004)	0.060	(0.019)
Al	1.949	(0.020)	1.938	(0.018)	1.887	(0.062)	1.874	(0.022)	1.922	(0.015)
Fe	0.721	(0.071)	0.840	(0.010)	0.699	(0.038)	0.728	(0.047)	0.482	(0.045)
Mn	1.561	(0.054)	1.748	(0.041)	2.142	(0.066)	2.019	(0.096)	2.608	(0.042)
Mg	0.800	(0.063)	0.539	(0.036)	0.347	(0.031)	0.447	(0.055)	0.126	(0.008)
Ca	0.016	(0.001)	0.015	(0.001)	0.032	(0.004)	0.017	(0.002)	0.032	(0.004)
∑ X-site	3.097	(0.029)	3.142	(0.032)	3.219	(0.071)	3.211	(0.017)	3.247	(0.024)
∑Cations	8.030	(0.011)	8.053	(0.020)	8.078	(0.024)	8.073	(0.011)	8.098	(0.009)
	Normative End-Member Components									
%Sps	50.63	(1.65)	55.89	(1.12)	67.17	(0.94)	63.20	(2.86)	81.12	(1.53)
%Alm	23.38	(2.08)	26.86	(0.38)	21.93	(0.98)	22.80	(1.48)	14.98	(1.34)
%Prp	25.99	(2.26)	17.24	(1.13)	10.89	(1.13)	14.00	(1.75)	3.91	(0.26)

2σSD in parentheses

Table 2 cont.: Garnet (Grt) compositions

	MnGT-BC-4.1							
	MnGT-76		MnGT-77		MnGT-56		MnGT-49	
T (°C)	800/775		800/750		800/700		800/700	
t (hrs)	168/24		168/24		336/336		168/264	
Location of Analysis	Rim		Rim		Rim		Rim	
	Weight Percent Oxides							
SiO_2	36.43	(0.18)	36.42	(0.33)	35.63	(0.39)	35.68	(0.24)
TiO_2	ND		ND		ND		0.05	(0.02)
Al_2O_3	20.03	(0.33)	19.55	(0.55)	19.54	(0.59)	19.05	(0.29)
FeO*	8.58	(0.22)	7.14	(0.27)	6.19	(1.34)	9.10	(0.98)
MnO	31.53	(0.58)	33.62	(0.23)	37.09	(2.32)	31.88	(1.30)
MgO	3.20	(0.20)	3.13	(0.16)	1.54	(0.79)	2.37	(0.29)
CaO	0.07	(0.01)	0.07	(0.01)	0.10	(0.01)	0.09	(0.01)
Na_2O	ND		ND		ND		ND	
K_2O	ND		ND		ND		ND	
Total	99.85	(0.46)	99.94	(0.59)	100.09	(0.60)	98.22	(0.30)
# Pts (N)	25		6		13		57	
	Atoms per formula unit (based on 12 oxygens)							
Si	2.974	(0.012)	2.982	(0.008)	2.953	(0.009)	2.987	(0.013)
Ti	ND		ND		ND		0.003	(0.001)
Al	1.927	(0.024)	1.885	(0.035)	1.908	(0.041)	1.880	(0.025)
Fe	0.586	(0.015)	0.489	(0.022)	0.429	(0.090)	0.637	(0.069)
Mn	2.180	(0.043)	2.331	(0.037)	2.604	(0.174)	2.261	(0.095)
Mg	0.389	(0.023)	0.382	(0.016)	0.190	(0.094)	0.295	(0.036)
Ca	0.006	(0.001)	0.006	(0.001)	0.009	(0.001)	0.008	(0.001)
∑ X-site	3.161	(0.021)	3.209	(0.042)	3.232	(0.057)	3.201	(0.033)
∑Cations	8.062	(0.021)	8.076	(0.013)	8.093	(0.019)	8.071	(0.013)
	Normative End-Member Components							
%Sps	69.10	(1.09)	72.80	(0.33)	80.83	(5.70)	70.80	(2.96)
%Alm	18.57	(0.47)	15.26	(0.52)	13.29	(2.81)	19.95	(2.07)
%Prp	12.34	(0.78)	11.93	(0.64)	5.89	(3.01)	9.25	(1.15)

2σSD in parentheses

Table 5-3 Tourmaline (tur) compositions

	MnGT-BC-4.1							
Exp #	MnGT-77		MnGT-78		MnGT-49		MnGT-56	
T (°C)	800/750		800/725		800/700		800/700	
t (hrs)	168/24		168/24		168/264		336/336	
	Weight Percent Oxides							
SiO_2	34.86	(0.60)	33.95	(0.70)	34.69	(0.58)	33.79	(0.83)
TiO_2	0.04	(0.02)	0.04	(0.02)	0.04	(0.02)	0.04	(0.02)
B_2O_3	10.97	(0.38)	11.33	(0.31)	11.11	(0.34)	11.32	(0.37)
Al_2O_3	30.80	(1.94)	28.37	(0.98)	31.26	(1.33)	29.70	(1.47)
FeO*	9.24	(0.99)	10.06	(0.37)	8.00	(0.56)	9.82	(0.77)
MnO	0.67	(0.06)	0.65	(0.06)	0.57	(0.08)	0.92	(0.19)
MgO	6.11	(0.49)	5.87	(0.45)	5.60	(0.41)	6.27	(0.51)
CaO	0.44	(0.07)	0.47	(0.07)	0.45	(0.07)	0.46	(0.11)
Na_2O	2.09	(0.03)	2.19	(0.05)	2.18	(0.08)	2.22	(0.08)
Total	95.22	(1.19)	92.94	(0.94)	93.90	(0.66)	94.54	(0.72)
# Pts (N)	6		15		31		69	
	2σSD in parentheses							
	Atoms per Formula Unit (29 Oxygens)							
Si	5.861	(0.105)	5.867	(0.092)	5.864	(0.122)	5.749	(0.140)
Ti	0.005	(0.002)	0.005	(0.003)	0.005	(0.003)	0.005	(0.002)
B	3.184	(0.097)	3.381	(0.095)	3.240	(0.086)	3.324	(0.111)
Al	6.098	(0.307)	5.778	(0.176)	6.227	(0.234)	5.956	(0.258)
Fe	1.301	(0.151)	1.455	(0.065)	1.130	(0.083)	1.398	(0.118)
Mn	0.095	(0.009)	0.096	(0.008)	0.081	(0.012)	0.133	(0.027)
Mg	1.531	(0.130)	1.511	(0.109)	1.411	(0.110)	1.592	(0.134)
Ca	0.079	(0.013)	0.088	(0.013)	0.081	(0.012)	0.084	(0.020)
Na	0.682	(0.018)	0.735	(0.019)	0.716	(0.028)	0.731	(0.030)
Sum	18.835	(0.065)	18.915	(0.029)	18.755	(0.057)	18.971	(0.071)
$Mg^{\#}$	0.541	(0.031)	0.509	(0.023)	0.555	(0.014)	0.532	(0.025)
	$Mg^{\#}$=Mg/Mg+Fe							
	Normative End-Member Components							
Schorl	25.53		36.81		27.98		28.05	
Dravite	39.59		33.43		34.90		40.80	
Tsilaisite	3.19		3.17		2.72		4.42	
Uvite	0.43		4.10		4.52		4.41	
Feruvite	0.36		4.61		3.62		3.98	
Foitite	14.18		9.46		9.10		8.70	
Mg-Foitite	16.71		8.41		11.35		9.64	
Olenite	0.00		0.00		5.80		0.00	

Table 3 cont.: Tourmaline (tur) compositions

Exp #	MnGT-66		MnGT-67		MnGT-57		MnGT-58	
T (°C)	800/700		800/700		800/600		800/600	
t (hrs)	336/24		336/72		336/336		336/336	
	Weight Percent Oxides							
SiO_2	34.34	(0.62)	34.29	(0.78)	33.35	(1.11)	33.99	(1.88)
TiO_2	0.04	(0.02)	0.04	(0.02)	0.03	(0.01)	0.04	(0.02)
B_2O_3	11.24	(0.30)	11.50	(0.39)	11.71	(0.58)	11.38	(0.41)
Al_2O_3	29.73	(1.48)	29.71	(1.20)	30.22	(2.50)	30.18	(1.65)
FeO*	9.13	(0.37)	9.36	(0.72)	9.84	(0.97)	9.25	(0.76)
MnO	1.02	(0.15)	0.98	(0.17)	2.17	(0.62)	0.86	(0.13)
MgO	6.48	(0.52)	6.50	(0.45)	6.08	(0.76)	6.04	(0.62)
CaO	0.41	(0.07)	0.42	(0.09)	0.35	(0.05)	0.48	(0.08)
Na_2O	2.25	(0.07)	2.21	(0.06)	2.31	(0.20)	2.17	(0.10)
Total	94.66	(0.73)	95.03	(0.55)	96.06	(0.54)	94.40	(1.05)
N	19		25		10		85	
	2σSD in parentheses							
	Atoms per Formula Unit (29 Oxygens)							
Si	5.818	(0.101)	5.785	(0.122)	5.617	(0.225)	5.765	(0.285)
Ti	0.005	(0.002)	0.005	(0.003)	0.004	(0.002)	0.006	(0.002)
B	3.287	(0.096)	3.349	(0.113)	3.403	(0.147)	3.332	(0.128)
Al	5.933	(0.258)	5.908	(0.226)	5.993	(0.448)	6.034	(0.299)
Fe	1.294	(0.061)	1.321	(0.108)	1.386	(0.142)	1.313	(0.120)
Mn	0.146	(0.021)	0.140	(0.023)	0.311	(0.091)	0.124	(0.018)
Mg	1.638	(0.141)	1.635	(0.112)	1.529	(0.204)	1.528	(0.161)
Ca	0.075	(0.013)	0.076	(0.016)	0.064	(0.009)	0.088	(0.015)
Na	0.740	(0.025)	0.723	(0.021)	0.754	(0.072)	0.713	(0.037)
Sum	18.937	(0.064)	18.943	(0.056)	19.059	(0.103)	18.903	(0.174)
$Mg^{\#}$	0.558	(0.015)	0.553	(0.024)	0.523	(0.037)	0.537	(0.024)
	$Mg^{\#}$=Mg/Mg+Fe							
	Normative End-Member Components							
Schorl	27.44		27.44		23.96		28.18	
Dravite	41.61		40.21		41.16		39.10	
Tsilaisite	4.88		4.67		10.32		4.12	
Uvite	4.09		4.10		3.31		4.69	
Feruvite	3.36		3.50		3.01		4.03	
Foitite	8.40		9.25		8.69		9.18	
Mg-Foitite	10.22		10.82		9.56		10.68	
Olenite	0.00		0.00		0.00		0.00	

Table 3 cont.: Tourmaline (tur) compositions

	GT 1.2				GT 1.2+			
Exp #	GBT-79		GBT-83		GBT-98		GBT-99	
T (°C)	850/750		750/700		850/750		850/700	
t (hrs)	24/168		24/168		42/456		48/336	
	Weight Percent Oxides							
SiO_2	35.10	(0.79)	34.79	(0.94)	35.47	(0.86)	34.54	(1.27)
TiO_2	0.01	(0.02)	0.01	(0.02)	0.01	(0.01)	0.01	(0.02)
B_2O_3	11.21	(0.46)	11.15	(0.64)	11.07	(0.44)	11.17	(0.78)
Al_2O_3	29.84	(2.70)	30.08	(2.67)	31.36	(1.72)	30.49	(2.67)
FeO*	8.49	(1.30)	8.35	(1.39)	7.58	(1.16)	8.85	(1.35)
MnO	0.43	(0.13)	0.71	(0.18)	0.63	(0.38)	0.80	(0.21)
MgO	7.82	(1.03)	7.84	(1.01)	7.47	(0.72)	7.29	(0.99)
CaO	0.03	(0.02)	0.03	(0.02)	0.03	(0.02)	0.03	(0.02)
Na_2O	2.58	(0.10)	2.62	(0.13)	2.44	(0.17)	2.49	(0.19)
Total	95.49	(1.21)	95.59	(1.03)	96.06	(1.17)	95.67	(0.72)
N	36		35		34		41	
	2σSD in parentheses							
	Atoms per Formula Unit (29 Oxygens)							
Si	5.863	(0.155)	5.816	(0.193)	5.863	(0.159)	5.779	(0.236)
Ti	0.001	(0.003)	0.001	(0.002)	0.001	(0.002)	0.001	(0.003)
B	3.232	(0.108)	3.218	(0.149)	3.159	(0.101)	3.227	(0.209)
Al	5.872	(0.466)	5.924	(0.445)	6.108	(0.301)	6.012	(0.476)
Fe	1.186	(0.196)	1.168	(0.211)	1.047	(0.165)	1.240	(0.201)
Mn	0.060	(0.019)	0.101	(0.027)	0.089	(0.054)	0.114	(0.030)
Mg	1.947	(0.269)	1.953	(0.270)	1.841	(0.174)	1.819	(0.259)
Ca	0.005	(0.003)	0.006	(0.004)	0.005	(0.004)	0.005	(0.003)
Na	0.835	(0.033)	0.850	(0.053)	0.783	(0.053)	0.807	(0.068)
Sum	19.001	(0.100)	19.037	(0.130)	18.895	(0.105)	19.004	(0.149)
$Mg^{\#}$	0.622	(0.044)	0.626	(0.042)	0.638	(0.041)	0.595	(0.034)
	$Mg^{\#}$=Mg/Mg+Fe							
	Normative End-Member Components							
Schorl	27.57		25.20		23.30		24.13	
Dravite	53.96		56.38		51.97		52.88	
Tsilaisite	2.03		3.35		2.94		3.78	
Uvite	0.33		0.33		0.34		0.32	
Feruvite	0.21		0.21		0.19		0.22	
Foitite	6.27		5.57		7.72		7.56	
Mg-Foitite	9.63		8.97		13.55		11.10	
Olenite	0.00		0.00		0.00		0.00	

Table 3 cont.: Tourmaline (tur) compositions

	GT 1.3			
Exp #	GBT-85		GBT-103	
T (°C)	850/650		850/650	
t (hrs)	24/168		42/456	
	Weight Percent Oxides			
SiO_2	34.02	(2.14)	34.77	(1.04)
TiO_2	0.01	(0.01)	0.45	(0.22)
B_2O_3	11.78	(0.97)	10.81	(0.57)
Al_2O_3	32.16	(3.75)	29.87	(2.18)
FeO*	5.97	(1.61)	9.11	(1.09)
MnO	1.49	(0.81)	1.51	(0.25)
MgO	7.25	(1.13)	6.25	(0.87)
CaO	0.03	(0.02)	0.79	(0.29)
Na_2O	2.42	(0.29)	2.08	(0.21)
Total	95.12	(0.86)	95.64	(1.08)
N	15		14	
	2σSD in parentheses			
	Atoms per Formula Unit (29 Oxygens)			
Si	5.643	(0.393)	5.859	(0.160)
Ti	0.001	(0.002)	0.057	(0.029)
B	3.373	(0.235)	3.145	(0.138)
Al	6.286	(0.662)	5.933	(0.442)
Fe	0.828	(0.231)	1.284	(0.153)
Mn	0.209	(0.116)	0.216	(0.035)
Mg	1.793	(0.293)	1.569	(0.216)
Ca	0.005	(0.004)	0.143	(0.053)
Na	0.777	(0.101)	0.678	(0.069)
Sum	18.915	(0.131)	18.884	(0.105)
$Mg^{\#}$	0.685	(0.063)	0.550	(0.027)
	$Mg^{\#}$=Mg/Mg+Fe			
	Normative End-Member Components			
Schorl	21.34		24.03	
Dravite	49.51		36.99	
Tsilaisite	6.98		7.21	
Uvite	0.36		7.78	
Feruvite	0.17		6.54	
Foitite	6.84		7.97	
Mg-Foitite	14.80		9.47	
Olenite	0.00		0.00	

Table 5-4 Cordierite (Crd) compositions

	GT 1.3															
Exp #	GBT-90		GBT-101		GBT-101		GBT-88		GBT-102		GBT-102		GBT-103		GBT-103	
T (°C)	850		850/750		850/750		850/750		850/700		850/700		850/650		850/650	
t (hrs)	48		42/456		42/456		24/168		48/336		48/336		42/456		42/456	
Location of analysis			Core		Rim		Rim		Core		Rim		Core		Rim	
	Weight Percent Oxides															
SiO2	46.56	(0.58)	47.73	(0.77)	47.35	(0.34)	47.28	(0.41)	47.35	(0.44)	47.48	(0.36)	46.81	(0.68)	45.79	(0.68)
Al2O3	32.79	(0.39)	32.64	(0.23)	32.30	(0.24)	32.82	(0.26)	32.84	(0.15)	32.14	(0.35)	33.02	(0.44)	32.00	(0.25)
FeO*	3.35	(0.31)	3.19	(0.44)	3.92	(0.38)	4.59	(0.09)	3.12	(0.22)	3.09	(0.16)	3.58	(0.32)	5.03	(0.29)
MnO	2.66	(0.36)	2.73	(0.46)	4.12	(0.25)	3.15	(0.19)	2.42	(0.27)	4.26	(0.67)	2.67	(0.16)	6.89	(0.98)
MgO	9.89	(0.45)	10.30	(0.60)	8.91	(0.10)	9.22	(0.18)	10.50	(0.31)	9.24	(0.38)	9.95	(0.30)	6.23	(0.50)
CaO	0.09	(0.03)	0.05	(0.02)	0.03	(0.02)	0.05	(0.02)	0.05	(0.02)	0.04	(0.02)	0.07	(0.02)	0.07	(0.03)
Na2O	0.25	(0.06)	0.21	(0.07)	0.15	(0.03)	0.18	(0.06)	0.26	(0.07)	0.18	(0.06)	0.33	(0.03)	0.40	(0.16)
K2O	0.19	(0.05)	0.07	(0.02)	0.06	(0.01)	0.08	(0.02)	0.10	(0.05)	0.05	(0.02)	0.13	(0.03)	0.07	(0.03)
Total	95.83	(0.39)	96.94	(0.89)	96.86	(0.55)	97.43	(0.49)	96.69	(0.32)	96.51	(0.51)	96.59	(0.50)	96.50	(0.34)
# Pts (N)	14		10		10		20		10		10		15		15	

2σSD in parentheses

Table 4 cont.: Cordierite (Crd) compositions

Atoms per formula unit (18 oxygen basis)															
Si	4.889	(0.045)	4.942	(0.033)	4.953	(0.023)	4.914	(0.028)	4.912	(0.023)	4.968	(0.034)	4.882	(0.045)	4.906	(0.045)
Al	4.058	(0.053)	3.983	(0.028)	3.982	(0.026)	4.020	(0.027)	4.016	(0.023)	3.964	(0.036)	4.058	(0.065)	4.041	(0.045)
Fe	0.295	(0.028)	0.277	(0.039)	0.343	(0.033)	0.399	(0.008)	0.271	(0.020)	0.270	(0.014)	0.312	(0.029)	0.451	(0.026)
Mn	0.236	(0.032)	0.239	(0.042)	0.365	(0.022)	0.278	(0.018)	0.213	(0.024)	0.377	(0.059)	0.236	(0.015)	0.625	(0.091)
Mg	1.548	(0.064)	1.590	(0.085)	1.389	(0.015)	1.428	(0.027)	1.624	(0.041)	1.441	(0.057)	1.546	(0.040)	0.994	(0.075)
Ca	0.010	(0.003)	0.005	(0.002)	0.004	(0.002)	0.005	(0.002)	0.006	(0.002)	0.005	(0.002)	0.008	(0.002)	0.008	(0.004)
Na	0.051	(0.012)	0.042	(0.013)	0.030	(0.006)	0.036	(0.012)	0.053	(0.014)	0.036	(0.012)	0.067	(0.006)	0.084	(0.034)
K	0.025	(0.006)	0.009	(0.002)	0.007	(0.002)	0.010	(0.003)	0.013	(0.007)	0.007	(0.003)	0.017	(0.004)	0.009	(0.004)
∑Cations	11.116	(0.029)	11.090	(0.025)	11.074	(0.013)	11.095	(0.017)	11.110	(0.022)	11.070	(0.017)	11.129	(0.015)	11.119	(0.041)
∑M site	2.079	(0.021)	2.106	(0.025)	2.097	(0.010)	2.105	(0.022)	2.107	(0.011)	2.088	(0.024)	2.094	(0.018)	2.070	(0.012)
Normative End-Member Components															
% Crd	83.99	(1.76)	85.13	(2.43)	80.22	(1.65)	78.14	(0.46)	85.71	(1.18)	84.19	(0.68)	83.20	(1.58)	68.73	(1.79)
% Sek	16.01	(1.76)	14.87	(2.43)	19.78	(1.65)	21.86	(0.46)	14.29	(1.18)	15.81	(0.68)	16.80	(1.58)	31.27	(1.79)

Crd: $Mg_2Al_4Si_5O_{18}$ (cordierite)
Sek: $Fe_2Al_4Si_5O_{18}$ (sekaninaite)

Table 5-5 EMPA Summary of Glasses

	GT1.2									
Exp#	GBT77		GBT78		GBT79		GBT83		GBT82	
T (°C)	850		850		850/750		750/700		850/650	
t (hrs)	24		24		24/168		24/168		24/168	
Direction	F		F		F		F		F	
	F: Forward thermal direction; R: reverse thermal direction									
	Weight Percent Oxides									
SiO_2	62.60	(1.69)	63.35	(1.54)	64.59	(0.67)	65.14	(0.66)	66.23	(0.47)
TiO_2	ND		ND		ND		ND		ND	
B_2O_3	7.92	(0.82)	7.96	(0.43)	7.87	(0.49)	6.05	(0.24)	5.96	(0.36)
Al_2O_3	12.69	(0.46)	12.67	(0.67)	12.05	(0.40)	11.66	(0.27)	11.20	(0.37)
FeO*	1.45	(0.39)	1.01	(0.07)	0.58	(0.03)	0.29	(0.02)	0.24	(0.04)
MnO	1.43	(0.24)	1.33	(0.17)	1.12	(0.07)	1.04	(0.09)	0.78	(0.05)
MgO	0.97	(0.10)	1.07	(0.12)	0.47	(0.04)	0.25	(0.03)	0.12	(0.04)
CaO	0.01	(0.02)	0.01	(0.01)	0.01	(0.02)	0.01	(0.02)	0.01	(0.01)
Na_2O	3.14	(0.13)	3.13	(0.17)	3.26	(0.11)	3.24	(0.11)	3.27	(0.13)
K_2O	3.18	(0.13)	3.30	(0.13)	3.37	(0.10)	3.87	(0.09)	3.74	(0.11)
F	ND		ND		ND		ND		ND	
O=F										
Total	93.39	(0.78)	93.82	(0.73)	93.32	(0.49)	91.55	(0.54)	91.55	(0.35)
H_2O	6.61	(0.78)	6.18	(0.73)	6.68	(0.49)	8.45	(0.54)	8.45	(0.35)
Femic	3.85	(0.50)	3.41	(0.33)	2.17	(0.13)	1.59	(0.10)	1.14	(0.10)
N	25		25		20		12		12	
	2σSD in parentheses									
	CIPW Normative Mineralogy									
Qz	33.06		33.70		35.78		35.08		37.21	
Or	22.00		22.69		23.30		26.72		25.80	
Ab	31.07		30.83		32.27		32.01		32.32	
An	0.07		0.06		0.06		0.07		0.06	
Crn	4.74		4.58		3.53		2.49		2.05	
En	2.83		3.10		1.36		0.74		0.36	
Fs	6.23		5.04		3.70		2.89		2.20	
	Mineral symbols after Whitney and Evans (2010)									
	Atoms per 8 Oxygens									
Si	2.828	(0.065)	2.841	(0.055)	2.898	(0.025)	3.000	(0.023)	3.040	(0.015)
Ti	ND		ND		ND		ND		ND	
B	0.617	(0.065)	0.616	(0.034)	0.609	(0.036)	0.481	(0.018)	0.472	(0.028)
Al	0.676	(0.026)	0.670	(0.038)	0.637	(0.023)	0.633	(0.015)	0.606	(0.020)
Fe	0.055	(0.015)	0.038	(0.003)	0.022	(0.001)	0.011	(0.001)	0.009	(0.001)
Mn	0.055	(0.009)	0.051	(0.007)	0.043	(0.003)	0.041	(0.003)	0.030	(0.002)
Mg	0.066	(0.007)	0.071	(0.008)	0.031	(0.003)	0.018	(0.002)	0.008	(0.003)
Ca	0.001	(0.001)	0.001	(0.001)	0.001	(0.001)	0.001	(0.001)	0.000	(0.001)
Na	0.275	(0.012)	0.272	(0.015)	0.284	(0.011)	0.289	(0.010)	0.291	(0.012)
K	0.183	(0.007)	0.189	(0.007)	0.193	(0.006)	0.227	(0.006)	0.219	(0.006)
F	ND		ND		ND		ND		ND	
Sum	4.755	(0.033)	4.747	(0.032)	4.717	(0.016)	4.701	(0.016)	4.676	(0.012)
ASI	1.471	(0.062)	1.450	(0.062)	1.335	(0.040)	1.224	(0.024)	1.187	(0.048)
$K^{\#}$	0.400	(0.010)	0.410	(0.013)	0.405	(0.008)	0.440	(0.010)	0.429	(0.009)
Mn*	50.306	(6.819)	56.951	(2.585)	66.139	(0.834)	78.330	(2.072)	76.730	(2.583)
$Mg^{\#}$	0.550	(0.066)	0.652	(0.019)	0.587	(0.016)	0.609	(0.033)	0.472	(0.044)
	ASI=aluminum saturation index (molar: Al/Na+K)						Mn^{*}=Mn/(Mn+Fe+Mg)*100			
	$K^{\#}$=K/K+Na						$Mg^{\#}$=Mg/(Mg+Fe)			

Table 5 cont.: EMPA Summary of Glasses

	GT1.2+									
Exp#	GBT81		GBT80		GBT97		GBT98		GBT99	
T (°C)	850/600		850/550		850		850/750		850/700	
t (hrs)	24/168		24/336		48		42/456		48/336	
Direction	F		F		F		F		F	
	F: Forward thermal direction; R: reverse thermal direction									
	Weight Percent Oxides									
SiO_2	66.11	(1.63)	65.95	(1.25)	64.73	(1.79)	66.94	(0.97)	67.00	(0.73)
TiO_2	ND		ND		ND		ND		MD	
B_2O_3	6.21	(0.53)	6.92	(0.44)	6.45	(0.38)	6.43	(0.26)	6.04	(0.30)
Al_2O_3	10.78	(0.74)	10.92	(0.82)	12.40	(0.64)	11.32	(0.22)	10.88	(0.36)
FeO*	0.19	(0.03)	0.11	(0.02)	1.27	(0.17)	0.43	(0.02)	0.29	(0.02)
MnO	0.78	(0.10)	0.34	(0.04)	1.62	(0.21)	1.75	(0.06)	1.40	(0.11)
MgO	0.08	(0.01)	0.03	(0.01)	0.93	(0.10)	0.25	(0.01)	0.13	(0.01)
CaO	0.01	(0.01)	0.01	(0.01)	0.02	(0.02)	0.01	(0.02)	0.01	(0.02)
Na_2O	3.27	(0.25)	3.48	(0.28)	2.69	(0.13)	2.91	(0.08)	2.93	(0.13)
K_2O	3.71	(0.23)	3.96	(0.25)	3.11	(0.09)	3.56	(0.13)	3.56	(0.09)
F	ND		ND		ND		ND		MD	
O=F										
Total	91.13	(0.42)	91.73	(0.89)	93.22	(1.04)	93.60	(0.84)	92.27	(0.44)
H_2O	8.87	(0.42)	8.27	(0.89)	6.78	(1.04)	6.40	(0.84)	7.73	(0.44)
Femic	1.04	(0.11)	0.48	(0.05)	3.81	(0.46)	2.42	(0.07)	1.83	(0.12)
N	12		12		20		20		20	
	2σSD in parentheses									
	CIPW Normative Mineralogy									
Qz	37.62		35.50		38.42		39.15		40.17	
Or	25.81		27.61		21.15		24.14		24.41	
Ab	32.58		34.71		26.23		28.26		28.79	
An	0.04		0.05		0.11		0.07		0.08	
Crn	1.62		1.06		5.27		3.05		2.52	
En	0.22		0.09		2.67		0.71		0.39	
Fs	2.11		0.99		6.15		4.62		3.65	
	Mineral symbols after Whitney and Evans (2010)									
	Atoms per 8 Oxygens									
Si	3.042	(0.068)	3.007	(0.063)	2.933	(0.058)	3.011	(0.019)	3.051	(0.030)
Ti	ND		ND		ND		ND		MD	
B	0.493	(0.042)	0.545	(0.033)	0.505	(0.031)	0.499	(0.019)	0.475	(0.023)
Al	0.585	(0.041)	0.587	(0.042)	0.662	(0.037)	0.600	(0.015)	0.584	(0.019)
Fe	0.007	(0.001)	0.004	(0.001)	0.048	(0.006)	0.016	(0.001)	0.011	(0.001)
Mn	0.030	(0.004)	0.013	(0.002)	0.062	(0.008)	0.067	(0.003)	0.054	(0.004)
Mg	0.005	(0.001)	0.002	(0.001)	0.063	(0.007)	0.017	(0.001)	0.009	(0.001)
Ca	0.000	(0.001)	0.000	(0.000)	0.001	(0.001)	0.001	(0.001)	0.001	(0.001)
Na	0.292	(0.023)	0.307	(0.023)	0.236	(0.012)	0.254	(0.007)	0.259	(0.011)
K	0.218	(0.014)	0.230	(0.013)	0.180	(0.004)	0.204	(0.008)	0.207	(0.005)
F	ND		ND		ND		ND		MD	
Sum	4.673	(0.046)	4.696	(0.044)	4.691	(0.030)	4.669	(0.012)	4.652	(0.018)
ASI	1.146	(0.019)	1.089	(0.025)	1.586	(0.081)	1.307	(0.028)	1.250	(0.038)
$K^{\#}$	0.428	(0.010)	0.429	(0.011)	0.432	(0.013)	0.446	(0.012)	0.449	(0.026)
Mn*	80.610	(3.470)	75.786	(4.235)	56.450	(1.306)	80.552	(1.105)	82.870	(1.557)
$Mg^{\#}$	0.419	(0.047)	0.331	(0.051)	0.567	(0.020)	0.511	(0.012)	0.449	(0.026)
	ASI=aluminum saturation index (molar: Al/Na+K)						Mn^{*}=Mn/(Mn+Fe+Mg)*100			
	$K^{\#}$=K/K+Na						$Mg^{\#}$=Mg/(Mg+Fe)			

Table 5 cont.: EMPA Summary of Glasses

	GT1.3									
Exp#	GBT85		GBT86		GBT90		GBT88		GBT101	
T (°C)	850/650		850		850		850/750		850/750	
t (hrs)	24/168		24		45		24/168		42/456	
Direction	F		F		F		F		F	
F: Forward thermal direction; R: reverse thermal direction										
Weight Percent Oxides										
SiO_2	65.12	(0.88)	68.47	(1.17)	68.85	(0.74)	68.32	(0.77)	69.36	(0.55)
TiO_2	ND		ND		ND		ND		ND	
B_2O_3	6.09	(0.27)	3.09	(0.34)	3.81	(0.27)	3.50	(0.35)	5.10	(0.32)
Al_2O_3	11.44	(0.50)	11.18	(0.36)	10.74	(0.27)	10.93	(0.36)	10.51	(0.20)
FeO*	0.19	(0.04)	1.39	(0.09)	1.32	(0.07)	1.05	(0.05)	0.49	(0.07)
MnO	1.47	(0.16)	1.52	(0.11)	1.45	(0.08)	1.23	(0.06)	1.16	(0.04)
MgO	0.10	(0.01)	1.00	(0.07)	0.89	(0.04)	0.51	(0.02)	0.41	(0.07)
CaO	0.02	(0.02)	0.22	(0.05)	0.22	(0.04)	0.23	(0.05)	0.28	(0.04)
Na_2O	3.04	(0.16)	1.83	(0.08)	1.84	(0.08)	1.96	(0.08)	2.06	(0.12)
K_2O	3.84	(0.15)	3.01	(0.11)	2.93	(0.11)	3.27	(0.11)	3.56	(0.15)
F	ND		ND		ND		ND		ND	
O=F										
Total	91.32	(0.37)	91.70	(0.58)	92.04	(0.37)	90.99	(0.56)	92.94	(0.88)
H_2O	8.68	(0.37)	8.30	(0.58)	7.96	(0.37)	9.01	(0.56)	7.06	(0.88)
Femic	1.76	(0.17)	3.91	(0.26)	3.66	(0.17)	2.78	(0.13)	2.06	(0.17)
N	10		25		25		20		15	
2σSD in parentheses										
CIPW Normative Mineralogy										
Qz	36.53		47.32		48.53		47.11		46.81	
Or	26.64		20.05		19.63		22.10		23.97	
Ab	30.17		17.44		17.62		18.94		19.85	
An	0.11		1.21		1.21		1.31		1.59	
Crn	2.64		5.11		4.70		4.28		3.13	
En	0.29		2.81		2.51		1.45		1.16	
Fs	3.62		6.07		5.80		4.80		3.48	
Mineral symbols after Whitney and Evans (2010)										
Atoms per 8 Oxygens										
Si	3.008	(0.035)	3.174	(0.039)	3.164	(0.028)	3.179	(0.024)	3.134	(0.017)
Ti	ND		ND		ND		ND		ND	
B	0.486	(0.021)	0.247	(0.028)	0.302	(0.021)	0.281	(0.027)	0.397	(0.023)
Al	0.623	(0.028)	0.611	(0.022)	0.582	(0.016)	0.599	(0.022)	0.560	(0.009)
Fe	0.007	(0.001)	0.054	(0.004)	0.051	(0.003)	0.041	(0.002)	0.018	(0.003)
Mn	0.058	(0.007)	0.060	(0.004)	0.057	(0.003)	0.048	(0.003)	0.044	(0.001)
Mg	0.007	(0.001)	0.069	(0.005)	0.061	(0.003)	0.035	(0.002)	0.027	(0.005)
Ca	0.001	(0.001)	0.011	(0.002)	0.011	(0.002)	0.011	(0.002)	0.014	(0.002)
Na	0.272	(0.014)	0.164	(0.008)	0.164	(0.007)	0.177	(0.008)	0.181	(0.010)
K	0.226	(0.009)	0.178	(0.007)	0.172	(0.006)	0.194	(0.007)	0.205	(0.009)
F	ND		ND		ND		ND		ND	
Sum	4.687	(0.024)	4.568	(0.020)	4.562	(0.013)	4.566	(0.015)	4.581	(0.011)
ASI	1.244	(0.036)	1.683	(0.070)	1.632	(0.070)	1.522	(0.046)	1.356	(0.034)
$K^{\#}$	0.454	(0.016)	0.520	(0.014)	0.546	(0.008)	0.524	(0.013)	0.532	(0.018)
Mn*	88.678	(2.227)	52.531	(0.828)	52.785	(0.765)	54.249	(0.760)	29.255	(2.171)
$Mg^{\#}$	0.486	(0.064)	0.561	(0.009)	0.546	(0.008)	0.465	(0.010)	0.597	(0.013)
ASI=aluminum saturation index (molar: Al/Na+K)							Mn^{*}=Mn/(Mn+Fe+Mg)*100			
$K^{\#}$=K/K+Na							$Mg^{\#}$=Mg/(Mg+Fe)			

Table 5 cont.: EMPA Summary of Glasses

									MnGT-BC-4.1	
Exp#	GBT89		GBT102		GBT104		GBT103		MnGT-80	
T (°C)	750		850/700		850/700		850/650		850	
t (hrs)	168		48/336		48/336		42/456			
Direction	F		F		R		F		F	
	F: Forward thermal direction; R: reverse thermal direction									
	Weight Percent Oxides									
SiO_2	70.58	(0.40)	68.33	(0.96)	66.83	(1.26)	66.09	(1.01)	62.73	(0.78)
TiO_2	ND		ND		ND		ND		ND	
B_2O_3	2.01	(0.26)	5.12	(0.32)	5.47	(0.36)	5.12	(0.25)	8.13	(0.44)
Al_2O_3	11.44	(0.26)	10.65	(0.42)	10.84	(0.36)	11.71	(0.17)	11.68	(0.15)
FeO*	0.67	(0.05)	0.46	(0.09)	0.50	(0.03)	0.30	(0.04)	0.89	(0.04)
MnO	0.68	(0.04)	1.17	(0.10)	1.18	(0.10)	0.93	(0.03)	1.86	(0.07)
MgO	0.23	(0.01)	0.29	(0.02)	0.25	(0.03)	0.13	(0.01)	0.43	(0.01)
CaO	0.29	(0.04)	0.27	(0.05)	0.26	(0.05)	0.25	(0.04)	0.07	(0.03)
Na_2O	2.59	(0.09)	2.21	(0.11)	2.15	(0.15)	2.48	(0.07)	2.80	(0.11)
K_2O	4.21	(0.12)	3.59	(0.10)	3.57	(0.11)	4.46	(0.16)	3.32	(0.11)
F	ND		ND		ND		ND		ND	
O=F										
Total	92.70	(0.59)	92.09	(0.60)	91.04	(0.97)	91.46	(1.12)	91.92	(0.62)
H_2O	7.30	(0.59)	7.91	(0.60)	8.96	(0.97)	8.54	(1.12)	8.08	(0.62)
Femic	1.58	(0.09)	1.91	(0.15)	1.93	(0.11)	1.36	(0.07)	3.18	(0.09)
N	15		12		20		10		50	
	2σSD in parentheses									
	CIPW Normative Mineralogy									
Qz	41.08		45.24		44.80		38.05		36.54	
Or	27.45		24.42		24.64		30.51		23.42	
Ab	24.20		21.47		21.24		24.28		28.24	
An	1.58		1.55		1.48		1.41		0.44	
Crn	2.30		3.03		3.48		2.73		4.00	
En	0.64		0.83		0.73		0.36		1.28	
Fs	2.75		3.46		3.63		2.65		6.08	
	Mineral symbols after Whitney and Evans (2010)									
	Atoms per 8 Oxygens									
Si	3.253	(0.019)	3.119	(0.034)	3.083	(0.033)	3.058	(0.015)	2.867	(0.030)
Ti	ND		ND		ND		ND		ND	
B	0.160	(0.020)	0.403	(0.024)	0.435	(0.030)	0.409	(0.018)	0.641	(0.034)
Al	0.621	(0.013)	0.573	(0.024)	0.590	(0.022)	0.639	(0.014)	0.629	(0.008)
Fe	0.026	(0.002)	0.017	(0.003)	0.019	(0.001)	0.012	(0.002)	0.034	(0.002)
Mn	0.026	(0.001)	0.045	(0.004)	0.046	(0.004)	0.037	(0.001)	0.072	(0.003)
Mg	0.016	(0.001)	0.020	(0.001)	0.017	(0.002)	0.009	(0.001)	0.029	(0.001)
Ca	0.014	(0.002)	0.013	(0.002)	0.013	(0.002)	0.012	(0.002)	0.004	(0.002)
Na	0.232	(0.008)	0.195	(0.009)	0.192	(0.013)	0.222	(0.006)	0.248	(0.010)
K	0.248	(0.007)	0.209	(0.007)	0.210	(0.007)	0.263	(0.010)	0.194	(0.007)
F	ND		ND		ND		ND		ND	
Sum	4.596	(0.011)	4.595	(0.019)	4.605	(0.016)	4.661	(0.012)	4.718	(0.014)
ASI	1.223	(0.037)	1.329	(0.040)	1.381	(0.060)	1.254	(0.040)	1.403	(0.041)
$K^{\#}$	0.517	(0.010)	0.534	(0.043)	0.469	(0.021)	0.542	(0.010)	0.439	(0.013)
Mn*	50.417	(0.902)	27.714	(4.036)	29.697	(2.018)	20.395	(1.927)	53.138	(0.872)
$Mg^{\#}$	0.383	(0.011)	0.534	(0.043)	0.469	(0.021)	0.151	(0.008)	0.462	(0.012)
	ASI=aluminum saturation index (molar: Al/Na+K)						Mn^{*}=Mn/(Mn+Fe+Mg)*100			
	$K^{\#}$=K/K+Na						$Mg^{\#}$=Mg/(Mg+Fe)			

Table 5 cont.: EMPA Summary of Glasses

Exp#	MnGT111		MnGT76		MnGT77		MnGT126	
T(°C)	850		800/775		800/750		750	
t (hrs)	168		168/24		168/24		720	
Direction	F		R		R		F	
	F: Forward thermal direction; R: reverse thermal direction							
	Weight Percent Oxides							
SiO_2	59.41	(1.20)	60.87	(1.07)	61.98	(1.02)	64.63	(1.35)
TiO_2	0.01	(0.01)	0.01	(0.01)	0.00	(0.00)	ND	
B_2O_3	8.97	(0.30)	9.59	(0.74)	8.81	(0.77)	8.20	(0.86)
Al_2O_3	12.23	(0.18)	11.51	(0.15)	11.70	(0.13)	10.55	(0.15)
FeO*	0.76	(0.02)	0.88	(0.05)	0.63	(0.04)	0.40	(0.02)
MnO	1.88	(0.05)	1.48	(0.08)	1.46	(0.10)	0.99	(0.05)
MgO	0.45	(0.01)	0.43	(0.01)	0.43	(0.01)	0.17	(0.01)
CaO	0.09	(0.04)	0.08	(0.03)	0.07	(0.03)	0.08	(0.00)
Na_2O	2.86	(0.13)	2.82	(0.07)	2.81	(0.11)	2.62	(0.10)
K_2O	3.36	(0.09)	3.31	(0.10)	3.34	(0.12)	3.54	(0.04)
F	0.01	(0.02)	0.03	(0.03)	0.01	(0.01)	0.01	(0.02)
O=F	0.00	0.00	-0.01	(0.01)	-0.01	(0.01)	-0.01	(0.01)
Total	90.03	(1.26)	90.99	(0.48)	91.25	(0.54)	91.19	(0.83)
H_2O	9.97	(1.26)	9.01	(0.48)	8.75	(0.54)	8.81	(0.83)
Femic	3.08	(0.07)	2.80	(0.13)	2.53	(0.12)	1.56	(0.06)
N	20		20		20		25	
	2σSD in parentheses							
	CIPW Normative Mineralogy							
Qz	33.06		35.65		36.71		41.23	
Or	24.52		24.01		23.93		25.20	
Ab	29.89		29.30		28.88		26.76	
An	0.54		0.47		0.44		0.48	
Crn	4.59		3.87		4.03		2.72	
En	1.38		1.32		1.31		0.52	
Fs	6.02		5.37		4.70		3.10	
	Mineral symbols after Whitney and Evans (2010)							
	Atoms per 8 Oxygens							
Si	2.770	(0.023)	2.791	(0.045)	2.837	(0.043)	2.947	(0.053)
Ti	0.000	(0.000)	0.000	(0.000)	0.000	(0.000)		
B	0.722	(0.030)	0.759	(0.058)	0.696	(0.060)	0.645	(0.067)
Al	0.672	(0.008)	0.622	(0.009)	0.631	(0.008)	0.567	(0.009)
Fe	0.029	(0.001)	0.034	(0.002)	0.024	(0.002)	0.015	(0.001)
Mn	0.074	(0.002)	0.058	(0.003)	0.057	(0.004)	0.038	(0.002)
Mg	0.031	(0.000)	0.030	(0.001)	0.030	(0.001)	0.012	(0.001)
Ca	0.004	(0.002)	0.004	(0.002)	0.004	(0.001)	0.004	(0.000)
Na	0.259	(0.011)	0.251	(0.006)	0.250	(0.010)	0.232	(0.009)
K	0.200	(0.006)	0.193	(0.007)	0.195	(0.007)	0.206	(0.004)
F	0.002	(0.003)	0.004	(0.004)	0.002	(0.002)	0.002	(0.002)
Sum	4.762	(0.013)	4.741	(0.018)	4.722	(0.014)	4.666	(0.020)
ASI	1.438	(0.041)	1.377	(0.033)	1.398	(0.034)	1.273	(0.031)
$K^{\#}$	0.436	(0.011)	0.436	(0.009)	0.439	(0.011)	0.470	(0.011)
Mn*	55.010	(0.659)	47.572	(0.880)	51.292	(1.611)	58.722	(0.963)
$Mg^{\#}$	0.514	(0.008)	0.467	(0.013)	0.550	(0.016)	0.439	(0.016)
	ASI=aluminum saturation index (molar: Al/Na+K)					Mn^{*}=Mn/(Mn+Fe+Mg)*100		
	$K^{\#}$=K/K+Na					$Mg^{\#}$=Mg/(Mg+Fe)		

Table 5 cont.: EMPA Summary of Glasses

Exp#	MnGT78		MnGT66		MnGT67		MnGT49		MnGT56	
T(°C)	800/725		800/700		800/700		800/700		800/700	
t (hrs)	168/24		336/24		336/72		168/264		336/336	
Direction	R		R		R		F		R	
	F: Forward thermal direction; R: reverse thermal direction									
	Weight Percent Oxides									
SiO_2	60.45	(1.17)	60.67	(0.72)	61.71	(1.50)	62.92	(0.72)	61.71	(0.64)
TiO_2	0.01	(0.01)	0.01	(0.01)	0.00	(0.01)	0.01	(0.01)	0.01	(0.01)
B_2O_3	9.43	(0.62)	9.53	(0.34)	9.71	(0.62)	9.56	(0.46)	10.29	(0.36)
Al_2O_3	11.64	(0.23)	11.56	(0.19)	10.92	(0.30)	11.03	(0.22)	11.00	(0.21)
FeO*	0.74	(0.05)	0.44	(0.03)	0.37	(0.03)	0.34	(0.04)	0.32	(0.02)
MnO	1.47	(0.13)	1.60	(0.08)	1.36	(0.12)	0.89	(0.05)	1.02	(0.09)
MgO	0.37	(0.02)	0.25	(0.03)	0.20	(0.08)	0.15	(0.03)	0.11	(0.01)
CaO	0.08	(0.04)	0.07	(0.04)	0.06	(0.04)	0.06	(0.04)	0.07	(0.03)
Na_2O	2.82	(0.18)	2.97	(0.15)	2.95	(0.13)	2.94	(0.10)	2.98	(0.11)
K_2O	3.42	(0.10)	3.44	(0.08)	3.46	(0.15)	3.56	(0.10)	3.71	(0.12)
F	0.01	(0.02)	0.02	(0.03)	0.01	(0.02)	0.03	(0.03)	0.02	(0.03)
O=F	-0.01	(0.01)	-0.01	(0.01)	-0.01	(0.01)	-0.01	(0.01)	-0.01	(0.01)
Total	90.44	(0.64)	90.53	(0.79)	90.74	(0.77)	91.47	(0.74)	91.22	(0.68)
H_2O	9.56	(0.64)	9.47	(0.79)	9.26	(0.77)	8.53	(0.74)	8.78	(0.68)
Femic	2.59	(0.15)	2.28	(0.13)	1.92	(0.22)	1.38	(0.10)	1.45	(0.10)
N	20		20		20		45		20	
	2σSD in parentheses									
	CIPW Normative Mineralogy									
Qz	35.05		34.55		36.34		37.57		35.52	
Or	24.92		25.11		25.22		25.68		27.10	
Ab	29.44		31.02		30.79		30.42		31.15	
An	0.48		0.41		0.34		0.38		0.41	
Crn	3.91		3.49		2.74		2.71		2.42	
En	1.13		0.76		0.61		0.45		0.32	
Fs	5.07		4.65		3.95		2.79		3.07	
	Mineral symbols after Whitney and Evans (2010)									
	Atoms per 8 Oxygens									
Si	2.790	(0.047)	2.794	(0.020)	2.825	(0.053)	2.851	(0.026)	2.803	(0.024)
Ti	0.000	(0.000)	0.000	(0.000)	0.000	(0.000)	0.000	(0.000)	0.000	(0.000)
B	0.751	(0.051)	0.758	(0.024)	0.768	(0.052)	0.747	(0.034)	0.807	(0.025)
Al	0.633	(0.013)	0.627	(0.012)	0.589	(0.018)	0.589	(0.011)	0.589	(0.011)
Fe	0.029	(0.002)	0.017	(0.001)	0.014	(0.001)	0.013	(0.001)	0.012	(0.001)
Mn	0.058	(0.005)	0.062	(0.003)	0.053	(0.005)	0.034	(0.002)	0.039	(0.004)
Mg	0.025	(0.001)	0.017	(0.002)	0.013	(0.005)	0.010	(0.002)	0.007	(0.000)
Ca	0.004	(0.002)	0.003	(0.002)	0.003	(0.002)	0.003	(0.002)	0.003	(0.002)
Na	0.252	(0.016)	0.265	(0.013)	0.262	(0.011)	0.259	(0.008)	0.262	(0.010)
K	0.201	(0.006)	0.202	(0.005)	0.202	(0.009)	0.206	(0.006)	0.215	(0.007)
F	0.002	(0.003)	0.002	(0.004)	0.002	(0.003)	0.004	(0.004)	0.004	(0.004)
Sum	4.744	(0.022)	4.747	(0.014)	4.728	(0.026)	4.713	(0.013)	4.738	(0.014)
ASI	1.375	(0.045)	1.325	(0.038)	1.257	(0.040)	1.253	(0.028)	1.218	(0.032)
$K^{\#}$	0.444	(0.017)	0.433	(0.013)	0.436	(0.012)	0.443	(0.011)	0.451	(0.012)
Mn*	51.543	(2.200)	64.840	(1.656)	66.109	(3.882)	60.144	(2.758)	67.265	(1.646)
$Mg^{\#}$	0.470	(0.019)	0.501	(0.025)	0.468	(0.087)	0.434	(0.033)	0.372	(0.019)
	ASI=aluminum saturation index (molar: Al/Na+K)						Mn^{*}=Mn/(Mn+Fe+Mg)*100			
	$K^{\#}$=K/K+Na						$Mg^{\#}$=Mg/(Mg+Fe)			

Table 5 cont.: EMPA Summary of Glasses

Exp#	MnGT125		MnGT124		MnGT57		MnGT58	
T(°C)	700		650		800/600		800/600	
t (hrs)	720		720		336/336		336/336	
Direction	F		F		F		R	
	F: Forward thermal direction; R: reverse thermal direction							
	Weight Percent Oxides							
SiO_2	64.01	(1.67)	62.42	(0.53)	65.03	(0.34)	61.97	(0.77)
TiO_2	ND		ND		0.01	(0.01)	0.01	(0.01)
B_2O_3	8.73	(1.10)	9.59	(0.69)	7.98	(0.29)	9.99	(0.33)
Al_2O_3	10.00	(0.20)	10.43	(0.17)	10.78	(0.24)	10.88	(0.27)
FeO*	0.28	(0.02)	0.22	(0.01)	0.10	(0.01)	0.32	(0.03)
MnO	0.59	(0.03)	0.35	(0.03)	0.65	(0.05)	1.10	(0.11)
MgO	0.09	(0.01)	0.04	(0.00)	0.01	(0.00)	0.14	(0.01)
CaO	0.07	(0.00)	0.08	(0.00)	0.06	(0.03)	0.06	(0.03)
Na_2O	2.65	(0.15)	2.84	(0.13)	3.04	(0.09)	2.94	(0.12)
K_2O	3.77	(0.09)	4.13	(0.08)	3.96	(0.12)	3.63	(0.12)
F	0.01	(0.01)	0.00	(0.01)	0.03	(0.03)	0.02	(0.03)
O=F	0.00	(0.00)	0.00	(0.00)	-0.01	(0.01)	-0.01	(0.01)
Total	90.20	(1.08)	90.11	(0.89)	91.62	(0.41)	91.05	(0.48)
H_2O	9.80	(1.08)	9.89	(0.89)	8.38	(0.41)	8.95	(0.48)
Femic	0.96	(0.04)	0.62	(0.03)	0.76	(0.05)	1.55	(0.14)
N	25		25		20		20	
	2σSD in parentheses							
	CIPW Normative Mineralogy							
Qz	40.67		36.52		37.62		36.30	
Or	27.35		30.28		27.96		26.49	
Ab	27.52		29.81		30.72		30.74	
An	0.45		0.50		0.34		0.36	
Crn	1.75		1.43		1.68		2.47	
En	0.27		0.13		0.02		0.42	
Fs	1.99		1.32		1.67		3.23	
	Mineral symbols after Whitney and Evans (2010)							
	Atoms per 8 Oxygens							
Si	2.939	(0.063)	2.868	(0.030)	2.957	(0.016)	2.822	(0.032)
Ti	ND		ND		0.000	(0.000)	0.000	(0.000)
B	0.692	(0.088)	0.760	(0.047)	0.626	(0.020)	0.785	(0.025)
Al	0.541	(0.011)	0.565	(0.012)	0.578	(0.013)	0.584	(0.015)
Fe	0.011	(0.001)	0.009	(0.000)	0.004	(0.001)	0.012	(0.001)
Mn	0.023	(0.001)	0.014	(0.001)	0.025	(0.002)	0.042	(0.004)
Mg	0.006	(0.000)	0.003	(0.000)	0.000	(0.000)	0.009	(0.001)
Ca	0.004	(0.000)	0.004	(0.000)	0.003	(0.001)	0.003	(0.001)
Na	0.236	(0.013)	0.253	(0.011)	0.268	(0.008)	0.260	(0.010)
K	0.221	(0.006)	0.242	(0.006)	0.229	(0.007)	0.211	(0.007)
F	0.001	(0.002)	0.001	(0.001)	0.004	(0.005)	0.003	(0.005)
Sum	4.673	(0.016)	4.717	(0.013)	4.690	(0.009)	4.729	(0.018)
ASI	1.167	(0.044)	1.125	(0.035)	1.150	(0.033)	1.226	(0.032)
$K^{\#}$	0.484	(0.013)	0.489	(0.013)	0.462	(0.012)	0.448	(0.012)
Mn*	57.713	(1.632)	54.472	(2.608)	86.157	(1.590)	66.474	(1.325)
$Mg^{\#}$	0.354	(0.016)	0.258	(0.022)	0.100	(0.072)	0.433	(0.017)
	ASI=aluminum saturation index (molar: Al/Na+K)					Mn^{*}=Mn/(Mn+Fe+Mg)*100		
	$K^{\#}$=K/K+Na					$Mg^{\#}$=Mg/(Mg+Fe)		

Table 5-6 Mineral-Melt Partition and Exchange Coefficients

	Exp #	BC	T (°C)	D_{FeO}	D_{MnO}	D_{MgO}	$*K_{DMnO/FeO}$	$*K_{DMgO/FeO}$	
Grt/melt	GBT-90	1.3	850	8.07	15.62	7.45	1.87	0.55	w/Crd
Grt/melt	MnGT-76	4.1	775	9.71	21.34	7.34			Grt only
Grt/melt	GBT-88	1.3	750	11.82	20.74	8.74			w/Crd
Grt/melt	GBT-101	1.3	750	21.56	24.85	8.91			w/Crd
Grt/melt	MnGT-77	4.1	750	11.31	23.01	7.23			w/Tur
Grt/melt	MnGT-49	4.1	700	26.78	35.69	16.01			w/Tur
Grt/melt	MnGT-56	4.1	700	19.95	36.37	14.02			w/Tur
Grt/melt	GBT-103	1.3	650	22.53	38.76	7.93			w/Crd&Tur
Crd/melt	GBT-90	1.3	850	2.55	1.83	11.14	0.65	3.03	w/Grt
Crd/melt	MnGT-89	#	850	2.20	---	9.93			Crd only
Crd/melt	GBT-88	1.3	750	4.39	2.57	18.07			w/Grt
Crd/melt	GBT-101	1.3	750	8.01	3.54	21.84			w/Grt
Crd/melt	GBT-102	1.3	700	6.79	3.64	31.95			w/Grt
Crd/melt	GBT-103	1.3	650	16.73	7.37	49.77			w/Grt&Tur
Crd/melt	4.1-1		750	11.15	7.19	32.56			Icenhower (1995)
Crd/melt	4C-8		750	13.71	10.50	37.44			"
Crd/melt	4C-11		750	19.49	14.46	---			"
Crd/melt	4.2-1		750	11.60	9.93	41.64			"
Crd/melt	5-17		700	13.98	9.33	43.68			"
Crd/melt	5-18		700	14.73	8.57	42.17			"
Crd/melt	5-19		700	16.02	8.93	43.87			"
Crd/melt	6M-3		700	14.18	8.92	32.62			"
Crd/melt	5+11		700	15.00	7.66	28.80			"
Crd/melt	15-10		700	12.65	11.92	33.60			"
Crd/melt	4.1-2		650	16.92	15.08	38.17			"
Crd/melt	4.2-2		650	18.43	8.50	55.09			"
Crd/melt	4C-13		650	17.00	---	61.00			"

BC: Bulk Composition

Mineral abbreviations after Whitney and Evans (2010)

*Average KD values from slope of each regression in Figures 7a-7b

Errors for mean D values are less than 10% relative, and most commonly ~ 5%.

Table 6 cont.: Mineral-Melt Partition and Exchange Coefficients

	Exp #	BC	T (°C)	D_{FeO}	D_{MnO}	D_{MgO}	$*K_{DMnO/FeO}$	$*K_{DMgO/FeO}$	
Tur/melt	GBT-98	1.2+	750	17.76	0.36	29.87	0.03	1.37	Tur only
Tur/melt	GBT-79	1.2	750	14.57	0.38	16.79			Tur only
Tur/melt	MnGT-77	4.1	750	14.64	0.46	14.11			w/Grt
Tur/melt	MnGT-78	4.1	725	13.56	0.44	15.91			w/Grt
Tur/melt	MnGT-49	4.1	700	23.52	0.64	37.88			w/Grt
Tur/melt	MnGT-56	4.1	700	31.11	0.90	---			w/Grt
Tur/melt	MnGT-66	4.1	700	20.89	0.64	26.14			Tur only
Tur/melt	MnGT-67	4.1	700	25.42	0.72	33.02			Tur only
Tur/melt	GBT-83	1.2	700	28.77	0.68	30.77			Tur only
Tur/melt	GBT-99	1.2+	700	30.29	0.57	---			Tur only
Tur/melt	GBT-103	1.3	650	30.28	1.62	49.93			w/Grt&Crd
Tur/melt	GBT-85	1.2+	650	31.36	1.01	---			Tur only
Bt/melt	6+4		750	18.42	3.71	67.33	0.21	3.03	Icenhower and London (1995)
Bt/melt	7+4		750	17.83	3.78	72.40			"
Bt/melt	5+6		750	16.80	3.50	76.00			"
Bt/melt	5+9		700	20.49	3.25	68.78			"
Bt/melt	5+7		700	19.60	5.00	49.54			"
Bt/melt	6+7		700	22.19	4.50	85.71			"
Bt/melt	6+5		700	27.96	5.50	84.29			"
Bt/melt	7+7		700	20.75	3.75	74.00			"
Bt/melt	7+5		700	21.03	4.63	54.91			"
Bt/melt	7+10		650	28.45	6.83	73.63			"
Bt/melt	7+6		650	27.89	5.57	76.25			"
Bt/melt	5+14		650	23.38	4.86	54.55			"
Bt/melt	5+15		650	20.19	5.43	37.63			"
Bt/melt	5+8		650	23.69	4.25	50.42			"
Ms/Melt	5+14		650	5.17	1	16	0.21	3.03	Icenhower and London (1995)
Ms/Melt	5+15		650	4.28	1	10.75			"
Ms/Melt	7+10		650	6.91	1.5	20.75			"

BC: Bulk Composition

Mineral abbreviations after Whitney and Evans (2010)

*Average KD values from slope of each regression in Figures 7a-7b

Errors for mean D values are less than 10% relative, and most commonly ~ 5%.

References

Acosta-Vigil, A., Buick, I.S., Hermann, J., Cesare, B., Rubatto, D., London, D., Morgan, G.B., 2010. Mechanisms of crustal anatexis: a geochemical study of partially melted metapelitic enclaves and host dacite, SE Spain. J. Petrol. 51, 785–821.

Acosta-Vigil, A., Cesare, B., London, D., Morgan, G.B., 2007. Microstructures and composition of melt inclusions in a crustal anatectic environment, represented by metapelitic enclaves within El Hoyazo dacits, SE Spain. Chem. Geol. 237, 450–465.

Acosta-Vigil, A., London, D., Dewers, T.A., Morgan, G.B., 2002. Dissolution of Corundum and Andalusite in H2O-Saturated Haplogranitic Melts at 800°C and 200 MPa: Constraints on Diffusivities and the Generation of Peraluminous Melts. J. Petrol. 43, 1885–1908. doi:10.1093/petrology/43.10.1885

Acosta-Vigil, A., London, D., Morgan IV, G.B., Dewers, T.A., 2003. Solubility of excess alumina in hydrous granitic melts in equilibrium with peraluminous minerals at 700-800 °C and 200 MPa, and applications of the aluminum saturation index. Contrib. to Mineral. Petrol. 146, 100–119. doi:10.1007/s00410-003-0486-6

Baker, D.R., 1996. Granitic melt viscosities: Empirical and configurational entropy models for their calculation. Am. Mineral. 81, 126–134.

Baker, D.R., 1992. Tracer diffusion of network formers and multicomponent diffusion in dacitic and rhyolitic melts. Geochim. Cosmochim. Acta 56, 617–631.

Baker, L.R., Rutherford, M.J., 1996. The effect of dissolved water on the oxidation state of silicic melts. Geochim. Cosmochim. Acta 60, 2179–2187.

Bartels, A., Vetere, F., Holtz, F., Behrens, H., Linnen, R.L., 2011. Viscosity of flux-rich pegmatitic melts. Contrib. to Mineral. Petrol. 162, 51–60. doi:10.1007/s00410-010-0582-3

Bea, F., 1996. Controls on the trace element composition of crustal melts, in: Brown, M., Candela, P.A., Peck, D.L., Stephens, W.E., Walker, R.J., Zen, E.-A. (Eds.), The Third Hutton Symposium on the Origin of Granites and Related Rocks. Geological Society of America Special Paper, pp. 33–41.

Beattie, P., Drake, M., Jones, J., Leeman, W., Longhi, J., McKay, G., Nielsen, R., Palme, H., Shaw, D., Takahashi, E., Watson, B., 1993. Terminology for trace-element partitioning. Geochim. Cosmochim. Acta 57, 1605–1606. doi:10.1016/0016-7037(93)90015-O

Beurlen, H., Trumbull, R.B., Wiedenbeck, M., Soares, D.R., 2011. Boron-isotope variations in tourmaline from granitic pegmatites of the Borborema pegmatite province, NE-Brazil. PEG 2011 14, 37–39.

Brenan, J.M., Neroda, E., Lundstrom, C.C., Shaw, H.F., Ryerson, F.J., Phinney, D.L., 1998. Behaviour of boron, beryllium, and lithium during melting and crystallization: Constraints from mineral-melt partitioning experiments. Geochim. Cosmochim. Acta 62, 2129–2141.

Cameron, E.N., Jahns, R.H., McNair, A.H., Page, L.R., 1949. Internal structure of granitic pegmatites. Econ. Geol. Monogr. 2.

Catanzaro, E.J., Champion, C.E., Garner, E.L., Marinenko, G., Sappenfield, K.M., Shields, W.R., 1970. Standard Reference Materials: Boric Acid; Isotopic, and Assay Standard Reference Materials. NBS Spec. Publ. 260, 1–70.

Černý, P., Ercit, T.S., 2005. The classification of granitic pegmatites revisited. Can. Mineral. 43, 2005–2026.

Černý, P., London, D., Novak, M., 2012. Granitic pegmatites as reflections of their sources. Elements 8, 289–294.

Černý, P., Meintzer, R.E., Anderson, A.J., 1985. Extreme fractionation in rare-element granitic pegmatites: Selected examples of data and mechanisms. Can. Mineral. 23, 381–421.

Chakraborty, S., Dingwell, D.B., Chaussidon, M., 1993. Chemical diffusivity of boron in melts of haplogranitic composition. Geochim. Cosmochim. Acta 57, 1741–1751.

Chappell, B.W., White, A.J.R., 2001. Two contrasting granite types: 25 years later. Aust. J. Earth Sci. 48, 489–499.

Christiansen, E.H., Bikun, J. V., Sheridan, M.F., Burt, D.M., 1984. Geochemical evolution of topaz rhyolites from the Thomas Range and Spor Mountain, Utah. Am. Mineral. 69, 223–236.

Clemens, J.D., Wall, V.J., 1981. Origin and crystallization of some peraluminous (S-type) granitic magmas. Can. Mineral. 19, 111–131.

Crank, J., 1975. The Mathematics of Diffusion. Oxford University Press.

da Costa, I.R., Mourao, C., Recio, C., Guimaraes, F., Antunes, I.M., Ramos, J.F., Barriga, F.J.A.S., Palmer, M.R., Milton, J.A., 2014. Tourmaline occurrences within the Penamacor-Monsanto granitic pluton and host-rocks (Central Portugal): genetic implications of crystal-chemical and isotopic features. Contrib. to Mineral. Petrol. 167, 1–23. doi:10.1007/s00410-014-0993-7

De Vito, C., Aurisicchio, C., Ferrini, V., Pezzotta, F., 2002. Chemical composition and B, O and H isotopes of tourmaline from Anjanabonoina pegmatite. Int. Mineral. Assoc. Abstr. 208.

Dingwell, D.B., Pichavant, M., Holtz, F., 1996. Experimental studies of boron in granitic melts. Rev. Mineral. Geochemistry 33, 331–386.

Dini, A., Tonarini, S., 2002. Boron isotope geochemistry: new insights from the study of borates and boro-silicates in granite-pegmatite systems. Int. Mineral. Assoc. Abstr. 205.

Dini, A., Tonarini, S., Pezzotta, F., De Vito, C., 2002. Boron isotopes study of borates and boro-silicates from Anjanabonoina and Tetezantsio pegmatites (Central Madagascar). Int. Mineral. Assoc. Abstr. 210.

Drivenes, K., Larsen, R.B., Müller, A., Sørensen, B.E., Wiedenbeck, M., Raanes, M.P., 2015. Late-magmatic immiscibility during batholith formation : assessment of B isotopes and trace elements in tourmaline from the Land ' s End granite , SW England. Contrib. to Mineral. Petrol. 169, 1–27. doi:10.1007/s00410-015-1151-6

Dwivedi, S.B., Mohan, A., Lal, R.K., 1998. Recalibration of the Fe-Mg exchange reaction between garnet and cordierite as a thermometer. Eur. J. Mineral. 10, 281–289.

Dyar, M.D., Wiedenbeck, M., Robertson, D., Cross, L.R., Delaney, J.S., Ferguson, K., Francis, C.A., Grew, E.S., Guidotti, C. V., Hervig, R.L., Hughes, J.M., Husler, J., Leeman, W.P., McGuire, A.V., Rhede, D., Rothe, H., Paul, R.L., Richards, I., Yates, M.G., 2001. Reference minerals for the microanalysis of light elements. Geostand. Newsl. 25, 441–463.

Fisher, J., 2002. Gem and rare element pegmatites of southern California. Mineral. Rec. 33, 363–407.

Foord, E.E., 1982. Bismuthian stibiocolumbite-tantalite and other minerals form the Little Three min, Ramona, California. Am. Mineral. 67, 181–182.

Foord, E.E., London, D., Kampf, A.R., Shigley, J.E., Snee, L.W., 1991a. Gem-bearing pegmatites of San Diego County, California. Geol. Excursions South. Calif. Mex. 128–146.

Foord, E.E., Martin, R.F., Fitzpatrick, J.J., Taggart, J.E., Crock, J.G.J., 1991b. Boromuscovite, a new member of the mica group, from the Little Three min pegmatite, Ramona district, San Diego County, California. Am. Mineral. 76, 1998–2002.

Foord, E.E., Spaulding, L.B., Martin, R.F., Mason, R.A., 1989. Mineralogy and paragenesis of the Little Three mine pegmatites, Ramona district, San Diego County, California 20, 101–127.

Foord, E.E., Starkey, H.C., Taggart, J.E., 1986. Mineralogy and paragenesis of "pocket" clays and associated minerals in complex pegmatites. Am. Mineral. 71, 428–439.

Frost, B.R., Barnes, C.G., Collins, W.J., Arculus, R.J., Ellis, D.J., Frost, C.D., 2001. A geochemical classification for granitic rocks. J. Petrol. 42, 2033–2048.

Geisinger, K.L., Oestrike, R., Navrotsky, A., Turner, G.L., Kirkpatrick, R.J., 1988. Thermochemistry and structure of glasses along the join NaAlSi3O8-NaBSi3O8.

Geochim. Cosmochim. Acta 52, 2405–2414. doi:10.1016/0016-7037(88)90297-9

Giordano, D., Romano, C., Dingwell, D.B., Poe, B., Behrens, H., 2004. The combined effects of water and fluorine on the viscosity of silicic magmas. Geochim. Cosmochim. Acta 68, 5159–5168. doi:10.1016/j.gca.2004.08.012

Grew, E.S., 1996. Borosilicates (exclusive of tourmaline) and Boron in rock-forming minerals in metamorphic environments. Rev. Mineral. Geochemistry 33, 387–502.

Grew, E.S., Locock, A.J., Mills, S.J., Galuskina, I.O., Galuskin, E. V., Hålenius, U., 2013. IMA report: Nomenclature of the garnet supergroup. Am. Mineral. 98, 785–811. doi:10.2138/am.2013.4201

Hawthorne, F.C., Burns, P.C., Grice, J.D., 1996. The Crystal Chemistry of Boron. Rev. Mineral. Geochemistry 33, 41–116.

Henry, D.J., Novák, M., Hawthorne, F.C., Ertl, A., Dutrow, B.L., Uher, P., Pezzotta, F., 2011. Nomenclature of the tourmaline-supergroup minerals. Am. Mineral. 96, 895–913. doi:10.2138/am.2011.3636

Hervig, R.L., 1996. Analyses of geological materials for boron by secondary ion mass spectrometry. Rev. Mineral. Geochemistry 33, 789–804.

Hervig, R.L., Moore, G.M., Williams, L.B., Peacock, S.M., Holloway, J.R., Roggensack, K., 2002. Isotopic and elemental partitioning of boron between hydrous fluid and silicate melt. Am. Mineral. 87, 769–774. doi:10.2138/am-2002-5-620

Holdaway, M.J., 2004. Optimization of some key geothermobarometers for pelitic metamorphic rocks. Mineral. Mag. 68, 1–14.

Holtz, F., Dingwell, D.B., Behrens, H., 1993. Effects of F, B2O3, and P2O5 on the solubility of water in haplogranite melts compared to natural silicate melts. Contrib. to Mineral. Petrol. 113, 492–501.

Huebner, J.S., Sato, M., 1970. The oxygen fugacity-temperature relationships of manganese oxide and nickel oxide buffers. Am. Mineral. 55, 934–952.

Icenhower, J.P., 1995. Experimental determination of element behavior in silicic systems during hydrous partial fusion. University of Oklahoma.

Icenhower, J.P., London, D., 1995. An experimental study of element partitioning among biotite, muscovite, and coexisting peraluminous silicic melt at 200 MPa (H2O). Am. Mineral. 80, 1229–1251.

Ildefonse, J.P., Jambon, A., Carron, J.P., Delbove, F., Gabis, V., 1979. La diffusion chimique dans les solutions hydrothermales et dans les verres et magmas silicates. Sci. Geol. Mem 53, 81–85.

Jahns, R.H., Burnham, C.W., 1969. Experimental studies of pegmatite genesis: I. A

model for the derivation and crystallization of granitic pegmatites. Econ. Geol. 64, 843–864. doi:10.2113/gsecongeo.64.8.843

Jambon, A., 1980. Isotopic fractionation: a kinetic model for crystals growing from magmatic melts. Geochim. Cosmochim. Acta 44, 1373–1380.

Jiang, S.-Y., Palmer, M.R., 1998. Boron isotope systematics of tourmaline from granites and pegmatites; a synthesis. Eur. J. Mineral. 10, 1253–1265.

Jiang, S.Y., Radvanec, M., Nakamura, E., Palmer, M., Kobayashi, K., Zhao, H.X., Zhao, K.D., 2008. Chemical and boron isotopic variations of tourmaline in the Hnilec granite-related hydrothermal system, Slovakia: Constraints on magmatic and metamorphic fluid evolution. Lithos 106, 1–11. doi:10.1016/j.lithos.2008.04.004

Jiang, S.Y., Yang, J.H., Novák, M., Selway, J., 2003. Chemical and boron isotopic compositions of tourmaline from the Lavicky leucogranite, Czech Republic. Geochem. J. 37, 545–556. doi:10.2343/geochemj.37.545

Kakihana, H., Kotaka, M., Satoh, S., Nomura, M., Okamoto, M., 1977. Fundamental Studies on the Ion-Exchange Separation of Boron Isotopes. Bull. Chem. Soc. Jpn. doi:10.1246/bcsj.50.158

Kasemann, S., Erzinger, J., Franz, G., 2000. Boron recycling in the continental crust of the central Andes from the Palaeozoic to Mesozoic, NW Argentina. Contrib. to Mineral. Petrol. 140, 328–343. doi:10.1007/s004100000189

Koga, K.., Rose-Koga, E.F., Laporte, D., Cluzel, N., Shimizu, N., Deloule, E., 2011. Lithium-Boron isotope fractionation during degassing of rhyolitic melt. Goldscmidt Conf. Abstr. 1211.

Kordela, D.G., 1990. Little Three mine. Rocks Gems 20, 70–72.

Kowalski, P.M., Wunder, B., Jahn, S., 2013. Ab initio prediction of equilibrium boron isotope fractionation between minerals and aqueous fluids at high P and T. Geochim. Cosmochim. Acta 101, 285–301. doi:10.1016/j.gca.2012.10.007

Laurs, B.M., Knox, K., 2001. Spessartine garnet from Ramona, San Diego County, California. Gems Gemol. 37, 278–295.

Leeman, W.P., Sisson, V.B., 1996. Geochemistry of Boron and its implications for crustal and mantle processes. Rev. Mineral. Geochemistry 33, 645–708.

Leeman, W.P., Tonarini, S., 2001. Boron isotopic analysis of proposed borosilicate mineral reference samples. Geostand. Newsl. 25, 399–403.

London, D., 2014. Subsolidus isothermal fractional crystallization. Am. Mineral. 99, 543–546. doi:10.1515/am.2014.4693

London, D., 2013. Crystal-Filled Cavities in Granitic Pegmatites: Bursting the Bubble.

Rocks Miner. 88, 527–538. doi:10.1080/00357529.2013.826090

London, D., 2009. The origin of primary textures in granitic pegmatites. Can. Mineral. 47, 697–724. doi:10.3749/canmin.47.4.697

London, D., 2008. Pegmatites, Canadian Mineralogist.

London, D., 1992. The application of experimental petrology to the genesis and crystallization of granitic pegmatites. Can. Mineral. 30, 499–540.

London, D., Burt, D.M., 1982. Alteration of spodumene, montebrasite and lithiophilite in pegmatites of the White Picacho district, Arizona. Am. Mineral. 67, 97–113.

London, D., Evensen, J.M., Fritz, E.A., Icenhower, J.P., Morgan, G.B., Wolf, M.B., 2001. Enrichment and accomodation of manganese in granite-pegmatite systems, in: Eleventh Annual V.M. Goldscmidt Conference. Hot Springs, VA, p. abstract no.3369.

London, D., Hervig, R.L., Morgan VI, G.B., 1988. Melt-vapor solubilities and elemental partitioning in peraluminous granite-pegmatite systems: experimental results with Macusani glass at 200 MPa. Contrib. to Mineral. Petrol. 99, 360–373. doi:10.1007/BF00375368

London, D., Morgan, G.B., 2017. Experimental crystallization of the Macusani obsidian, with applications to lithium-rich pegmatites. J. Petrol. accepted.

London, D., Morgan VI, G.B., Wolf, M.B., 1996. Boron in granitic rocks and their contact aureoles. Rev. Mineral. Geochemistry 33, 299–330.

London, D., Morganvi, G.B., Paul, K.A., Guttery, B.M., 2012. Internal evolution of miarolitic granitic pegmatites at the little three Mine, Ramona, California, USA. Can. Mineral. 50, 1025–1054. doi:10.3749/canmin.50.4.1025

London, D., Wolf, M.B., Morgan Vi, G.B., Garrido, M.G., 1999. Experimental Silicate–Phosphate Equilibria in Peraluminous Granitic Magmas, with a Case Study of the Alburquerque Batholith at Tres Arroyos, Badajoz, Spain. J. Petrol. 40, 215–240.

Ludwig, T., Marschall, H.R., Von Strandmann, P.A.E.P., Shabaga, B.M., Fayek, M., Hawthorne, F.C., 2011. A secondary ion mass spectrometry (SIMS) re-evaluation of B and Li isotopic compositions of Cu-bearing elbaite from three global localities. Mineral. Mag. 75, 2485–2494. doi:10.1180/minmag.2011.075.4.2485

Maner, J.L., London, D., 2017. The boron isotopic evolution of the Little Three pegmatites, Ramona, CA. Chem. Geol. 460, 70–83.

Maner, J.L., London, D., Morgan, G.B., 2014. Elemental partioning and zoning in tourmalien: An experimental investigation, in: Goldscmidt Conference Abstracts. Sacramento, California.

Maner, J.L., London, D., Morgan, G.B., 2013. Toward an experimentally calibrated

garnet-tourmaline geothermometer, in: Geological Society of America Abstracts with Programs. Austin, TX, p. 17.

Marschall, H.R., Ludwig, T., 2006. Re-examination of the boron isotopic composition of tourmaline from the Lavicky granite, Czech Republic, by secondary ion mass spectrometry: Back to normal. Geochem. J. 40, 631–638. doi:10.2343/geochemj.40.631

Marschall, H.R., Ludwig, T., Altherr, R., Kalt, A., Tonarini, S., 2006. Syros metasomatic tourmaline: Evidence for very high-δ11 B fluids in subduction zones. J. Petrol. 47, 1915–1942. doi:10.1093/petrology/egl031

Marschall, H.R., Meyer, C., Wunder, B., Ludwig, T., Heinrich, W., 2009. Experimental boron isotope fractionation between tourmaline and fluid: Confirmation from in situ analyses by secondary ion mass spectrometry and from Rayleigh fractionation modelling. Contrib. to Mineral. Petrol. 158, 675–681. doi:10.1007/s00410-009-0403-8

Marschall, H.R., Wanless, V.D., Shimizu, N., Pogge von Strandmann, P.A.E., Elliott, T., Monteleone, B.D., 2017. The boron and lithium isotopic composition of mid-ocean ridge basalts and the mantle. Geochim. Cosmochim. Acta 207, 102–138.

Maya, L., 1976. Identification of polyborate and fluoropolyborate ions in solution by Raman spectroscopy. Inorg. Chem. 15, 2179–2184. doi:10.1021/ic50163a036

Meyer, C., Wunder, B., Meixner, A., Romer, R.L., Heinrich, W., 2008. Boron-isotope fractionation between tourmaline and fluid: An experimental re-investigation. Contrib. to Mineral. Petrol. 156, 259–267. doi:10.1007/s00410-008-0285-1

Moore, G., Righter, K., Carmichael, I.S.E., 1995. The effect of dissolved water on the oxidation state of iron in natural silicate liquids. Contrib. to Mineral. Petrol. 120.

Morgan, G.B., 2016. A spreadsheet for calculating normative mole fractions of end-member species for Na-Ca-Li-Fe $^{2+}$ -Mg-Al tourmalines from electron microprobe data. Am. Mineral. 101, 111–119. doi:10.2138/am-2016-5392

Morgan, G.B., London, D., 2005. Effect of current density on the electron microprobe analysis of alkali aluminosilicate glasses. Am. Mineral. 90, 1131–1138.

Morgan, G.B., London, D., 1999. Crystallization of the Little Three layered pegmatite-aplite dike, Ramona District, California. Contrib. to Mineral. Petrol. 136, 310–330. doi:10.1007/s004100050541

Morgan, G.B., London, D., Kirkpatrick, R.J., 1990. Reconnaissance spectroscopic study of hydrous sodium aluminum borosilicate glasses. Geol. Soc. Am. Abstr. with Programs 22, A167.

Morgan VI, G.B., London, D., 1996. Optimizing the electron microprobe analysis of hydrous alkali aluminosilicate glasses. Am. Mineral. 81, 1176–1185. doi:10.2138/am.2005.1769

Mukhopadhyay, B., Holdaway, M.J., 1994. Cordierite-garnet-sillimanite-quartz equilibrium: I. New experimental calibration in the system FeO-Al2O3-SiO2-H2O and certain P-T-XH2O relations. Contrib. to Mineral. Petrol. 116, 462–472.

Müller, A., Kearsley, A., Spratt, J., Seltmann, R., 2012. Petrogenetic implications of magmatic garnet in granitic pegmatites from Southern Norway. Can. Mineral. 50, 1095–1115. doi:10.3749/canmin.50.4.1095

Müller, A., Seltmann, R., Halls, C., Siebel, W., Dulksi, P., Jeffries, T., Spratt, J., Kronz, A., 2006. The magmatic evolution of the Land's End Pluton, Cornwall, and associated pre-enrichment of metals. Ore Geol. Rev. 28, 329–367.

Mungall, J.E., 2002. Empircal models relating viscosity and tracer diffusion in magmatic silicate melts. Geochim. Cosmochim. Acta 66, 125–143.

Mungall, J.E., Dingwell, D.B., Chaussidon, M., 1999. Chemical diffusivites of 18 trace elements in granitoid melts. Geochim. Cosmochim. Acta 63, 2599–2610.

Novak, M., Burns, P.C., Morgan, G.B., 1998. Fluorine variations in hambergite from granitic pegmatites. Can. Mineral. 36, 441–446.

Palmer, M., London, D., Morgan VI, G., Babb, H., 1992. Experimental determination of fractionation of 11B/10B between tourmaline and aqueous vapor: A temperature- and pressure-dependent isotopic system. Chem. Geol. 101, 123–129. doi:http://dx.doi.org/10.1016/0009-2541(92)90209-N

Palmer, M.R., Swihart, G.H., 1996. Boron isotope geochemistry: An overview. Rev. Mineral. Geochemistry 33, 709–744.

Pereira, M.D., Bea, F., 1994. Cordierite-producing reactions in the Pena Negra complex, Avila batholith, central Spain: The key role of cordierite in low-pressure anatexis. Can. Mineral. 31, 763–780.

Pesquera, A., Torres-Ruiz, J., Gil-Crespo, P.P., Jiang, S.Y., 2005. Petrographic, chemical and B-isotopic insights into the origin of Tourmaline-Rich rocks and boron recycling in the Martinamor Antiform (Central Iberian Zone, Salamanca, Spain). J. Petrol. 46, 1013–1044. doi:10.1093/petrology/egi009

Phillips, G.N., Wall, V.J., Clemens, J.D., 1981. Petrology of the Strathbogie batholith: a cordierite-bearing granite. Can. Mineral. 19, 47–63.

Pichavant, M., 1981. An experimental study of the effect of boron on a water saturated haplogranite at 1 Kbar vapour pressure - Geological applications. Contrib. to Mineral. Petrol. 76, 430–439. doi:10.1007/BF00371485

Pouchou, J.L., Pichoir, F., 1985. "PAP" (ϕ-ρ-z) correction procedure for improved quantitative microanalysis, in: Microbeam Analysis. San Francisco Press, California, pp. 104–106.

Richter, F.M., Davis, A.M., DePaolo, D.J., Watson, E.B., 2003. Isotopic fractionation

by chemical diffusion between molten basalt and rhyolite. Geochim. Cosmochim. Acta 20, 3905–3923.

Richter, F.M., Liang, Y., Davis, A.M., 1999. Isotope fractionation by diffusion in molten oxides. Geochim. Cosmochim. Acta 63, 2853–2861.

Romer, R.L., Kirsch, M., Kroner, U., 2011. Geochemical signature of Ordovician Mn-rich sedimentary rocks on the Avalonian shelf. Can. J. Earth Sci. 48, 703–718.

Romer, R.L., Meixner, A., 2014a. Lithium and boron in late-orogenic granites – Isotopic fingerprints for the source of crustal melts? 131, 98–114. doi:10.1016/j.gca.2014.01.018

Romer, R.L., Meixner, A., 2014b. Lithium and boron isotopic fractionation in sedimentary rocks during metamorphism – The role of rock composition and protolith mineralogy. Geochim. Cosmochim. Acta 128, 158–177. doi:10.1016/j.gca.2013.11.032

Rosner, M., Erzinger, J., Franz, G., Trumbull, R.B., 2003. Slab-derived boron isotope signatures in arc volcanic rocks from the Central Andes and evidence for boron isotope fractionation during progressive slab dehydration. Geochemistry, Geophys. Geosystems 4. doi:10.1029/2002GC000438

Roy, S., 1997. Genetic diversity of manganese deposition in the terrestrial geological record, Special Pu. ed. Geological Society, London.

Sanchez-Valle, C., Reynard, B., Daniel, I., Lecuyer, C., Martinez, I., Chervin, J.C., 2005. Boron isotopic fractionation between minerals and fluids: New insights from in situ high pressure-high temperature vibrational spectroscopic data. Geochim. Cosmochim. Acta 69, 4301–4313. doi:10.1016/j.gca.2005.03.054

Schmidt, B.C., Zotov, N., Dupree, R., 2004. Structural implications of water and boron dissolution in albite glass. J. Non. Cryst. Solids 337, 207–219. doi:10.1016/j.jnoncrysol.2004.04.007

Schmidt, C., Thomas, R., Heinrich, W., 2005. Boron speciation in aqueous fluids at 22 to 600??C and 0.1 MPa to 2 GPa. Geochim. Cosmochim. Acta 69, 275–281. doi:10.1016/j.gca.2004.06.018

Shearer, C.K., Papike, J.J., Jolliff, B.L., 1992. Petrogenetic links among granites and pegmatites in the Harney Peak rare-element granite-pegmatite system, Black Hills, South Dakota. Can. Mineral. 30, 785–809.

Siegel, K., Wagner, T., Trumbull, R.B., Jonsson, E., Matalin, G., Wälle, M., Heinrich, C.A., 2016. Stable isotope (B, H, O) and mineral-chemistry constraints on the magmatic to hydrothermal evolution of the Varuträsk rare-element pegmatite (Northern Sweden). Chem. Geol. 421, 1–16. doi:10.1016/j.chemgeo.2015.11.025

Simmons, W.B., Foord, E.E., Falster, A.U., King, V.T., 1996. Evidence for an anatectic origin of granitic pegmatites, western Maine, USA, in: Geological Society of

America Abstracts with Programs. p. 27:411.

Simmons, W.B., Pezzotta, F., Shigley, J.E., Beurlen, H., 2012. Granitic pegmatites: Storehouses of colored gemstones. Elements 8, 281–287.

Simpson, D.R., 1965. Geology of the central part of the Ramona pegmatite district. Calif. Div. Mines Geol., Spec. Rep. 86, 3–23.

Sinkankas, J., 1967. Notes on some minerals from San Diego County, California. Gems Gemol. 363, 34–35.

Sinkankas, J., 1956. Recent gem mining at Ramona, San Diego County, California. Gems Gemol. 8, 367–373.

Smith, M.P., Yardley, B.W.D., 1996. The boron isotopic composition of tourmaline as a guide to fluid processes in the southwestern England orefield: An ion microprobe study. Geochim. Cosmochim. Acta 60, 1415–1427. doi:10.1016/0016-7037(96)00007-5

Stern, L.A., Brown, G.E., Bird, D.K., Jahns, R.H., Foord, E.E., Shigley, J.E., Spaulding, L.B., J., 1986. Mineralogy and geochemical evolution of the little three pegmatite-aplite layered intrusive, Ramona, California. Am. Mineral. 71, 406–427.

Stevens, G., Villaros, A., Moyen, J.F., 2007. Selective peritectic garnet entertainment as the origin of geochemical diversity in S-type granites. Geology 35, 9–12. doi:10.1130/G22959A.1

Stewart, D.B., 1978. Petrogenesis of lithium-rich pegmatites. Am. Mineral. 63, 970–980.

Strong, D.F., Hammer, S.K., 1981. The leucogranites of southern Brittany: origin by faulting, frictional heating, fluid flux and fractional melting. Can. Mineral. 19, 163–176.

Symons, D.T.A., Smith, T.E., Kawasaki, K., Walawender, M.J., 2009. Paleomagnetism of the mid-Cretaceous gem-bearing pegmatite dikes of San Diego County, California, USA. Can. J. Earth Sci. 46, 675–687. doi:10.1139/E09-035

Symons, D.T.A., Wlawender, M.J., Smith, T.E., Molnar, S.E., Harris, M.J., Blackburn, W.H., 2003. Paleomagnetism and geobarometry of the La Posta pluton, California. Geol. Soc. Am. Special Pa, 135–155. doi:10.1130/0-8137-2374-4.135

Taylor, J.F., Wall, V.J., 1992. The behavior of tin in granitoid magmas. Econ. Geol. 87, 403–420.

Todd, V.R., Shaw, S.E., Hammerstrom, J.M., 2003. Cretaceous plutons of the Peninsular Ranges batholith, San Diego and westernmost Imperial Counties, California: Intrusion across a Lake Jurassic continental margin. Geol. Soc. Am. Special Pa, 185–235. doi:10.1130/0-8137-2374-4.185

Tonarini, S., Dini, A., Pezzotta, F., Leeman, W.P., 1998. Boron isotopic composition of zoned (schorl-elbaite) tourmalines, Mt. Capanne Li-Cs pegmatites, Elba (Italy). Eur. J. Mineral. 10, 941–951.

Tonarini, S., Forte, C., Petrini, R., Ferrara, G., 2003. Melt/biotite 11B/10B isotopic fractionation and the boron local environment in the structure of volcanic glasses. Geochim. Cosmochim. Acta 67, 1863–1873. doi:10.1016/S0016-7037(02)00987-0

Trumbull, R.B., Beurlen, H., Wiedenbeck, M., Soares, D.R., 2013. The diversity of B-isotope variations in tourmaline from rare-element pegmatites in the Borborema Province of Brazil. Chem. Geol. 352, 47–62. doi:10.1016/j.chemgeo.2013.05.021

Trumbull, R.B., Chaussidon, M., 1999. Chemical and boron isotopic composition of magmatic and hydrothermal tourmalines from the Sinceni granite-pegmatite system in Swaziland. Chem. Geol. 153, 125–137. doi:10.1016/S0009-2541(98)00155-7

Trumbull, R.B., Krienitz, M.S., Gottesmann, B., Wiedenbeck, M., 2008. Chemical and boron-isotope variations in tourmalines from an S-type granite and its source rocks: The Erongo granite and tourmalinites in the Damara Belt, Namibia. Contrib. to Mineral. Petrol. 155, 1–18. doi:10.1007/s00410-007-0227-3

Trumbull, R.B., Krienitz, M.S., Grundmann, G., Wiedenbeck, M., 2009. Tourmaline geochemistry and δ11B variations as a guide to fluid-rock interaction in the Habachtal emerald deposit, Tauern Window, Austria. Contrib. to Mineral. Petrol. 157, 411–427. doi:10.1007/s00410-008-0342-9

Tuttle, O.F., Bowen, N.L., 1958. Origin of granite in light of experimental studies in the system NaAlSi3O8-KAlSi3O8-SiO2-H2O. Geol. Soc. Am. Mem. 74.

van Hinsberg, V.J., Marschall, H.R., 2007. Boron isotope and light element sector zoning in tourmaline: Implications for the formation of B-isotopic signatures. Chem. Geol. 238, 141–148. doi:10.1016/j.chemgeo.2006.11.002

van Hinsberg, V.J., Schumacher, J.C., 2009. The geothermobarometric potential of tourmaline, based on experimental and natural data. Am. Mineral. 94, 761–770. doi:10.2138/am.2009.3022

Villaseca, C., Barbero, L., Rogers, G., 1998. Crustal origin of Hercynian peraluminous granitic batholiths of Central Spain: petrological, geochemical amd isotopes (Sr, Nd) contsraints. Lithos 43, 55–79.

Visonà, D., Lombardo, B., 2002. Two-mica and tourmaline leucogranites from the Everest-Makalu region (Nepal - Tibet). Himalayan leucogranite genesis by isobaric heating? Lithos. doi:10.1016/S0024-4937(02)00112-3

Walawender, M.J., Gastil, R.G., Clinkenbeard, J.P., Mccormick, W. V, Eastman, B.G., Wernicke, R.S., Wardlaw, M.S., Gunn, S.H., Smith, B.M., 1990. Origin and evolution of the zoned La Posta-type plutons, easter Peninsular Ranges batholith,

southern and Baja California. Geol. North Am. Mem. 174 1–18.

Watson, E.B., Müller, T., 2009. Non-equilibrium isotopic and elemental fractionation during diffusion-controlled crystal growth under static and dynamic conditions. Chem. Geol. 267, 111–124.

White, A.J.R., Allen, C.M., Beams, S.D., Carr, P.F., Champion, D.C., Chappell, B.W., Wyborn, D., Wyborn, L.A.I., 2001. Granite suites and supersuites of Eastern Australia. Aust. J. Earth Sci. 48, 515–530. doi:10.1046/j.1440-0952.2001.00874.x

White, W.M., 2013. Geochemistry. Wiley-Blackwell.

Whitney, D.L., Evans, B.W., 2010. Abbreviations for names of rock-forming minerals. Am. Mineral. 95, 185–187.

Williams, L.B., Hervig, R.L., Holloway, J.R., Hutcheon, I., 2001a. Boron isotope geochemistry during diagenesis. Part I. Experimental determination of fractionation during illitization of smectite. Geochim. Cosmochim. Acta 65, 1769–1782. doi:10.1016/S0016-7037(01)00557-9

Williams, L.B., Hervig, R.L., Hutcheon, I., 2001b. Boron isotope geochemistry during diagenesis. Part II. Applications to organic-rich sediments. Geochim. Cosmochim. Acta 65, 1783–1794. doi:10.1016/S0016-7037(01)00558-0

Wohletz, K., 2013. KWare HEAT3D software. Los Alamos Nat. Lab., Open File Progr. LA-CC 99-2.

Wolf, M.B., London, D., 1997. Boron in granitic magmas: stability of tourmaline in equilibrium with biotite and cordierite. Contrib. to Mineral. Petrol. 130, 12–30. doi:10.1007/s004100050346

Wolf, M.B., London, D., Morgan, G.B., 1994. Effects of boron on the solubility of cassiterite and tantalite in granitic liquids, in: Geological Society of America Abstracts with Programs.

Wu, J., Potuzak, M., Stebbins, J.F., 2011. High-temperature in situ 11B NMR study of network dynamics in boron-containing glass-forming liquids. J. Non. Cryst. Solids 357, 3944–3951. doi:10.1016/j.jnoncrysol.2011.08.013

Wu, J., Stebbins, J.F., 2013. Temperature and modifier cation field strength effects on aluminoborosilicate glass network structure. J. Non. Cryst. Solids 362, 73–81. doi:10.1016/j.jnoncrysol.2012.11.005

Wu, J., Stebbins, J.F., 2010. Quench rate and temperature effects on boron coordination in aluminoborosilicate melts. J. Non. Cryst. Solids 356, 2097–2108. doi:10.1016/j.jnoncrysol.2010.08.015

Wu, J., Stebbins, J.F., 2009. Effects of cation field strength on the structure of aluminoborosilicate glasses: High-resolution 11B, 27Al and 23Na MAS NMR. J. Non. Cryst. Solids 355, 556–562. doi:10.1016/j.jnoncrysol.2009.01.025

Wunder, B., Meixner, A., Romer, R.L., Wirth, R., Heinrich, W., 2005. The geochemical cycle of boron: Constraints from boron isotope partitioning experiments between mica and fluid. Lithos 84, 206–216. doi:10.1016/j.lithos.2005.02.003

Xiao, J., Xiao, Y., Jin, Z., He, M., Liu, C., Xiao, Y., Jin, Z., Liu, C., 2013. Boron isotope variations and its geochemical application in nature. Aust. J. Earth Sci. An Int. Geosci. J. Geol. Soc. Aust. 604. doi:10.1080/08120099.2013.813585

Xue, X., Kanzaki, M., 2007. Al coordination and water speciation in hydrous aluminosilicate glasses: Direct evidence from high-resolution heteronuclear 1H-27Al correlation NMR. Solid State Nucl. Magn. Reson. 31, 10–27. doi:10.1016/j.ssnmr.2006.11.001

Yang, S.Y., Jiang, S.Y., Palmer, M.R., 2015. Chemical and boron isotopic compositions of tourmaline from the Nyalam leucogranites, South Tibetan Himalaya: Implication for their formation from B-rich melt to hydrothermal fluids. Chem. Geol. 419, 102–113. doi:10.1016/j.chemgeo.2015.10.026

Appendix 1: Chemical and boron isotopic compositions of tourmaline, and other minerals, from the Main, Swamp, and Spessartine dikes of the Little Three pegmatite mine

Pegmatite	Main Dike		Main Dike		Main Dike	
Mineral	Tourmaline		Tourmaline		Tourmaline	
Sample ID	2		3		4	
Location	Massive Aplite		Massive Aplite		Massive Aplite	
HAB	3		9		30	
SIMS data						
$\delta^{11}B$	6.4		4.5		5.7	
2σSD	0.9		1.5		---	
N	3		4		1	
EMPA data						
SiO_2	34.30	0.73	35.69	0.47	35.78	0.20
TiO_2	0.12	0.12	0.27	0.12	0.24	0.09
Al_2O_3	33.92	0.35	33.56	0.96	33.60	0.86
FeO	12.26	0.30	13.38	0.88	13.07	0.86
MnO	0.14	0.02	0.19	0.03	0.18	0.03
MgO	2.32	0.06	2.76	0.19	2.73	0.21
CaO	0.18	0.06	0.24	0.04	0.24	0.03
Na_2O	1.66	0.12	2.01	0.11	1.99	0.12
K_2O	0.04	0.01	0.05	0.10	0.05	0.00
B_2O_3	10.27	0.25	---		---	
F	0.00	0.00	0.18	0.03	0.18	0.03
O=F	0.00		-0.07		-0.08	
Total	95.22	0.91	88.24	0.65	87.99	0.25
N	15		296		176	
	Atoms on 24.5 anions basis w/o B and 29 w/ B					
Si	5.819		5.865		5.883	
Ti	0.016		0.033		0.029	
Al	6.783		6.501		6.513	
Fe	1.740		1.839		1.797	
Mn	0.020		0.026		0.025	
Mg	0.586		0.675		0.669	
Ca	0.032		0.042		0.042	
Na	0.547		0.642		0.636	
K	0.009		0.010		0.010	
B			---		---	
F	0.000		0.092		0.096	
Sum	15.552		15.632		15.606	
Schorl (Srl)	35.01		43.95		42.61	
Dravite (Drv)	11.70		15.87		15.61	
Uvite (Uvt)	0.82		1.12		1.12	
Feruvite (Fuv)	2.45		3.11		3.05	
Foitite (Ftt)	31.56		23.21		22.84	
Mg-Foitite (Mft)	10.55		8.38		8.36	
Olenite (Oln)	7.23		3.48		5.57	
Tsilaisite (Tsl)	0.67		0.88		0.84	
Liddicoatite (Ldd)	---		---		---	
Elbaite (Elb)	---		---		---	
Rossmanite (Rss)	---		---		---	
Li Calc	---		---		---	

HAB: Height Above Base of pegmatite (cm)

CMP: EMPA data from Morgan and London (1999), Contributions to Mineralogy and Petrology

CanMin: EMPA data from London et al. (2012), The Canadian Mineralogist

Tourmaline components calculated using the Excel™ spreadsheet of Morgan (2016)

Pegmatite	Main Dike		Main Dike		Main Dike		Main Dike	
Mineral	Tourmaline		Tourmaline		Tourmaline		Tourmaline	
Sample ID	5c		5d		5e		5f	
Location	Layered Aplite		Layered Aplite		Layered Aplite		Layered Aplite	
HAB	52		58		62		68	
SIMS data								
$\delta^{11}B$	3.6		3.5		2.1		2.0	
2σSD	1.3		2.0		1.6		6.1	
N	3		2		3		3	
EMPA data							CMP	
SiO_2	35.59	0.19	35.65	0.19	35.31	0.34	35.60	0.25
TiO_2	0.22	0.04	0.22	0.04	0.24	0.05	0.24	0.07
Al_2O_3	34.72	0.27	34.53	0.26	34.79	0.25	34.60	0.38
FeO	13.57	0.25	13.30	0.31	13.65	0.26	13.62	0.40
MnO	0.18	0.08	0.18	0.01	0.19	0.02	0.18	0.02
MgO	1.85	0.11	1.70	0.13	1.58	0.19	1.60	0.24
CaO	0.22	0.03	0.22	0.03	0.22	0.03	0.21	0.04
Na_2O	1.81	0.05	1.74	0.06	1.75	0.06	1.72	0.08
K_2O	0.05	0.00	0.05	0.01	0.05	0.01	0.06	0.06
B_2O_3	---		---		---		---	
F	0.11	0.03	0.11	0.03	0.12	0.03	0.13	0.04
O=F	-0.05		-0.05		-0.05		-0.05	
Total	88.27	0.27	87.65	0.36	87.85	0.35	87.90	0.34
N	162		179		247		301	
Si	5.839		5.877		5.822		5.862	
Ti	0.027		0.028		0.030		0.029	
Al	6.713		6.709		6.761		6.715	
Fe	1.861		1.834		1.882		1.875	
Mn	0.025		0.025		0.026		0.026	
Mg	0.452		0.418		0.389		0.393	
Ca	0.038		0.039		0.039		0.036	
Na	0.577		0.557		0.560		0.549	
K	0.010		0.010		0.010		0.012	
B	---		---		---		---	
F	0.057		0.059		0.064		0.066	
Sum	15.543		15.495		15.520		15.498	
Schorl (Srl)	39.70		37.42		38.87		38.21	
Dravite (Drv)	9.50		8.40		7.91		7.89	
Uvite (Uvt)	0.74		0.71		0.66		0.62	
Feruvite (Fuv)	3.10		3.16		3.23		3.02	
Foitite (Ftt)	30.22		32.20		32.45		33.40	
Mg-Foitite (Mft)	7.23		7.23		6.60		6.90	
Olenite (Oln)	8.67		10.07		9.40		9.11	
Tsilaisite (Tsl)	0.84		0.82		0.87		0.85	
Liddicoatite (Ldd)	---		---		---		---	
Elbaite (Elb)	---		---		---		---	
Rossmanite (Rss)	---		---		---		---	
Li Calc	---		---		---		---	

HAB: Height Above Base of pegmatite (cm)

CMP: EMPA data from Morgan and London (1999), Contributions to Mineralogy and Petrology

CanMin: EMPA data from London et al. (2012), The Canadian Mineralogist

Tourmaline components calculated using the Excel™ spreadsheet of Morgan (2016)

Pegmatite	Main Dike		Main Dike		Main Dike		Main Dike	
Mineral	Tourmaline		Tourmaline		Tourmaline		Tourmaline	
Sample ID	6a		6b		6c		6d	
Location	Layered Aplite		Layered Aplite		Layered Aplite		Layered Aplite	
HAB	75		79		84		88	
SIMS data								
$\delta^{11}B$	4.7		5.2		4.7		5.4	
2σSD	1.8		0.2		1.4		1.4	
N	2		2		2		4	
EMPA data							CMP	
SiO_2	35.12	0.37	35.81	0.33	35.61	0.43	35.42	0.28
TiO_2	0.22	0.06	0.19	0.07	0.19	0.08	0.21	0.06
Al_2O_3	34.84	0.31	34.43	0.33	34.66	0.48	34.75	0.40
FeO	13.85	0.48	13.36	0.33	14.06	0.44	14.43	0.37
MnO	0.19	0.02	0.17	0.02	0.21	0.02	0.25	0.03
MgO	1.61	0.29	1.83	0.20	1.47	0.25	1.13	0.28
CaO	0.19	0.04	0.19	0.04	0.19	0.04	0.17	0.04
Na_2O	1.72	0.07	1.75	0.09	1.79	0.08	1.75	0.09
K_2O	0.05	0.01	0.04	0.01	0.05	0.01	0.05	0.01
B_2O_3	---		---		---		---	
F	0.13	0.04	0.13	0.05	0.16	0.06	0.14	0.04
O=F	-0.05		-0.05		-0.07		-0.06	
Total	87.86	0.20	87.85	0.38	88.32	0.31	88.22	0.30
N	346		197		149		308	
Si	5.797		5.891		5.850		5.837	
Ti	0.027		0.023		0.023		0.026	
Al	6.780		6.675		6.712		6.750	
Fe	1.912		1.838		1.931		1.989	
Mn	0.026		0.024		0.030		0.035	
Mg	0.395		0.450		0.359		0.276	
Ca	0.034		0.033		0.034		0.030	
Na	0.550		0.557		0.570		0.558	
K	0.011		0.009		0.010		0.010	
B	---		---		---		---	
F	0.067		0.066		0.085		0.072	
Sum	15.533		15.499		15.518		15.510	
Schorl (Srl)	39.35		37.89		40.55		40.96	
Dravite (Drv)	8.02		9.16		7.46		5.62	
Uvite (Uvt)	0.58		0.64		0.52		0.36	
Feruvite (Fuv)	2.86		2.63		2.85		2.60	
Foitite (Ftt)	33.62		32.26		32.63		35.41	
Mg-Foitite (Mft)	6.86		7.80		6.00		4.86	
Olenite (Oln)	7.82		8.83		9.00		9.04	
Tsilaisite (Tsl)	0.88		0.80		0.99		1.16	
Liddicoatite (Ldd)	---		---		---		---	
Elbaite (Elb)	---		---		---		---	
Rossmanite (Rss)	---		---		---		---	
Li Calc	---		---		---		---	

HAB: Height Above Base of pegmatite (cm)

CMP: EMPA data from Morgan and London (1999), Contributions to Mineralogy and Petrology

CanMin: EMPA data from London et al. (2012), The Canadian Mineralogist

Tourmaline components calculated using the Excel™ spreadsheet of Morgan (2016)

Pegmatite	Main Dike		Main Dike		Main Dike	
Mineral	Tourmaline		Tourmaline		Tourmaline	
Sample ID	6e		6f		6g	
Location	Layered Aplite		Lower Intermediate Zone		Lower Intermediate Zone	
HAB	92		96		100	
SIMS data						
$\delta^{11}B$	6.4		5.3		3.9	
2σSD	1.7		1.3		2.9	
N	6		2		2	
EMPA data					CMP	
SiO_2	35.32	0.19	34.98	0.41	35.22	0.99
TiO_2	0.20	0.04	0.16	0.06	0.10	0.02
Al_2O_3	35.27	0.29	35.55	0.43	34.84	0.24
FeO	14.60	0.27	14.43	0.35	14.13	0.15
MnO	0.33	0.04	0.42	0.03	0.36	0.02
MgO	0.65	0.13	0.34	0.09	0.43	0.02
CaO	0.12	0.02	0.08	0.02	0.05	0.01
Na_2O	1.69	0.06	1.60	0.07	1.41	0.03
K_2O	0.04	0.01	0.04	0.01	0.03	0.01
B_2O_3	---		---		10.80	0.35
F	0.16	0.04	0.15	0.03	0.00	0.00
O=F	-0.07		-0.06		0.00	
Total	88.31	0.25	87.69	0.37	97.36	1.26
N	222		103		25	
Si	5.816		5.795		5.895	
Ti	0.024		0.020		0.012	
Al	6.845		6.941		6.873	
Fe	2.010		1.999		1.977	
Mn	0.046		0.059		0.051	
Mg	0.161		0.085		0.106	
Ca	0.021		0.015		0.009	
Na	0.538		0.513		0.458	
K	0.009		0.009		0.007	
B	---		---			
F	0.084		0.080		0.000	
Sum	15.469		15.435		15.389	
Schorl (Srl)	39.19		36.21		32.17	
Dravite (Drv)	3.09		1.52		1.72	
Uvite (Uvt)	0.15		0.06		0.05	
Feruvite (Fuv)	1.93		1.41		0.87	
Foitite (Ftt)	40.06		44.49		49.91	
Mg-Foitite (Mft)	3.16		1.87		2.67	
Olenite (Oln)	10.89		12.46		10.91	
Tsilaisite (Tsl)	1.52		1.97		1.69	
Liddicoatite (Ldd)	---		---		---	
Elbaite (Elb)	---		---		---	
Rossmanite (Rss)	---		---		---	
Li Calc	---		---		---	

HAB: Height Above Base of pegmatite (cm)

CMP: EMPA data from Morgan and London (1999), Contributions to Mineralogy and Petrology

CanMin: EMPA data from London et al. (2012), The Canadian Mineralogist

Tourmaline components calculated using the Excel™ spreadsheet of Morgan (2016)

Pegmatite	Main Dike		Main Dike		Main Dike	
Mineral	Tourmaline		Tourmaline		Tourmaline	
Sample ID	Elbaite 1 (green/light green)		Elbaite 2 (green)		Elbaite 2 (light green)	
Location	Pocket		Pocket		Pocket	
HAB	100-135		100-135		100-135	
SIMS data						
$\delta^{11}B$	1.0		3.5		3.2	
2σSD	1.0		2.0		1.8	
N	7		2		2	
EMPA data	CanMin					
SiO_2	36.76	0.03	36.19	0.94	36.97	0.79
TiO_2	0.18	0.01	0.13	0.01	0.20	0.01
Al_2O_3	39.43	0.16	38.81	0.17	38.02	0.15
FeO	0.01	0.01	0.55	0.03	0.01	0.01
MnO	6.02	0.09	6.08	0.08	5.90	0.06
MgO	0.11	0.02	0.00	0.00	0.00	0.00
CaO	0.10	0.01	0.06	0.01	0.10	0.01
Na_2O	2.79	0.05	2.31	0.05	2.61	0.03
K_2O	---		0.02	0.01	0.03	0.01
B_2O_3	---		7.06	0.23	7.51	0.34
F	1.57	0.13	0.99	0.07	1.42	0.01
O=F	-0.66		-0.42		-0.60	
Total	86.31		91.78	1.10	92.18	0.83
N	35		10		10	
Si	5.845		5.884		5.983	
Ti	0.022		0.015		0.025	
Al	7.390		7.438		7.253	
Fe	0.001		0.074		0.002	
Mn	0.811		0.837		0.809	
Mg	0.026		0.001		0.001	
Ca	0.017		0.010		0.018	
Na	0.860		0.729		0.818	
K	0.000		0.004		0.006	
B	---					
F	0.790		0.510		0.724	
Sum	14.973		14.993		14.915	
Schorl (Srl)	---		---		---	
Dravite (Drv)	---		---		---	
Uvite (Uvt)	---		---		---	
Feruvite (Fuv)	---		---		---	
Foitite (Ftt)	1.16		4.58		1.30	
Mg-Foitite (Mft)	1.32		---		---	
Olenite (Oln)	22.95		20.69		14.70	
Tsilaisite (Tsl)	27.47		28.21		27.37	
Liddicoatite (Ldd)	1.73		1.06		1.76	
Elbaite (Elb)	37.02		24.70		41.08	
Rossmanite (Rss)	8.35		20.76		13.78	
Li Calc	0.67		0.60		0.79	

HAB: Height Above Base of pegmatite (cm)

CMP: EMPA data from Morgan and London (1999), Contributions to Mineralogy and Petrology

CanMin: EMPA data from London et al. (2012), The Canadian Mineralogist

Tourmaline components calculated using the Excel™ spreadsheet of Morgan (2016)

Pegmatite	Main Dike		Main Dike		Main Dike	
Mineral	Tourmaline		Tourmaline		Tourmaline	
Sample ID	Elbaite 2 (pink)		7c		7b	
Location	Pocket		Upper Intermediate Zone		Upper Intermediate Zone	
HAB	100-135		140		145	
SIMS data						
$\delta^{11}B$	2.5		2.0		5.9	
2σSD	0.4		2.0		0.0	
N	2		2		1	
EMPA data						
SiO_2	36.68	1.03	36.02	0.84	34.45	0.65
TiO_2	0.08	0.01	0.12	0.01	0.07	0.01
Al_2O_3	38.03	0.71	38.20	0.09	36.90	0.21
FeO	0.17	0.29	0.02	0.01	5.95	0.07
MnO	6.91	0.20	7.09	0.05	4.53	0.05
MgO	0.00	0.01	0.01	0.01	0.00	0.00
CaO	0.05	0.02	0.11	0.00	0.02	0.01
Na_2O	2.49	0.23	2.56	0.04	1.58	0.04
K_2O	0.02	0.01	0.03	0.00	0.02	0.01
B_2O_3	7.38	0.25	7.20	0.24	8.69	0.28
F	1.19	0.26	1.30	0.02	0.48	0.01
O=F	-0.50		-0.55		-0.20	
Total	92.50	1.21	92.11	0.81	92.50	0.79
N	10		10		10	
Si	5.949		5.865		5.805	
Ti	0.010		0.015		0.009	
Al	7.270		7.331		7.329	
Fe	0.023		0.003		0.839	
Mn	0.949		0.978		0.647	
Mg	0.001		0.002		0.001	
Ca	0.008		0.020		0.003	
Na	0.783		0.810		0.518	
K	0.004		0.005		0.004	
B						
F	0.608		0.670		0.253	
Sum	14.996		15.027		15.155	
Schorl (Srl)	---		---		---	
Dravite (Drv)	---		---		---	
Uvite (Uvt)	---		---		---	
Feruvite (Fuv)	---		---		---	
Foitite (Ftt)	1.66		0.88		42.60	
Mg-Foitite (Mft)	---		0.12		---	
Olenite (Oln)	17.61		21.04		14.62	
Tsilaisite (Tsl)	32.04		33.05		21.67	
Liddicoatite (Ldd)	0.88		1.95		0.36	
Elbaite (Elb)	29.64		27.86		15.62	
Rossmanite (Rss)	18.17		15.10		5.14	
Li Calc	0.64		0.61		0.29	

HAB: Height Above Base of pegmatite (cm)

CMP: EMPA data from Morgan and London (1999), Contributions to Mineralogy and Petrology

CanMin: EMPA data from London et al. (2012), The Canadian Mineralogist

Tourmaline components calculated using the Excel™ spreadsheet of Morgan (2016)

Pegmatite	Main Dike		Main Dike	
Mineral	Tourmaline		Tourmaline	
Sample ID	7a		8	
Location	Upper Intermediate Zone		Upper Intermediate Zone	
HAB	150		150	
SIMS data				
$\delta^{11}B$	6.0		5.2	
2σSD	0.1		0.3	
N	2		5	
EMPA data				
SiO_2	34.88	0.79	34.69	0.37
TiO_2	0.09	0.02	0.10	0.00
Al_2O_3	36.42	0.42	33.88	0.24
FeO	8.41	0.48	12.79	0.17
MnO	2.99	0.16	0.18	0.00
MgO	0.00	0.01	1.88	0.02
CaO	0.03	0.01	0.12	0.00
Na_2O	1.71	0.37	1.52	0.03
K_2O	0.02	0.01	0.03	0.01
B_2O_3	9.20	0.26	10.11	0.31
F	0.51	0.30	0.00	0.00
O=F	-0.21		0.00	
Total	94.04	1.11	95.32	0.78
N	10		3	
Si	5.839		5.853	
Ti	0.011		0.031	
Al	7.186		6.685	
Fe	1.178		1.911	
Mn	0.423		0.028	
Mg	0.001		0.408	
Ca	0.005		0.034	
Na	0.554		0.567	
K	0.005		0.010	
B				
F	0.268		0.071	
Sum	15.202		15.527	
Schorl (Srl)	10.75		33.72	
Dravite (Drv)	---		8.77	
Uvite (Uvt)	---		0.45	
Feruvite (Fuv)	---		1.73	
Foitite (Ftt)	43.64		38.02	
Mg-Foitite (Mft)	---		9.89	
Olenite (Oln)	12.87		6.55	
Tsilaisite (Tsl)	14.21		0.86	
Liddicoatite (Ldd)	0.54		---	
Elbaite (Elb)	17.98		---	
Rossmanite (Rss)	---		---	
Li Calc	0.28		---	

HAB: Height Above Base of pegmatite (cm)

CMP: EMPA data from Morgan and London (1999), Contributions to Mineralogy and Petrology

CanMin: EMPA data from London et al. (2012), The Canadian Mineralogist

Tourmaline components calculated using the Excel™ spreadsheet of Morgan (2016)

Pegmatite	Swamp Dike		Swamp Dike		Swamp Dike	
Mineral	Tourmaline		Tourmaline		Tourmaline	
Sample ID	KD1		KD2		KD3	
Location	Lower graphic		Massive aplite		Layered aplite	
HAB	3.5		10		15.5	
SIMS data						
$\delta^{11}B$	4.7		6.5		6.2	
2σSD	1.9		0.8		0.1	
N	2		4		2	
EMPA data						
SiO_2	33.90	0.65	34.49	0.70	34.17	0.78
TiO_2	0.41	0.03	0.11	0.03	0.24	0.09
Al_2O_3	33.48	0.62	35.05	0.25	35.04	0.26
FeO	13.23	0.28	12.97	0.14	13.22	0.28
MnO	0.16	0.02	0.15	0.01	0.18	0.03
MgO	2.95	0.10	1.85	0.02	1.76	0.10
CaO	0.34	0.02	0.12	0.02	0.18	0.05
Na_2O	2.18	0.07	1.64	0.02	1.82	0.09
K_2O	0.06	0.01	0.04	0.00	0.04	0.00
B_2O_3	11.13	0.24	11.24	0.22	11.49	0.33
F	0.02	0.03	0.00	0.00	0.00	0.00
O=F	-0.01		0.00		0.00	
Total	97.85	0.91	97.66	1.04	98.15	0.67
N	5		5		5	
	Atoms on 29 anions basis					
Si	5.632		5.694		5.623	
Ti	0.051		0.014		0.030	
Al	6.557		6.819		6.797	
Fe	1.838		1.790		1.819	
Mn	0.022		0.021		0.025	
Mg	0.730		0.454		0.432	
Ca	0.060		0.021		0.031	
Na	0.702		0.524		0.581	
K	0.013		0.008		0.009	
B	3.190		3.202		3.264	
F	0.011		0.000		0.000	
Sum	18.795		18.548		18.611	
Schorl (Srl)	47.83		34.70		38.67	
Dravite (Drv)	18.49		8.73		9.02	
Uvite (Uvt)	1.67		0.42		0.59	
Feruvite (Fuv)	4.31		1.67		2.52	
Foitite (Ftt)	16.23		35.67		30.68	
Mg-Foitite (Mft)	6.27		8.98		7.16	
Olenite (Oln)	4.47		9.15		10.54	
Tsilaisite (Tsl)	0.73		0.68		0.82	
Liddicoatite (Ldd)	---		---		---	
Elbaite (Elb)	---		---		---	
Rossmanite (Rss)	---		---		---	
Li Calc	---		---		---	

HAB: Height Above Base of pegmatite (cm)

CMP: EMPA data from Morgan and London (1999), Contributions to Mineralogy and Petrology

CanMin: EMPA data from London et al. (2012), The Canadian Mineralogist

Tourmaline components calculated using the Excel™ spreadsheet of Morgan (2016)

Pegmatite	Swamp Dike		Swamp Dike		Swamp Dike		Swamp Dike	
Mineral	Tourmaline		Tourmaline		Tourmaline		Tourmaline	
Sample ID	KD4		KD5		KD6		KD7	
Location	Layered aplite		Layered aplite		Layered aplite		Layered aplite	
HAB	17		19		20.5		22	
SIMS data								
$\delta^{11}B$	6.4		7.5		4.6		6.5	
2σSD	2.6		0.7		1.1		0.1	
N	2		2		2		2	
EMPA data								
SiO_2	33.75	0.71	35.14	0.52	34.25	0.71	33.54	0.45
TiO_2	0.33	0.02	0.11	0.04	0.28	0.05	0.32	0.02
Al_2O_3	35.09	0.29	35.85	0.26	34.25	0.27	35.00	0.39
FeO	13.49	0.38	13.21	0.09	13.71	0.09	13.88	0.13
MnO	0.17	0.01	0.20	0.01	0.17	0.01	0.20	0.01
MgO	1.69	0.08	1.33	0.03	1.79	0.17	1.42	0.11
CaO	0.23	0.02	0.11	0.01	0.26	0.03	0.22	0.02
Na_2O	1.84	0.08	1.55	0.02	1.89	0.06	1.79	0.08
K_2O	0.04	0.01	0.03	0.01	0.05	0.01	0.05	0.01
B_2O_3	11.52	0.18	11.47	0.31	11.40	0.22	11.56	0.36
F	0.03	0.04	0.00	0.00	0.02	0.04	0.00	0.00
O=F	-0.01		0.00		-0.01		0.00	
Total	98.18	0.91	99.02	0.93	98.06	0.91	97.98	0.34
N	5		5		5		5	
Si	5.564		5.712		5.661		5.550	
Ti	0.041		0.014		0.034		0.039	
Al	6.819		6.870		6.673		6.826	
Fe	1.860		1.796		1.896		1.921	
Mn	0.023		0.028		0.024		0.028	
Mg	0.415		0.323		0.441		0.350	
Ca	0.041		0.019		0.046		0.040	
Na	0.587		0.490		0.605		0.573	
K	0.009		0.007		0.010		0.010	
B	3.277		3.218		3.253		3.300	
F	0.017		0.000		0.012		0.000	
Sum	18.636		18.478		18.643		18.639	
Schorl (Srl)	40.16		31.35		42.21		40.65	
Dravite (Drv)	8.77		5.60		9.65		7.26	
Uvite (Uvt)	0.73		0.29		0.86		0.60	
Feruvite (Fuv)	3.35		1.61		3.77		3.38	
Foitite (Ftt)	29.80		41.06		27.53		31.98	
Mg-Foitite (Mft)	6.51		7.34		6.29		5.71	
Olenite (Oln)	9.91		11.82		8.90		9.47	
Tsilaisite (Tsl)	0.78		0.93		0.78		0.95	
Liddicoatite (Ldd)	---		---		---		---	
Elbaite (Elb)	---		---		---		---	
Rossmanite (Rss)	---		---		---		---	
Li Calc	---		---		---		---	

HAB: Height Above Base of pegmatite (cm)

CMP: EMPA data from Morgan and London (1999), Contributions to Mineralogy and Petrology

CanMin: EMPA data from London et al. (2012), The Canadian Mineralogist

Tourmaline components calculated using the Excel™ spreadsheet of Morgan (2016)

Pegmatite	Swamp Dike		Swamp Dike		Swamp Dike	
Mineral	Tourmaline		Tourmaline		Tourmaline	
Sample ID	KD8		KD9		KD10	
Location	Layered aplite		Lower Intermediate Zone		Lower Intermediate Zone	
HAB	23		25		29	
SIMS data						
$\delta^{11}B$	6.4		1.6		1.5	
2σSD	0.6		1.4		0.8	
N	2		4		4	
EMPA data						
SiO_2	34.30	0.76	33.58	0.63	33.18	1.02
TiO_2	0.27	0.02	0.10	0.01	0.27	0.01
Al_2O_3	34.63	0.24	35.23	0.21	35.28	0.22
FeO	14.04	0.19	14.37	0.11	14.14	0.11
MnO	0.21	0.02	0.38	0.01	0.66	0.04
MgO	1.56	0.12	0.43	0.02	0.10	0.01
CaO	0.21	0.03	0.06	0.00	0.06	0.01
Na_2O	1.90	0.02	1.53	0.01	1.65	0.05
K_2O	0.05	0.00	0.03	0.00	0.04	0.00
B_2O_3	11.33	0.34	11.09	0.31	10.94	0.27
F	0.00	0.00	0.00	0.00	0.03	0.01
O=F	0.00		0.00		-0.01	
Total	98.49	0.95	96.81	0.88	96.35	1.24
N	5		5		5	
Si	5.655		5.634		5.603	
Ti	0.033		0.013		0.034	
Al	6.731		6.966		7.021	
Fe	1.936		2.016		1.997	
Mn	0.030		0.053		0.095	
Mg	0.382		0.107		0.026	
Ca	0.037		0.011		0.012	
Na	0.607		0.498		0.540	
K	0.010		0.007		0.008	
B	3.224		3.211		3.189	
F	0.000		0.000		0.015	
Sum	18.644		18.517		18.524	
Schorl (Srl)	43.21		35.98		37.57	
Dravite (Drv)	8.39		1.89		0.48	
Uvite (Uvt)	0.60		0.05		0.01	
Feruvite (Fuv)	3.07		1.03		1.14	
Foitite (Ftt)	29.00		45.93		43.50	
Mg-Foitite (Mft)	5.63		2.42		0.55	
Olenite (Oln)	9.10		10.91		13.59	
Tsilaisite (Tsl)	1.00		1.78		3.15	
Liddicoatite (Ldd)	---		---		---	
Elbaite (Elb)	---		---		---	
Rossmanite (Rss)	---		---		---	
Li Calc	---		---		---	

HAB: Height Above Base of pegmatite (cm)

CMP: EMPA data from Morgan and London (1999), Contributions to Mineralogy and Petrology

CanMin: EMPA data from London et al. (2012), The Canadian Mineralogist

Tourmaline components calculated using the Excel™ spreadsheet of Morgan (2016)

Pegmatite	Swamp Dike		Swamp Dike		Swamp Dike	
Mineral	Tourmaline		Tourmaline		Tourmaline	
Sample ID	Black Tourmaline		KD11		KD12	
Location	Pocket		Upper Intermediate Zone		Upper Intermediate Zone	
HAB	30-35		36		38	
SIMS data						
$\delta^{11}B$	6.7		2.0		1.6	
2σSD	2.8		0.8		3.5	
N	3		4		4	
EMPA data						
SiO_2	32.96	0.76	32.81	1.33	33.45	0.24
TiO_2	0.34	0.02	0.13	0.01	0.43	0.03
Al_2O_3	33.08	0.20	34.50	0.24	33.19	0.15
FeO	14.96	0.26	14.35	0.11	12.26	0.21
MnO	1.09	0.07	0.26	0.03	0.14	0.02
MgO	0.20	0.02	0.82	0.02	3.16	0.14
CaO	0.11	0.01	0.08	0.01	0.32	0.02
Na_2O	1.88	0.03	1.64	0.05	2.11	0.06
K_2O	0.05	0.01	0.04	0.01	0.06	0.00
B_2O_3	10.76	0.33	11.42	0.40	11.22	0.28
F	0.09	0.01	0.00	0.00	0.05	0.08
O=F	-0.04		0.00		-0.02	
Total	95.47	1.00	96.05	1.71	96.38	0.29
N	5		5		5	
Si	5.669		5.548		5.611	
Ti	0.044		0.017		0.055	
Al	6.729		6.875		6.563	
Fe	2.159		2.029		1.720	
Mn	0.159		0.037		0.020	
Mg	0.051		0.207		0.790	
Ca	0.020		0.014		0.058	
Na	0.629		0.537		0.686	
K	0.011		0.009		0.012	
B	3.205		3.333		3.249	
F	0.049		0.000		0.026	
Sum	18.725		18.605		18.764	
Schorl (Srl)	49.34		40.30		43.87	
Dravite (Drv)	1.15		4.08		19.54	
Uvite (Uvt)	0.05		0.13		1.79	
Feruvite (Fuv)	1.99		1.25		4.01	
Foitite (Ftt)	33.18		39.93		16.92	
Mg-Foitite (Mft)	0.77		4.04		7.53	
Olenite (Oln)	8.21		9.04		5.69	
Tsilaisite (Tsl)	5.31		1.23		0.65	
Liddicoatite (Ldd)	---		---		---	
Elbaite (Elb)	---		---		---	
Rossmanite (Rss)	---		---		---	
Li Calc	---		---		---	

HAB: Height Above Base of pegmatite (cm)

CMP: EMPA data from Morgan and London (1999), Contributions to Mineralogy and Petrology

CanMin: EMPA data from London et al. (2012), The Canadian Mineralogist

Tourmaline components calculated using the Excel™ spreadsheet of Morgan (2016)

Pegmatite	Spessartine Dike		Spessartine Dike		Spessartine Dike	
Mineral	Tourmaline		Tourmaline		Tourmaline	
Sample ID	Herc		LT3core		LT3pen	
Location	Intermediate Zone		Pocket		Pocket	
HAB						
SIMS data						
$\delta^{11}B$	4.6		5.7		5.8	
2σSD	1.8		0.6		1.2	
N	3		3		4	
EMPA data						
SiO_2	33.97	0.95	34.39	0.29	35.52	0.34
TiO_2	0.17	0.01	0.09	0.10	0.38	0.19
Al_2O_3	36.54	0.22	34.75	0.16	34.10	1.46
FeO	13.37	0.03	14.21	0.36	9.07	0.50
MnO	1.07	0.02	0.46	0.08	0.56	0.16
MgO	0.04	0.00	0.31	0.33	4.52	0.84
CaO	0.04	0.00	0.02	0.03	0.68	0.35
Na_2O	1.61	0.02	1.52	0.07	1.85	0.25
K_2O	0.04	0.00	---		---	
B_2O_3	---		---		---	
F	0.06	0.01	---		---	
O=F	-0.03		---		---	
Total	98.26	0.98	96.61	0.43	97.33	0.36
N	5		50		245	
	Atoms on 24.5 anions basis					
Si	5.674		5.827		5.832	
Ti	0.021		0.011		0.047	
Al	7.194		6.941		6.599	
Fe	1.868		2.014		1.245	
Mn	0.151		0.066		0.078	
Mg	0.010		0.078		1.105	
Ca	0.007		0.004		0.120	
Na	0.521		0.499		0.589	
K	0.009		---		---	
B	---		---		---	
F	0.032		---		---	
Sum	15.455		15.440		15.615	
Schorl (Srl)	31.56		35.26		26.16	
Dravite (Drv)	0.17		1.36		22.39	
Uvite (Uvt)	---		0.01		5.52	
Feruvite (Fuv)	5.05		2.20		2.60	
Foitite (Ftt)	46.04		47.85		15.70	
Mg-Foitite (Mft)	0.71		0.35		6.45	
Olenite (Oln)	16.22		11.12		7.74	
Tsilaisite (Tsl)	0.24		1.85		13.44	
Liddicoatite (Ldd)	---		---		---	
Elbaite (Elb)	---		---		---	
Rossmanite (Rss)	---		---		---	
Li Calc	---		---		---	

HAB: Height Above Base of pegmatite (cm)

CMP: EMPA data from Morgan and London (1999), Contributions to Mineralogy and Petrology

CanMin: EMPA data from London et al. (2012), The Canadian Mineralogist

Tourmaline components calculated using the Excel™ spreadsheet of Morgan (2016)

Pegmatite	Spessartine Dike		Spessartine Dike	
Mineral	Tourmaline		Tourmaline	
Sample ID	TurAx		SD_ExoTur	
Location	Pocket		External	
HAB				
SIMS data				
$\delta^{11}B$	13.8		-0.1	
2σSD	4.5		3.4	
N	3		7	
EMPA data				
SiO_2	34.26	1.02	34.44	0.80
TiO_2	0.13	0.01	1.02	0.33
Al_2O_3	37.33	0.21	34.87	0.47
FeO	8.95	0.11	7.89	0.40
MnO	2.82	0.04	1.47	0.19
MgO	0.02	0.01	2.71	0.25
CaO	0.02	0.01	0.67	0.08
Na_2O	1.52	0.05	2.14	0.05
K_2O	0.03	0.01	0.03	0.01
B_2O_3	---		---	
F	0.29	0.02	0.66	0.06
O=F	-0.12		-0.28	
Total	95.36	1.08	95.55	1.03
N	20		28	
Si	5.726		5.709	
Ti	0.016		0.127	
Al	7.354		6.813	
Fe	1.251		1.094	
Mn	0.399		0.206	
Mg	0.005		0.669	
Ca	0.004		0.119	
Na	0.493		0.688	
K	0.006		0.006	
B	---		---	
F	0.153		0.349	
Sum	15.254		15.431	
Schorl (Srl)	8.85		24.97	
Dravite (Drv)	0.03		13.69	
Uvite (Uvt)	---		4.21	
Feruvite (Fuv)	13.31		6.88	
Foitite (Ftt)	49.55		12.07	
Mg-Foitite (Mft)	0.36		7.69	
Olenite (Oln)	27.70		23.88	
Tsilaisite (Tsl)	0.19		6.62	
Liddicoatite (Ldd)	---		---	
Elbaite (Elb)	---		---	
Rossmanite (Rss)	---		---	
Li Calc	---		---	

HAB: Height Above Base of pegmatite (cm)

CMP: EMPA data from Morgan and London (1999), Contributions to Mineralogy and Petrology

CanMin: EMPA data from London et al. (2012), The Canadian Mineralogist

Tourmaline components calculated using the Excel™ spreadsheet of Morgan (2016)

Appendix 2: Methodology for preparation of starting materials for experiments and details of Rayleigh model

Preparation of starting materials for experiments

The sources of Fe, Mn, and Mg in each starting material mixture are as follows: mixtures GT1.2 and GT1.2+ contained Fe metal and MnO, mixture GT1.3 contained rhodonite (source of Mn), Mn-Fayalite (source of Fe and Mn), and forsterite (source of Mg), and mixture MnGT-BC-4.1 contained almandine (source of Fe and Mg) and spessartine (source of Mn). Mixture GT1.2+ was made by adding 5% quartz, 0.5% MnO, and 2% $Al(OH)_3$, by relative weight, to mixture GT1.2. Each mixture was created by crushing natural minerals in a mortar and pestle and then milling in an agate mortar and pestle in alcohol to a fine powder. Milled powders were placed in an oven at ~120°C for ~15 minutes to dry. Final preparation of each individual mixture involved weighing individual components to attain the target composition, dry milling the combination in an agate mortar and pestle, and storing mixtures in glass vials in a desiccator.

Parameters for Rayleigh model

Calculation of normative mineralogy. Three different normative mineral assemblages were calculated based on the initial composition of the melt inclusions. The normative assemblages are similar in that they all include quartz, orthoclase, and plagioclase, for which the partition coefficients for Mg, Fe, and Mn have been set to zero. The assemblages differ in that the first contains cordierite and biotite, the second contains biotite, and the third contains biotite and muscovite. Biotite is considered a solid-solution of phlogopite-annite in the model. Normative cordierite and biotite for the first assemblage were calculated iteratively by assigning some MnO, FeO, and MgO, and stoichiometric proportions of Al_2O_3, SiO_2, and K_2O, to biotite and the remainder of

the mafic oxides, Al_2O_3, and SiO_2 to cordierite; by this process, the residual normative corundum component approached zero. Normative biotite for the second assemblage was calculated by taking all FeO, MnO, and MgO, plus stoichiometric amounts of K_2O, SiO_2, and Al_2O_3. Since biotite is a phlogopite-annite solid-solution, excess Al_2O_3 is apportioned to aluminosilicate. Normative muscovite and biotite for the third assemblage were calculated by apportioning all MnO, FeO, and MgO, and stoichiometric proportions of K_2O, Al_2O_3, and SiO_2, to biotite; the remaining balance of Al_2O_3 and part of the orthoclase component were converted to form muscovite.

Temperature, bulk distribution coefficients, and crystallization sequence. The ferromagnesian and mica assemblages used in the model change with decreasing temperature. Crystallization of a cordierite-biotite is modeled between 800° and 750°C, referred to as the 1st iteration, a biotite granite between 750° and 700°C, referred to as the 2nd iteration, and a muscovite-biotite granite between 700° and 650°C, referred to as the 3rd iteration. The 1st iteration is modeled between F=1.0 and F=0.8. The resultant concentrations of FeO, MnO, and MgO from the 1st iteration are used as the initial concentrations in the 2nd iteration and to calculate mineral modes. The 2nd and 3rd iterations were modeled from F=1.0 to F=0.375 and from F=1.0 to F=0.0, respectively. The results of the 2nd and 3rd iterations are plotted from F=0.8 to F=0.3 and from F=0.3 to F=0.0, respectively, in Figure 5-9. The composition of the liquid at F=0.375 in the 2nd iteration was used as the starting composition and as the basis for calculating mineral modes for the 3rd iteration. Liquid fractions (F values) for each iteration were chosen such as to increase the effects of micas relative to cordierite, consistent with field observations (e.g. Villaseca et al. 1998). Lastly, the partition coefficients were varied

continuously and linearly over the temperature interval, as determined by the experiments in this study (refer to Table 7 for a list of Rayleigh parameters).

Caveats regarding the results of the Rayleigh model

Composition of initial melt. There are an unlimited number of scenarios involving subtle changes in the concentrations of the mafic components and the modal mineralogy as calculated from the initial melt composition, and these would lead to slight differences in the temperature and extent of crystallization that are necessary to reach saturation in spessartine-rich garnet. However, the bulk composition and mineral modes used here are typical of holocrystalline S-type granites (e.g., cordierite-biotite granite, Avila batholith, Central Spain: Pereira and Bea 1994; two-mica and biotite granites, Nepal-Tibet: Visonà and Lombardo 2002). Moreover, the modeled change in mineralogy (as a function of F) is similar to reported percentages of different granite facies in natural fractionation sequences. For example, in a study of the Hercynian cordierite-biotite granites of Central Spain, Villaseca et al. (1998) used field relationships and geochemical evidence to show that the most differentiated leucogranites represent, at minimum, the last ~30% of the initial melt.

Solubility data for garnet. The degree of fractional crystallization required to achieve garnet saturation depends on the saturation surface for garnet in granitic melt. However, the solubility of garnet in granitic melt, in terms of MnO content of melt, has not been systematically studied. The solubility data for garnet presented in this study stems from the dissolution of Mn-rich garnet in B-bearing, hydrous granitic melt. We hypothesize

that the concentration of MnO in melt at garnet saturation would be lower in a hydrous but B-free melt of the same composition. Figure 5-4b shows the concentration of MnO at garnet saturation for B-rich melt (this study), F-rich melt (~ 1 wt% F: Icenhower, 1995), and hydrous, but B- and F-free, granitic melt (London et al., 2012). It is clear from the data presented in Figure 5-4b that the solubility of MnO, at garnet saturation, is much lower in B- and F-free granitic melt. In addition, it has been shown that a decrease in the concentration of water in melt results in an increase of the activity of alumina in melt, thereby promoting the crystallization of aluminous phases at lower ASI values of the melt (Acosta-Vigil et al., 2003). We expect that the crystallization of a B-free and less hydrous melt would be to promote garnet crystallization at an F value closer to 1.0 in Figure 5-9.

Table 7: Parameters and results for Rayleigh fractional crystallization model

Partition Coefficients (D)

	FeO	MnO	MgO
T (°C)	Crd/melt	Crd/melt	Crd/melt
800	3.47	1.83	9.82
750	13.89	3.06	38.93
T (°C)	Bt/melt	Bt/melt	Bt/melt
800	22.05	4.61	66.10
750	22.05	4.61	66.10
700	22.05	4.61	66.10
T (°C)	Ms/melt	Ms/melt	Ms/melt
700	5.45	1.17	15.83
650	5.45	1.17	15.83

Bulk partition coefficients (*W*D)

T (°C)	FeO	MnO	MgO
800	0.46	0.16	1.35
750	1.07	0.23	3.04
700	1.39	0.29	4.12
650	1.39	0.29	4.12

Normative Mineralogy

Granite type	Crd, Bt granite	Bt granite	Bt, Ms granite
Qtz	28.27	30.99	31.36
Kfs	28.94	25.47	21.17
Pl	34.56	34.38	35.11
Bt	1.67	5.85	4.79
Crd	6.46	---	---
Ms	---	---	7.57
Als	---	3.31	---

Initial concentrations (C_o)

Granite type	Crd, Bt granite	Bt granite	Bt, Ms granite
FeO	1.72	1.61	1.21
MnO	0.08	0.09	0.20
MgO	0.05	0.03	0.00

Rayleigh parameters (T&F)

Granite type	Crd, Bt granite	Bt granite	Bt, Ms granite
T range (°C)	800 --> 750	750 --> 700	700 --> 650
F (liquid fraction)	1.0 --> 0.8	0.8 --> 0.3	0.3 --> 0.0
% of total crystallization	20	50	30

Final conentrations (C)

Granite type	Crd, Bt granite	Bt granite	Bt, Ms granite
FeO	1.61	1.21	0.03
MnO	0.09	0.20	2.45
MgO	0.03	0.00	0.00